# SURFACE EFFECTS AND GOLD-NANOSTRUCTURE SURFACE COATING OF WHISPERING-GALLERY MICRORESONATORS

By

GANTA DEEPAK

Bachelor of Science

University of Madras

Chennai, India

1999

Master of Science

Oklahoma State University

Stillwater, Oklahoma

2002

Submitted to the Faculty of the
Graduate College of the
Oklahoma State University
in partial fulfillment of
the requirements for
the Degree of
DOCTOR OF PHILOSOPHY
May, 2010

# SURFACE EFFECTS AND GOLD-NANOSTRUCTURE SURFACE COATING OF WHISPERING-GALLERY MICRORESONATORS

Dissertation Approved:

Albert T. Rosenberger

Donna K. Bandy

Weili Zhang

Gil Summy

A. Gordon Emslie

Dean of the Graduate College

# ACKNOWLEDGEMENTS

I would like to thank the people who helped to make this long journey of learning possible. I would like to thank my parents Dr. G. Ramanjaneyulu and Dr. A. Seshukumari for the encouragement, love and support they gave all my life. I would also like to thank B. Vijetha for her support and encouragement.

This dissertation would not be possible without the help from my advisor Dr. A. Rosenberger and I would like to thank him whole heartedly. His patient guidance, encouragement and comments on the drafts improved my presentation and writing skills. I would also like to thank him and Physics department for financial support. I would like to thank my other committee members Dr. W. Zhang, Dr. G. Summy, and Dr. D. Bandy for their guidance and comments throughout the pursuit of this degree.

I would also like to thank my friends at Oklahoma State University. I would like to thank Elijah Dale who has been the best colleague you could wish for, helping and encouraging me in this work. I would also like to thank other colleagues Razvan Stoian, and E. Gonzales. I would also like to thank Warren Grider and Mike Lucas for their help in the machine shop and people from physics department office, especially Susan Cantrell who always enquires of my well being.

# TABLE OF CONTENTS

# LIST OF FIGURES

# LIST OF TABLES

# Chapter I

# INTRODUCTION

High $Q$ (quality factor) optical microcavities are used to confine light, allowing them to be used for storage of optical energy. This ability to confine light in the volume of a fused-silica (for example) microresonator has profound implications in many areas. The light confined in an optical microcavity is in phase with itself after one round trip resulting in resonant modes called "whispering gallery modes". In the 19$^{th}$ century Lord Rayleigh proposed an explanation on the basis of his observations at St. Paul's Cathedral in London, where a whisper against a wall is audible to a listener at any point around the gallery with an ear held to the wall [1-2]. Richtmyer, in 1939, showed that a spherical microparticle could sustain high $Q$ resonant modes [3].

In our lab, whispering gallery modes (WGM) have primarily been observed in spheroidal microresonators. In general, microresonators can be fabricated into various shapes, including microring, cylindrical, micropillar, spheroidal and toroidal chip based [4-8]. They can also be fabricated from many materials such as fused silica, polystyrene, lithium niobate, magnesium fluoride, calcium fluoride and liquid droplets [4-11]. Spheroidal fused-silica microresonators are fabricated in our lab by melting the end of a fused silica fiber, using a hydrogen-oxygen torch as seen in Fig. 1. Microsphere fabrication has also been achieved by using a $CO_2$ laser, placing the fiber in the beam path near a focal point [7]. Surface tension pulls the molten silica into a spheroidal

shape. This high *Q* microresonator, with a long photon storage time on the order of 100's of nanoseconds has an evanescent field extending into the adjacent medium. These microresonators are of interest in various applications like cavity quantum electrodynamics, environmental probes, atom trapping, low threshold lasers, sensing, optical filtering and nonlinear optics [12-18]. The excited optical modes typically lie in the equatorial plane of the microresonator. A tapered fiber is used in our lab to tunnel the evanescent light into the microsphere to excite WGMs of the microresonator. It is tapered or reduced in diameter to 2-3 μm using a flame brush technique with the apparatus seen in Fig. 2.

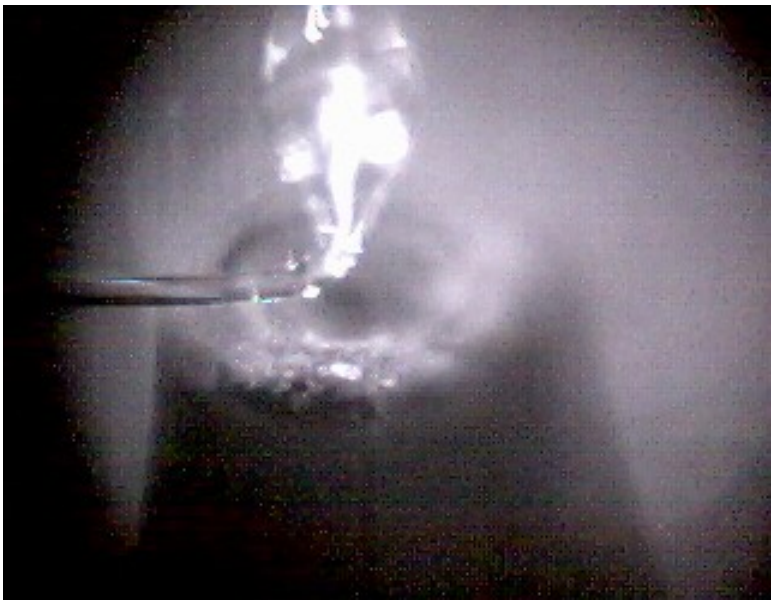

Figure 1. Microsphere being fabricated using hydrogen-oxygen torch.

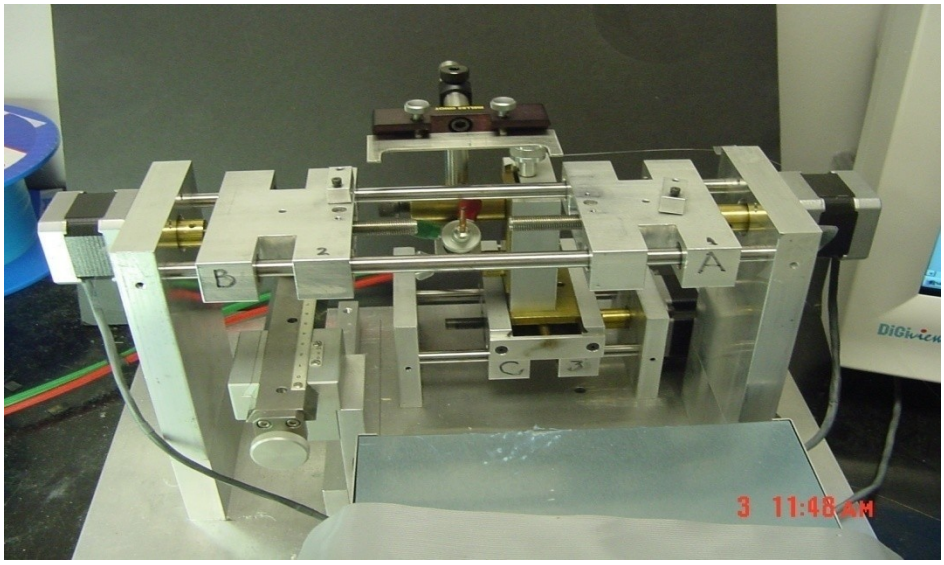


Figure 2. Setup used in our lab for tapering optical fibers.

The tapered region can support multiple modes, in contrast to the untapered region which can support only the fundamental mode of the fiber. The taper becomes effectively a dielectric cylinder in which light is guided by the cladding/air interface rather than by the core/cladding interface. It is known that optimal coupling is obtained by maximizing spatial overlap and minimizing phase mismatch between the fiber mode and the microsphere mode [19, 20]. The $Q$ of the microresonators varies from $10^6$-$10^{11}$, based on the geometry of the resonator [21-24]. The calcium fluoride based microresonators exhibit the highest $Q$, on the order of $10^{11}$ [10, 23]. It has been demonstrated that in a fused-silica microresonator, the ultimate $Q$ factor is limited by water absorption on the surface and internal scattering [22].

There is another method discussed in the literature to couple light into microsphere to excite WGMs, using prism-resonator interface [8, 24]. Alignment issues make it hard to integrate with fiber optic systems.

## I.1 Purpose and Organization of the Thesis

The main purpose of this thesis is to use a tunable diode laser operating around 1570 nm to investigate various effects of the heat transfer from fused-silica microspheres, with and without thin-film coatings, to the surrounding gas in a vacuum chamber. This is an application of microsphere whispering gallery modes to various aspects of surface characterization.

The second major topic discussed in my dissertation is advanced methods for synthesis of gold nanorods and gold nanowires of different sizes, along with characterization methods. Methods of attaching gold nanorods and nanowires to the microresonator using silanes or polymers like PDDA and poly (acrylic acid) will be described, as will better methods to control the concentration and distribution of gold nanorods or gold nanowires on the surface of the microsphere. These coating methods can make the microresonators useful for plasmonic sensing applications and for surface-enhanced Raman scattering (SERS) studies.

In **Chapter II** the general theory behind a novel method for determination of the thermal accommodation coefficient of a gas on a surface is described, followed by experimental results. Results reported here include the thermal accommodation coefficient of air, helium and nitrogen on different surfaces. This accommodation coefficient characterizes the interaction of ambient gas molecules with the surface.

**Chapter III** discusses thermal bistabilty theory and experiment. In an experiment, performed after determining the thermal accommodation coefficient, by observing thermal optical bistability of the WGM resonances, optical absorption coefficients and layer thickness of surface water layers or thin film coatings have been found. The results

are presented. We also discuss methods to find the water layer's rates of desorption and adsorption.

In **Chapter IV** different methods for synthesis of gold nanorods are discussed in detail. The methods used to control the aspect ratio of gold nanorods are discussed in detail. The characterization methods involved are also discussed. Better filtering methods are also discussed for separating gold nanorods from other structures and to improve the yield.

In **Chapter V** the synthesis of gold nanowires using a dielectrophoretic method is discussed in detail. The ability to control the size and shape of gold nanowires is also discussed. Structural characterization methods for gold nanowires are also presented.

In **Chapter VI** the various methods involved in the adhesion of gold nanowires and gold nanorods on modified fused silica microresonator surfaces are discussed, with characterization methods described in detail. The surface charges of various chemicals or polymers are analyzed. The applications of these coated microresonators are discussed briefly. Other materials like carbon nanotubes (CNT) are also coated on the microresonators and the method involved is discussed briefly.

**Chapter VII** summarizes the conclusions and discusses the future direction.

# Chapter II

# THERMAL ACCOMODATION COEFFICIENT

## II.1 Introduction

Whispering-gallery modes (WGMs) of dielectric microresonators can serve as sensitive probes of their environment, through the environment's interaction with the WGMs' evanescent components. For example, high quality factor ($Q$) WGM resonances have been used for microcavity-enhanced laser absorption spectroscopy of molecules in the ambient gas or liquid [13, 22, 25, 26]. Microresonators have also been used as environmental probes making use of the temperature sensitivity of WGM resonance frequencies [27-30].

Heat transfer between solid surfaces and gases continues to be an active area of research at various temperatures and pressures. Thermal accommodation coefficients have been found using various methods involving complex setups for various bulk solid -gas interfaces [31]. In the work reported here, heat transfer between a fused-silica microsphere, which may have a surface coating, and the ambient gas is studied by observing temperature-dependent shifts in WGM frequencies. At wavelengths around 1570 nm, the WGM resonance frequency will shift down by approximately 1.6 GHz for each Kelvin increase in temperature. This shift is primarily due to the temperature-dependent change in refractive index [32], to which is added the effect of thermal

expansion [32]. The expression for temperature -dependent frequency tuning is given by [22]

$$\frac{dv}{dT} = -v\left[\frac{1}{n_s}\frac{dn_s}{dT} + \alpha_{\text{exp}\,ansion}\right], \qquad (1)$$

where $n_s$ is the index of the fused silica and $\alpha_{\text{expansion}} = 5.5 \times 10^{-7}\ \text{K}^{-1}$ is the coefficient of thermal expansion of fused silica. Around 1570 nm, $n_s = 1.45$ approximately and

$\frac{dn_s}{dT} = 11.3 \times 10^{-6}\ \text{K}^{-1}$ [22, 32].

The microsphere is heated by focusing a laser beam onto it; upon turnoff of the heating beam, the microsphere relaxes back to room temperature. From its relaxation rate or thermal decay rate, observed via the WGM frequency shift using a tunable diode laser, we can calculate the thermal conductivity of the surrounding gas. In our work the surrounding gases used are air, helium, and nitrogen. The thermal conductivity of a gas as a function of pressure gives us the thermal accommodation coefficient (roughly the probability that a gas molecule will equilibrate with the surface after one collision) of the gas on fused silica. The surface of bare fused silica is then coated with a layer of polydimethyldiallylammonium chloride (PDDA) or silanized with aminosilane. Silanization is explained in brief in a later section. The temperature relaxation experiments are repeated to find the thermal accommodation coefficients for coated spheres. This is a novel method for finding thermal accommodation coefficients of gases on bare and coated fused silica interfaces, using WGMs at room temperature, unlike other methods, many of which require high temperatures [31].

## II.2 Thermal Accommodation Coefficient Theory

The theory incorporates several simple assumptions. First, the temperature in the microsphere is uniform at all times because of its very fast internal relaxation [33]. Second, as the microsphere cools, heat loss occurs through conduction by the surrounding gas and by radiation. Since the microsphere is so small, convection is negligible [34], and because its mounting stems are so thin, their conduction is negligible. The last assumption is that the microsphere is a perfect sphere with some effective radius, to avoid complications in the theory. Define $T$ to be the deviation of the microsphere's temperature above room temperature $T_R$, and the relaxation equation can be written as follows for $T << T_R$:

$$\frac{dT}{dt} = -\frac{1}{mc}\left(4\pi a k_{gas} + 16\pi a^2 \varepsilon \sigma T_R^3\right)T = -\frac{1}{\tau}T \quad , \tag{2}$$

where the measured value of the thermal conductivity of the ambient gas, $k_{\text{gas}}$, is determined from the measured thermal relaxation time, $\tau$, by

$$k_{gas} = \frac{\rho c a^2}{3\tau} - 4a\varepsilon\sigma(T_R)^3, \tag{3}$$

where $m$ is the microsphere's mass, $\rho$ = 2.20 g·cm$^{-3}$ is the density of fused silica, $c$ = 0.741J·g$^{-1}$·K$^{-1}$ is the specific heat of fused silica, $a$ is the microsphere's radius, $\varepsilon$ = 0.87 is the emissivity of fused silica, and $\sigma$ is the Stefan-Boltzmann constant. If the thermal relaxation time is measured, the thermal conductivity of the gas can be found. To obtain the thermal accommodation coefficient, we must find the thermal conductivity of the ambient gas at various pressures. The measured value of $k_{gas}$ decreases with pressure as

the molecular mean free path becomes comparable to the size of the microsphere. The temperature-jump method (pressure is higher than the free-molecular-flow regime) is used for the pressure dependence of the thermal conductivity of air [35]. If the pressure is low (not extremely low-in the slip flow regime), there will be temperature jumps at the surfaces and that affects the thermal conductivity of the gas, thus making surfaces seem farther apart. The pressure dependence of $k_{gas}$, taking into consideration the temperature jumps, is given in this model by

$$k_{gas}(p) = \frac{k_{atm}}{1 + \left(\frac{2-\alpha}{\alpha}\right)\frac{k_{atm}\sqrt{2\pi R T_R}}{(c_p + c_v)pa}} \quad , \tag{4}$$

where $k_{atm}$ is the thermal conductivity of the gas at atmospheric pressure, $R$ is the gas constant per unit mass of gas, $c_p$ and $c_v$ are the heat capacities of the gas at constant pressure and volume, respectively, $p$ is the gas pressure, and $\alpha$ is the thermal accommodation coefficient for the gas on the surface of interest. The plot of $k_{gas}$ vs. $p$ determines the value of $\alpha$. The thermal accommodation coefficient depends on the specific properties of the material-gas interface. For example, a polished or smooth surface will have a lower thermal accommodation coefficient than an unpolished or rough surface [31]. Table 1 specifies the properties of gases used in this work.

| Gas | $k_{atm}$ (W/ m·K) | $R$ (kJ / kg· K) | $c_p$ (kJ / kg· K) | $c_v$ (kJ / kg· K) |
|---|---|---|---|---|
| Air | 0.025 | 0.287 | 1.01 | 0.718 |
| Helium | 0.142 | 2.080 | 5.19 | 3.12 |
| Nitrogen | 0.025 | 0.297 | 1.04 | 0.743 |

Table 1. Properties of the various ambient gases used in this work.

## II.3 Experiment

The thermal relaxation time $\tau$ is found by measuring the WGM shift as the heated sphere cools back to room temperature, after a focused laser beam which heats the microsphere is turned off. Measurements of WGM frequency versus temperature at wavelengths around 1570 nm yields an average linear shift of -1.60 GHz/K, in agreement with the prediction of Eq. (1) and similar mapping done earlier in [22].

The pressure in the vacuum chamber, which has a transparent top plate and side windows for viewing as shown in Fig. 3, can be reduced from atmospheric pressure (760 Torr) to about 1 mTorr. Light from a cw tunable diode laser (New Focus 6328) is fiber coupled into a lithium niobate Mach-Zehnder amplitude modulator, from which it exits into a single-mode optical fiber that passes through a polarization controller before being fed into the chamber, where its adiabatic bitapered region is brought into contact with the microsphere. As seen in Fig. 4, the microsphere is actually a prolate spheroid, fabricated from optical fiber in such a way as to have very thin stems at both the ends, making it

rigid. The stems are made very thin, of the order of a few μm, to avoid heat loss by conduction through the stems.

.

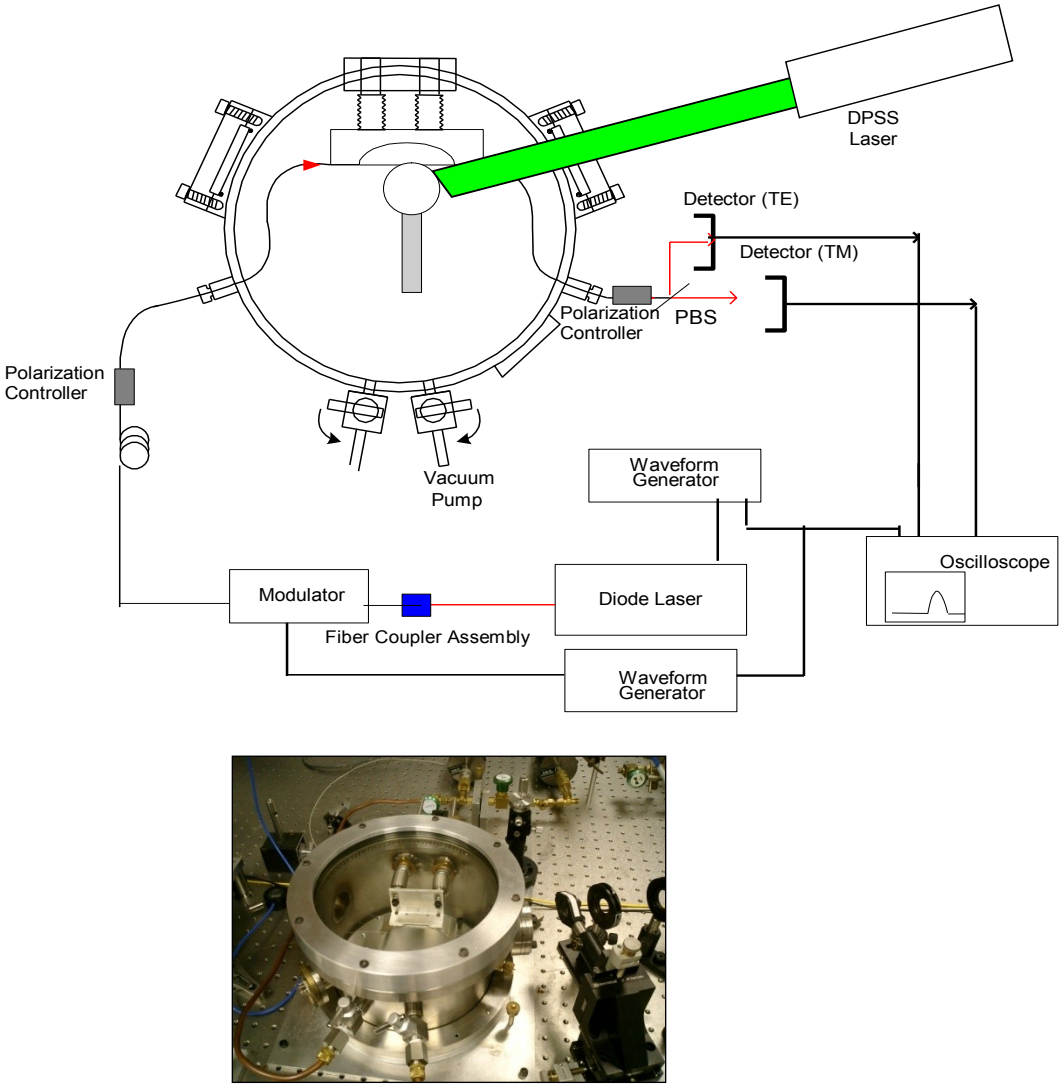


Figure 3. a) Experimental setup. Light from a frequency-scanned cw diode laser is launched into a bi-tapered fiber to excite WGMs of the microresonator. A polarizing beamsplitter (PBS) separates throughput of the two polarizations. A diode-pumped solid state laser (DPSS) can be used as an external heat source for the microsphere, and the vacuum chamber allows control over the ambient pressure. b) The inset shows a photograph of the vacuum chamber used in the experiment.

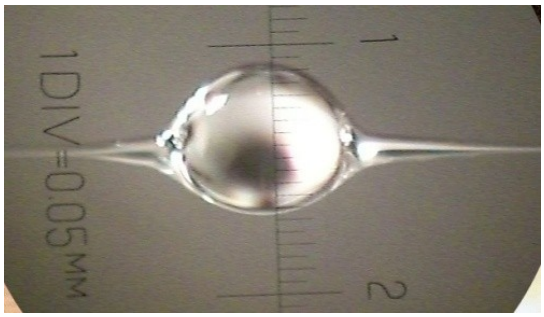


Figure 4. Photograph of a bare fused-silica microsphere with two thin stems. This one has an effective radius, as defined in the text, of 293 μm.

The tapered fiber is used to tunnel the evanescent light into the microsphere to excite WGMs of the microresonator. It is tapered or reduced in diameter to 2-3 μm using the flame brush technique. The tapered fiber is mounted in the vacuum chamber, and its position is controlled by 3D stages located outside the chamber. The tapered fiber and the tapered ends of the microsphere are perpendicular to each other when the microsphere is brought into contact with the tapered fiber.

The polarization controller as seen in Fig. 3 is adjusted to ensure that WGMs of a single polarization (TE or TM) are excited, and after the fiber is fed out of the chamber the two polarizations in the throughput can be detected separately. The modulator is normally off, but can be turned on to provide a square-wave intensity modulation; the throughput response to the square-wave input tells us whether a WGM is undercoupled or overcoupled (intrinsic or coupling loss dominant, respectively) without changing the geometry of the system. The 532-nm heating beam of about 1-2 W comes from a frequency-doubled Nd:$YVO_4$ (DPSS) laser (Spectra-Physics Millennia), and is focused through a side window onto the microsphere as shown in Fig. 3. The diode laser is scanned up and down in frequency by a triangle wave, so that the scan should be linear in

time and have the same rate in both directions. Results from the two scan directions are averaged to reduce error from residual scan nonlinearity due to laser hysteresis (divergence in the scan rate or scan frequency from being linear, caused by the piezo-electric actuator present inside the diode laser). We addressed the hysteresis effect by averaging the $\tau$ values for up and down scans in frequency, that is, the $\tau$ we used for finding thermal conductivity is actually the average for up and down scans. In the thermal accommodation coefficient experiments, the external beam heats the microsphere to a few K above room temperature and is then turned off. The diode laser is operated at low power to prevent bistability effects due to its appreciably heating the microsphere. Displacement of a WGM's throughput dip from one scan trace to the next is analyzed to find the relaxation time constant as the microsphere returns to room temperature. This is done over a wide range of pressures from 760 Torr to 20 mTorr. Fitting the thermal conductivity vs. pressure curve determines the thermal accommodation coefficient as discussed earlier. These experiments, unlike the different methods used to find thermal accommodation coefficients of bulk metals in the past, are performed at room temperature.

## II.4 Results

In this section we first discuss some problems encountered and then present experimental results, for bare and coated fused silica microspheres in three ambient gases. The experiments that were run initially as proof of concept in [22, 36], have a lot of data scatter. This is because the probe power was high enough to cause heating of the sphere; the data scatter is due to changes in the mean temperature of the sphere during the experiments owing to differing heating efficiencies for different resonant WGMs excited during a frequency scan. To avoid this problem, the experiments are run at very low powers (<1 μW), scaled down from 0.2-0.4 mW in [22]. Initially we had trouble in the mode returning to equilibrium temperature after cooling. This was caused by the metal base plate present inside the vacuum chamber, which absorbed heat when the heating beam was focused onto the microsphere and radiated heat when the heat pump was turned off, thus shifting the equilibrium temperature. We addressed this problem by focusing the heating beam from the side glass window instead of through the top glass cover of the vacuum chamber, thus avoiding direct incidence on the base plate.

Because our microresonators are roughly prolate spheroids, and the theoretical model given in Eqs. (2)- (4) assumes spheres, we use an effective radius in the model for data analysis. The effective radius is found by choosing the value of $a$ in Eq. (3) that makes the measured values of the thermal relaxation time $\tau$ give the known value of $k_{gas} = k_{atm}$ at higher pressures (>100 Torr). In the analysis of thermal accommodation data it has been found that the effective radius is near that of the minor radius of a typical highly prolate sphere used in the experiment. The rate of heat transport from the surface is not uniform; it depends on the local radius of curvature. The tapered ends tend to lose heat

faster due to their larger surface to volume ratio. This disagrees with the assumption that effective radius would be approximately the mean radius given that heat transport occurs uniformly over entire area of the sphere, which is not true. So the effective radius is closer to the minor radius.

In this work, the ambient gas will interact with the surface of a fused-silica microsphere that has been prepared in one of several ways. Different surfaces/thin films are obtained by using: bare spheres; spheres coated with a 1-nm-thick film of the polyelectrolyte PDDA, produced by immersion for an hour in a 0.5% solution [37]; and spheres with their surfaces silanized with aminosilane to provide a surface layer of amine groups, limiting the adsorption of water from the ambient gas. After the PDDA coating was applied, the cavity's quality factor was checked against the uncoated quality factor, and no appreciable change was observed at atmospheric pressure. All the PDDA coated samples are rinsed in DI (deionized) water to remove any unbonded PDDA which may outgas at low pressures.

Silanization of the microsphere with aminosilane makes the surface more hydrophobic. Silanization with different silane compounds can be done to provide a surface coating ranging from hydrophobic to polar. The process of silanization is discussed in [38-40]. During the silanization reaction, -Cl, $-OCH_3$ and $-OCH_2CH_3$ groups are converted to –OH groups and these –OH groups react with other –OH groups on the surface of the silica microsphere. These reactive alkoxy groups cross link with the silica surface to different extents.

As in [40], we dipped the bare microsphere in 5% solution of aminosilane in 95% ethanol and 5% water for 30 minutes, then subsequently rinsed with ethanol, and dried in a 120º C oven. The $Q$ of the silanized microresonator is reduced by 1-2 orders of magnitude.

As seen in Figs. 5-7, the measured thermal conductivity of the gas decreases as we decrease the pressure in the vacuum chamber, thus agreeing to the theory discussed in the previous section. Recall that the high-pressure limit of the fit of experimental data to Eq. (4) gives the effective radius $a_{eff}$, leaving the thermal accommodation coefficient $\alpha$ as the only free parameter to be determined by the fit. The results in Fig. 5 give $\alpha$ of air on fused silica to be 0.770 ± 0.027. The $\alpha$ value for air on PDDA was found to be 0.802 ± 0.029 (Fig. 6). For air on silanized fused silica, $\alpha$ was found to be 0.776 ± 0.011 from Fig. 7. The higher $\alpha$ for air on PDDA may reflect the porosity of the coating. These and all other results for accommodation coefficient are summarized in Table 2 at the end of this section.

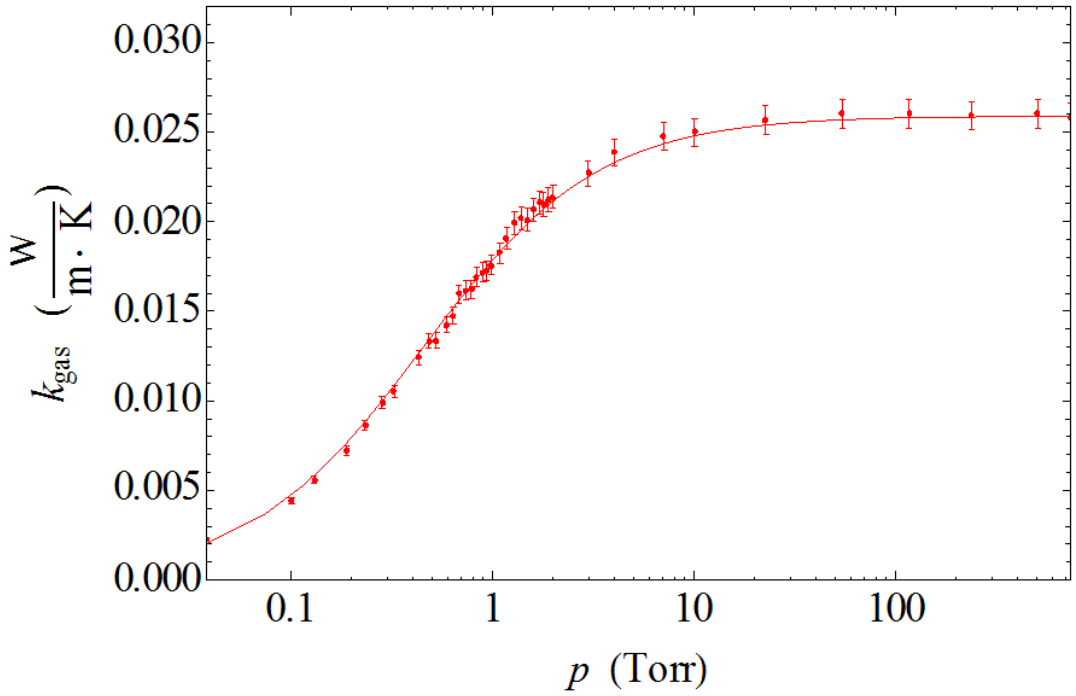


Figure 5. Thermal conductivity of air vs. pressure, measured using a bare microsphere of effective radius 293 μm. The line is a fit to Eq. (4).

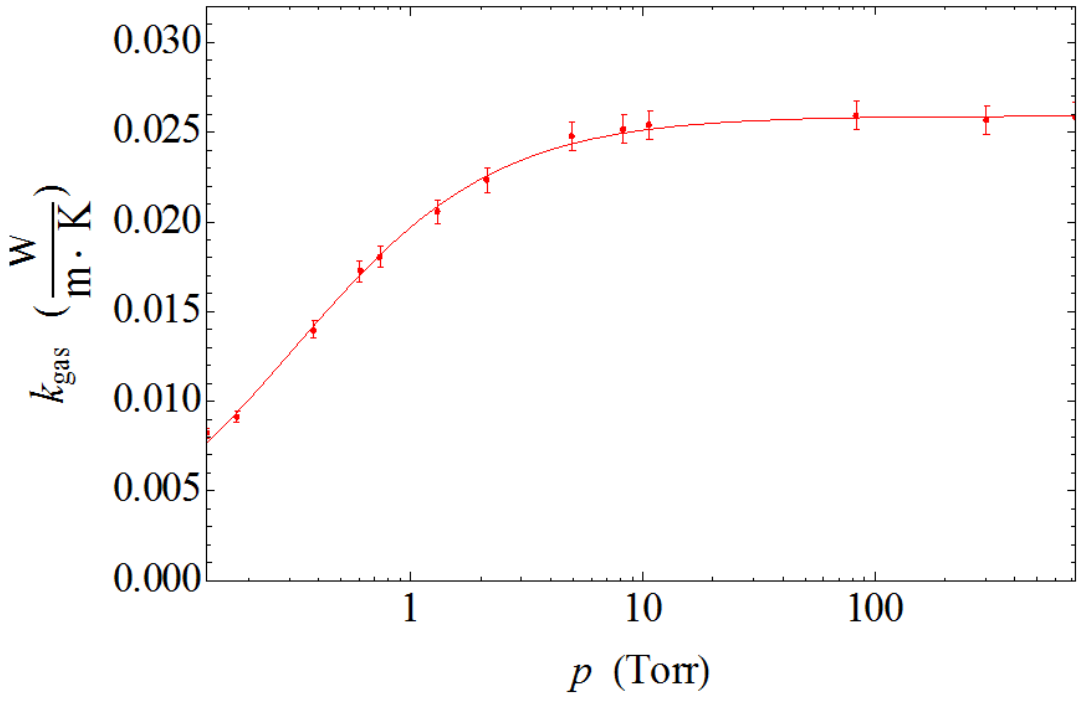


Figure 6. Thermal conductivity of air vs. pressure, measured using a PDDA coated microsphere of effective radius 391 μm. The line is a fit to Eq. (4).

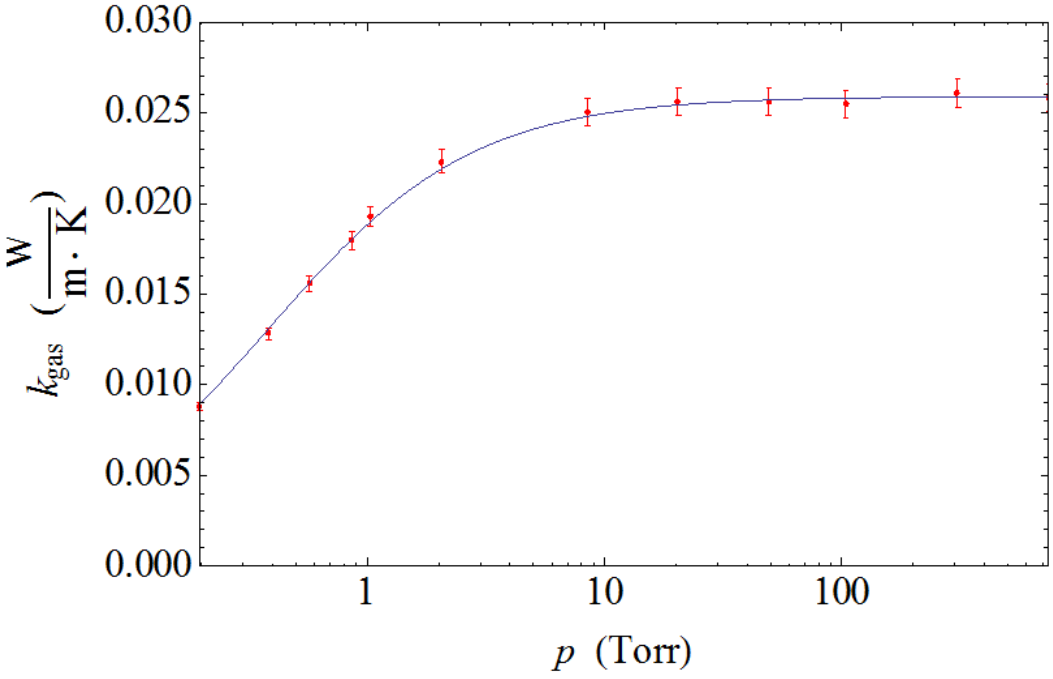


Figure 7. Thermal conductivity of air vs. pressure, measured using a microsphere silanized with aminosilane, of effective radius 345 μm. The line is a fit to Eq. (4).

The $\alpha$ values for helium are found to be 0.388 ± 0.017 on fused silica, 0.352 ± 0.012 on PDDA, and 0.381 ± 0.016 on silanized fused silica from the fits to the data, shown in Figs. 8-10. The thermal accommodation coefficient for helium is significantly lower than for air; this is attributable to the lower atomic mass and momentum which leads to a shorter mean interaction time with the surface. This difference has been observed in the literature for other surfaces [31].

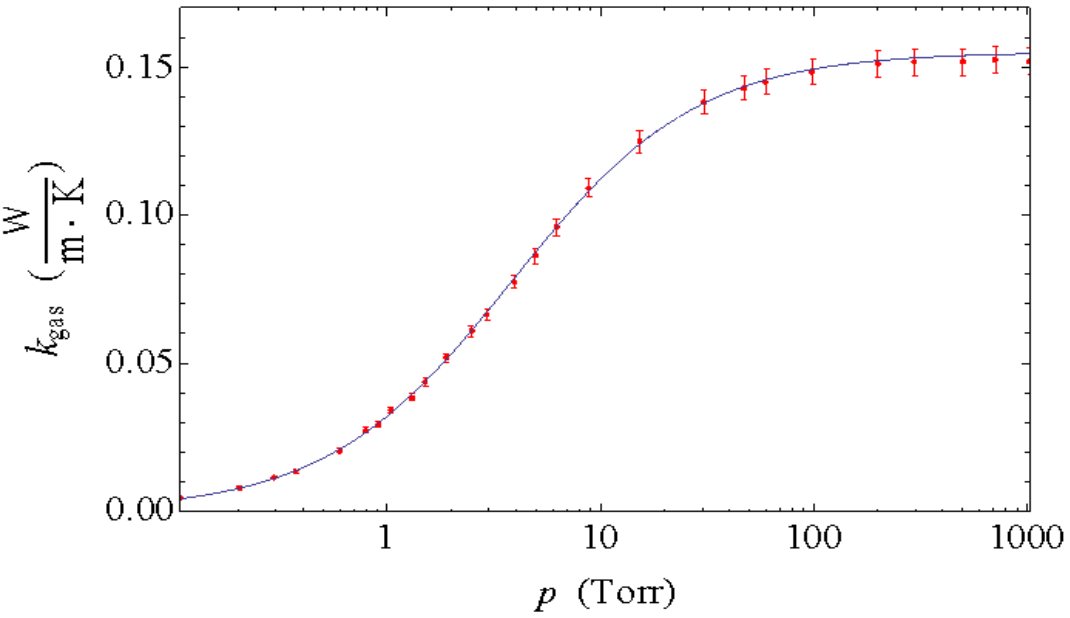


Figure 8. Thermal conductivity of helium vs. pressure, measured using a bare microsphere of effective radius 298 μm. The line is a fit to Eq. (4).

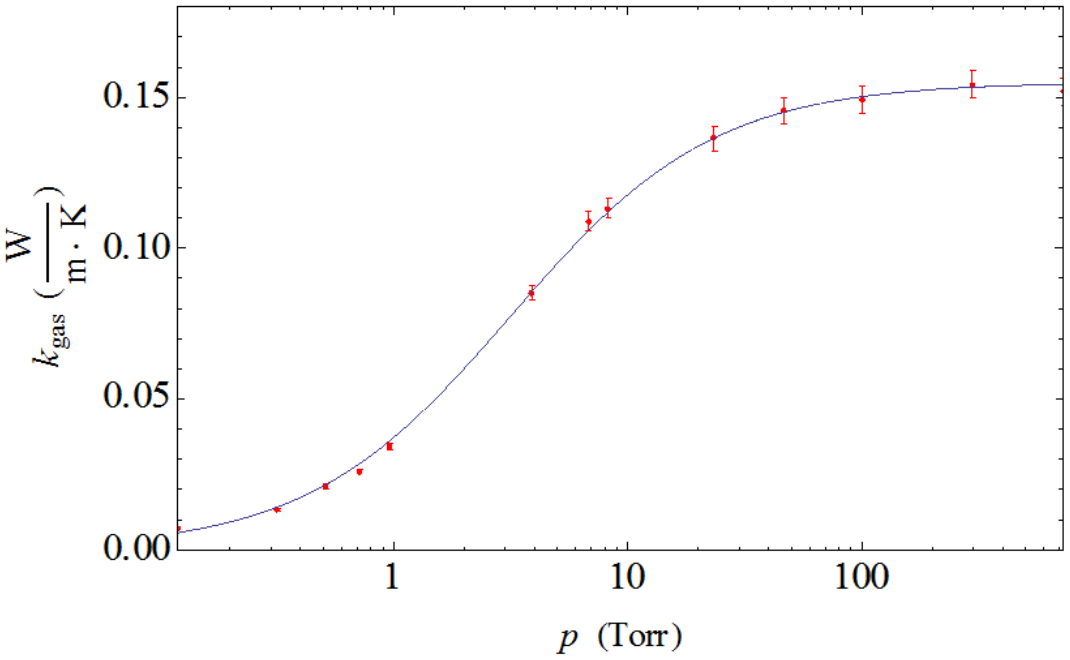


Figure 9. Thermal conductivity of helium vs. pressure, measured using a PDDA coated sphere of effective radius 407 μm. The line is a fit to Eq. (4).

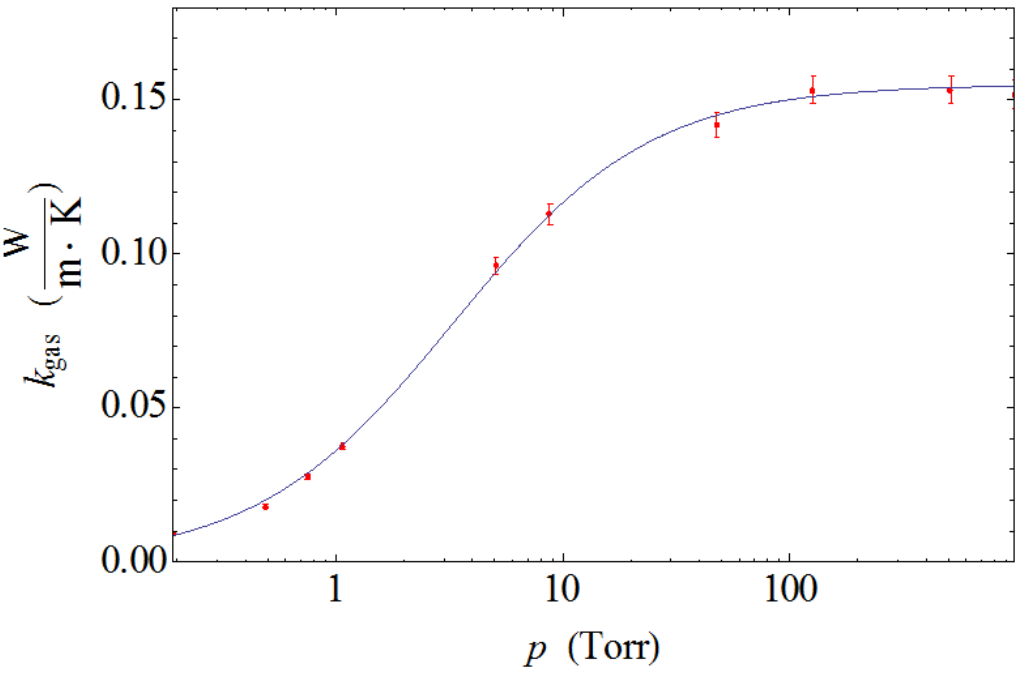


Figure 10. Thermal conductivity of helium vs. pressure, measured using a microsphere silanized with aminosilane, of effective radius 356 μm. The line is a fit to Eq. (4).

Figure 11 gives the thermal accommodation coefficient ($\alpha$) of nitrogen on fused silica to be 0.780 ± 0.027. The value is equal, within the uncertainty, to that obtained for ambient air. Ambient air is a mixture of gases, major components being 78% nitrogen and 21% oxygen. This method verifies the results for air since it is known that $\alpha$ for oxygen has almost exactly the same value as for nitrogen [31]. The experiments are not repeated for coated spheres as we know the values will be close to that of ambient air.

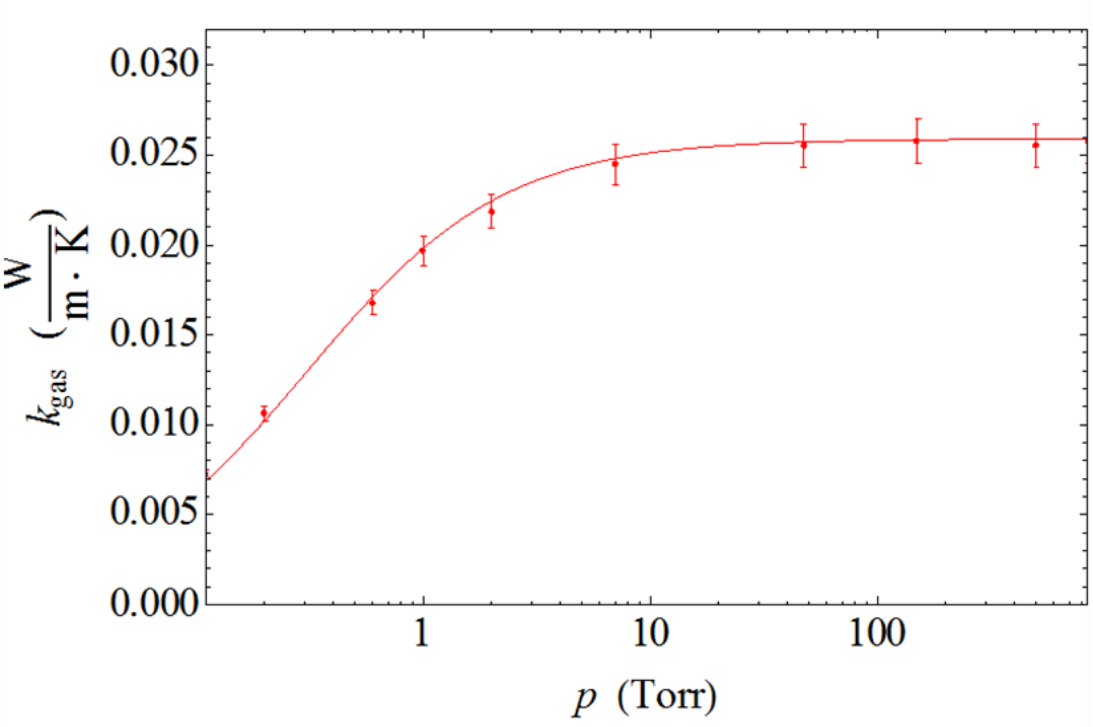


Figure 11. Thermal conductivity of nitrogen vs. pressure, measured using a bare microsphere, of effective radius 426 μm. The line is a fit to Eq. (4).

| Gas | Surface | $a_{eff}$ (μm) | $\alpha$ |
|---|---|---|---|
| Air | Bare | 293 | 0.770 ± 0.027 |
| Air | PDDA | 391 | 0.802 ± 0.029 |
| Air | Silanized | 345 | 0.776 ± 0.011 |
| Helium | Bare | 298 | 0.388 ± 0.017 |
| Helium | PDDA | 407 | 0.352 ± 0.012 |
| Helium | Silanized | 356 | 0.381 ± 0.016 |
| Nitrogen | Bare | 426 | 0.780 ± 0.027 |

Table 2: Summary of results of thermal accommodation coefficient ($\alpha$), of various gases on different surfaces.

## II.5 Effective Radius Calculations

In this section, the idea is to use the measured $a_e$ (minor radius) and $a_p$ (major radius) of the spheroid, and not do a fit to find $a_{eff}$ as in the sphere model; thus the thermal accommodation coefficient becomes the only free parameter. For a prolate spheroid, $a_c$, $a_a$ and $a_v$ are different effective radii found from the measured $a_e$ and $a_p$ [41]; $a_a$ is the area radius that gives the surface area as $4\pi a_a^2$, $a_v$ is the volume radius that gives the volume of the spheroid as (4/3) $\pi$ $a_v^3$, and $a_c$ is the global mean of the local mean radius of curvature. The basic idea is that radiative heat loss depends only on the surface area, but the conductive heat loss is proportional to $a_c$. So the $a$ in the first term of relaxation equation, which defines the rate of heat loss in the microsphere, given by Eq. (2) becomes $a_c$, likewise for $a$ in Eq. (4). Equations (3) and (4) are modified for different effective radii at different points:

$$k_{gas} = \frac{\rho c a_v^3}{3\tau a_c} - \frac{4a_a^2 \varepsilon \sigma (T_{rm})^3}{a_c}, \tag{5}$$

$$k_{gas}(p) = \frac{k_{atm}}{1 + \left(\frac{2-\alpha}{\alpha}\right)\frac{k_{atm}\sqrt{2\pi R T_R}}{(c_p + c_v) p a_c}}, \tag{6}$$

$$e = \sqrt{1 - \left(\frac{a_e}{a_p}\right)^2}, \tag{7}$$

$$a_a = \frac{a_e}{\sqrt{2}}\left[1 + \frac{\sin^{-1} e}{e\sqrt{1-e^2}}\right]^{1/2}, \tag{8}$$

$$a_c = \frac{a_p}{2}\left[1 + \frac{1-e^2}{2e}\ln\left(\frac{1+e}{1-e}\right)\right], \tag{9}$$

$$a_v = [a_e^2 a_p]^{1/3}. \tag{10}$$

Here, $e$ is the eccentricity of the spheroid. The fit to Eq. (6) with $k_{gas}$ given by Eq. (5) is seen in Fig. 12, for helium on a bare microsphere (same data as in Fig. 8, where the simpler model gave. $\alpha = 0.388 \pm 0.017$. The minor and major radii are measured to be 295 ± 2 μm and 365 ± 20 μm respectively. Then $e = 0.617$, $a_a = 317.93$ μm, $a_c = 319.33$ μm, and $a_v = 316.69$ μm.

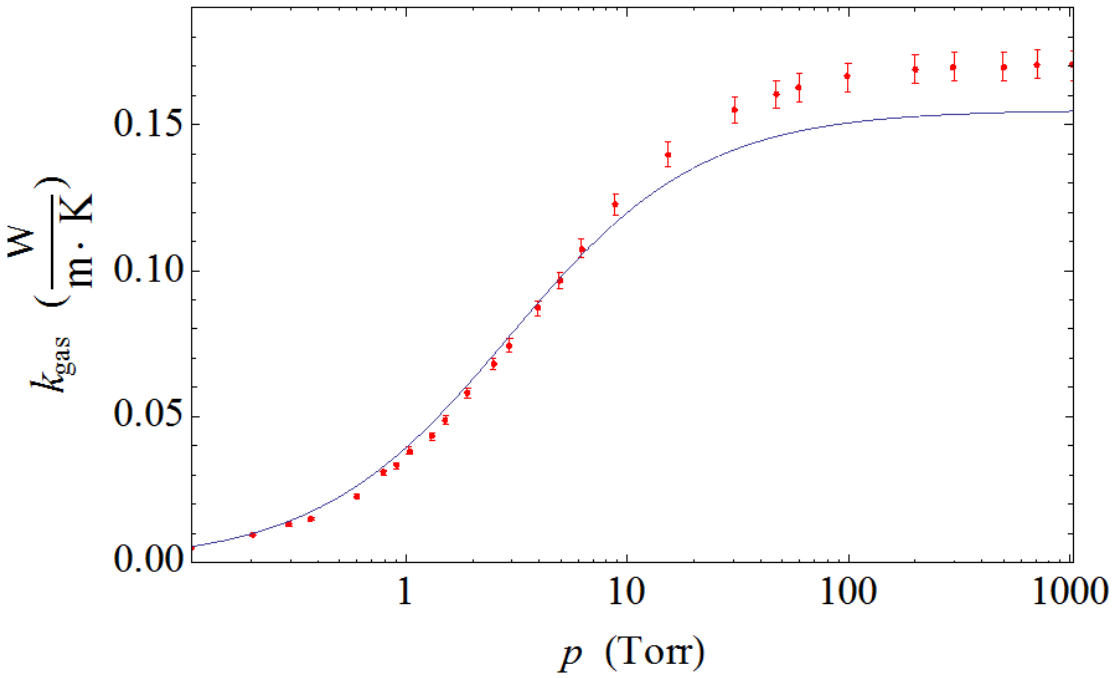


Figure 12. Thermal conductivity of Helium vs. pressure, measured using a bare microsphere, of major radius 365 μm and minor radius 295 μm. The line is a fit to Eq. (4).

Figure 12 gives the $\alpha$ value for helium on fused silica as 0.471 ± 0.017. Next we reduced the value of the major radius by 14 % to (314 μm), assuming there is error beyond the stated uncertainty in measuring it. From the fit in Fig. 13 the $\alpha$ value for helium is found to be 0.403 ± 0.017 on fused silica, in agreement with the result of the simpler model.

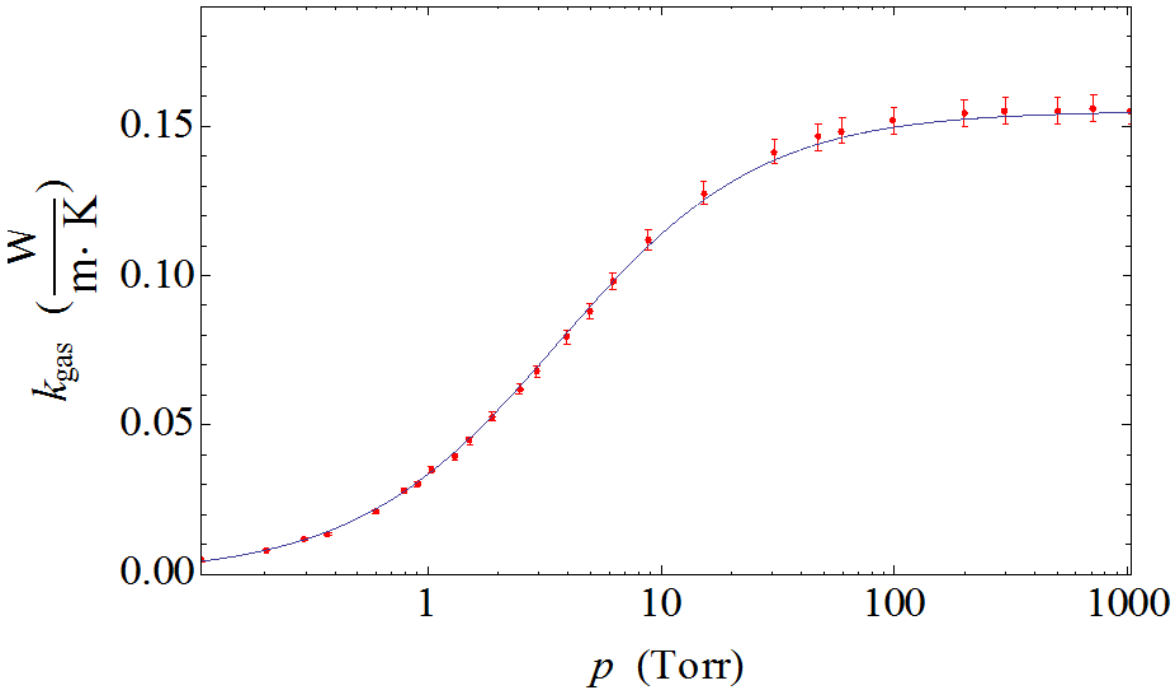


Figure 13. Thermal conductivity of Helium vs. pressure, measured using a bare microsphere, of major radius 318.7 μm and minor radius 295 μm. The line is a fit to Eq. (4).

As the major and minor radii approach closer to each other we get a good fit since the spheroid is becoming a sphere. We attempted the same on bare sphere in air and we could get a reasonable fit when we reduced the major radius by ~18%, giving $\alpha = 0.79 \pm 0.017$. Thus by having to reduce the major radius, we still have two free parameters in the fit, and nothing is gained using this more complicated model.

## II.6 Conclusions

In conclusion, a novel method is presented for measuring thermal accommodation coefficients of various gases on several surfaces at room temperature. The temperature sensitivity of the resonant frequencies of WGMs in a microsphere has been employed to measure the thermal conductivity of the ambient gas as a function of pressure. Measuring the thermal relaxation time to determine $k_{gas}$ vs. $p$, and fitting the results to the temperature-jump model of Eq. (4), determines the value of the thermal accommodation coefficient of the gas on the microsphere surface coated or uncoated. Since these measurements can easily be done with various gases, using different surface coatings (thin compared to the wavelength), a large number of gas-surface interactions can be studied. The precision of these measurements is quite good (< 2%). This optical technique using microresonators is very well suited to making these measurements, and so adds a new method for the study of the interaction of gases with surfaces.

# Chapter III

# THERMAL BISTABILITY

## III.1 Introduction

In this section we discuss the thermal bistability of WGM resonances caused by absorption of the probe laser, which in our case is a tunable diode laser. Intracavity absorption heating and thermal dependence of the refractive index leads to thermal bistability when the resonant frequency shifts either along or opposite the direction of the laser scan. The bistable response gives us the heat supplied by the fraction of total optical power lost due to absorption. The scan rate of the probe laser affects the bistabilty [22, 30]. Bistability can be used to find the contribution of water or film absorption to the total loss on bare and coated spheres, which is a novel method in the case of films. These experiments are done using air, helium, or nitrogen as the ambient gas, on bare, PDDA–coated, and silanized spheres. The thermal decay rate is measured and its experimental value is then used to fit experimental bistability data to a thermal bistability model. The absorption that leads to bistability results from a water layer on the surface of a bare sphere, for a coated sphere it is due to the PDDA layer, and for a silanized sphere it is predominantly due to the coating. This method can be used to find either the absorption coefficient or the thickness of a thin film, provided that one of the two is known. Real time monitoring of thermal properties and quality factor ($Q$) can be

beneficial in studying dynamics of the interaction between a microresonator surface and its environment [30].

## III.2 Thermal Bistability Theory

A wide range of thermally induced behavior such as hysteretic wavelength response and oscillatory instability is observed experimentally for microspheres [29, 30, 42]. Bistability refers to a microsphere's throughput signal depending on the laser frequency scan direction. If the power of the laser which excites the WGMs is high enough, its absorption will heat the microsphere if it is scanned slowly enough across a WGM resonance. When the laser frequency is scanned in the direction of increasing frequency, a fraction of its power is absorbed as it approaches the WGM resonance, thus shifting the WGM frequency downward, opposite the scan direction. This causes the apparent WGM linewidth to be smaller than its actual linewidth. When the laser frequency is scanned in the direction of decreasing frequency, the opposite effect takes place, shifting the resonance frequency in the same direction, causing an apparent linewidth larger than the actual linewidth.

In equilibrium, the power absorbed depends on the detuning from the temperature-dependent resonance, the depth of the resonance dip, and the power incident on the microsphere. Thus a heating term can be added to the right-hand side of Eq. (2) to describe the microsphere's temperature as a function of time and is given by

$$\frac{dT}{dt} = \frac{\beta M_0 P_{inc}}{mc} \frac{\left(\frac{\Delta\nu}{2}\right)^2}{\left(\nu(t) - \nu_0 + bT\right)^2 + \left(\frac{\Delta\nu}{2}\right)^2} - \frac{T}{\tau}, \tag{11}$$

where $m$ is the microsphere mass, $c = 0.741\text{J}\cdot\text{g}^{-1}\cdot\text{K}^{-1}$ is the specific heat of fused silica, $M_0$ is the fractional dip depth, $P_{inc}$ is the power incident on the microsphere (and throughput off resonance), $\Delta\nu$ is the linewidth of the Lorentzian WGM resonance at $\nu_0 - bT$ where $b$ is the 1.6 GHz/K temperature shift, $\nu(t)$ is the scanned laser frequency, and the only free parameter, $\beta$, is the fraction of the total power loss ($M_0 P_{inc}$) that is due to absorption, as opposed to scattering. Fitting the experimental throughput trace to a tuning curve derived from Eq. (11) gives the value of $\beta$. Now from $M_0 = 4x/(1+x)^2$, where the ratio of coupling to intrinsic losses is $x = T_c / 2\pi a\alpha_i$ ($a$ is the microsphere's equatorial radius, approximated here by the $a_{\text{eff}}$ of Section II.4), and the measured quality factor

$$Q = \frac{\nu_0}{\Delta\nu} = \frac{2\pi n}{\lambda(1+x)\alpha_i}, \tag{12}$$

where $n$=1.44 is the index of refraction of fused silica in the range of wavelengths $\lambda$ = 1550 ± 15 nm, the coupling loss $T_c$ and the intrinsic loss coefficient $\alpha_i$ can be found for different coupling regimes [26]. There are two solutions, corresponding to the undercoupled ($x < 1$) and overcoupled ($x > 1$) cases, which is why the lithium niobate modulator as shown in Fig. 3 is needed in the experiment – to determine the coupling regime. Fitting the observed thermal bistability mode profiles to the model allows us to completely specify the system losses, determining how much of the total intrinsic loss is due to absorption [30]. We must make sure we do not see bistability effects when measuring $Q$ or determining the coupling regime, so we use low input power for these measurements. The effective absorption coefficient is

$$\alpha_{abs} = \beta\alpha_i . \tag{13}$$

The effective absorption coefficient is dependent on the $Q$ of the mode and the coupling regime, since we get different solutions for $\alpha_i$ for under- and overcoupling. Knowing the coupling regime we can choose the proper solution, but sometimes both are calculated if the coupling regime is not determined with certainty.

An approximate expression for the relation between the effective absorption coefficient of the water layer (or thin film if it is a coated microsphere), of thickness $\delta$, and its bulk absorption coefficient $\alpha_b$ has been given by [43]

$$\delta \cong \left(\frac{\lambda a}{\pi n^5}\right)^{1/2} \frac{\alpha_{abs}}{4\alpha_b} . \tag{14}$$

From Eq. (14), knowing the thickness of the polymer film or water layer, we can find its bulk absorption coefficient or vice versa.

## III.3 Experimental Setup and Results

In this section we discuss the experimental results for thermal bistability for bare and coated fused silica microspheres. We use the same experimental setup (Fig. 3) used for measuring thermal accommodation coefficient, but without the DPSS laser, as shown in Fig. 14.

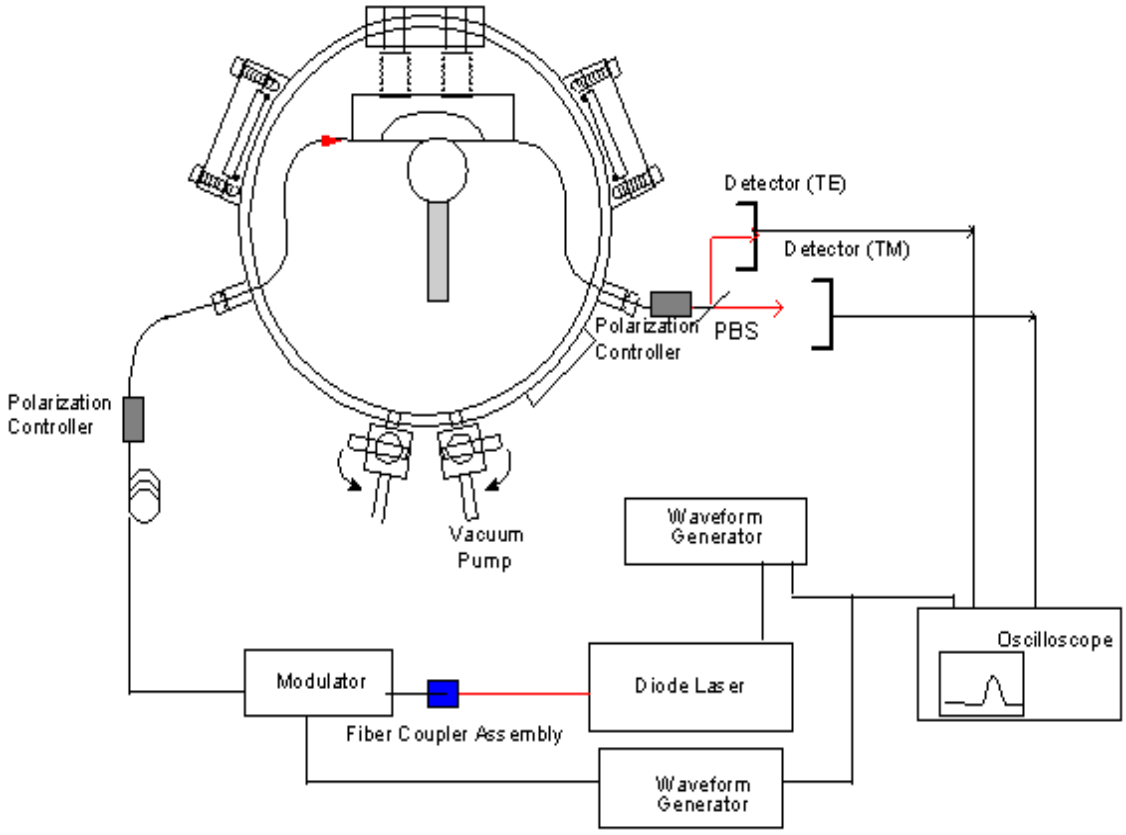


Figure 14. Experimental setup used for performing thermal bistability experiments.

Using slow probe laser scan rates, (<1 MHz/s) and incident power on the order of 150 μW can cause prominent bistability effects to be observed. These experiments are repeated several times with several samples and have good repeatability at several different pressures from 0.022 Torr to 746.4 Torr. Here a few sets of data will be reported for a limited number of pressures, i.e., higher and lower pressures. We assume that for modes of differing radial order, which will have differing evanescent fractions, the effective absorption constants should be very similar because while the evanescent extent is certainly increasing with order the surface water layer or coating is confined to within at most a few nanometers of the surface, which is but a small fraction of the total

evanescent field; so the variation in localized field intensity will be minimal. Therefore, the overall absorption will be very weakly dependent on the evanescent extent. It does depend on the microsphere's radius and the thermal conductivity of the ambient gas as seen from Eqs. (2), (11), and (14). The fitting to the data in Figs. 15-17, which are for a 293 μm bare sphere in air at different pressures at a wavelength of 1560.5 nm, gives the values of $\alpha_{abs}$.

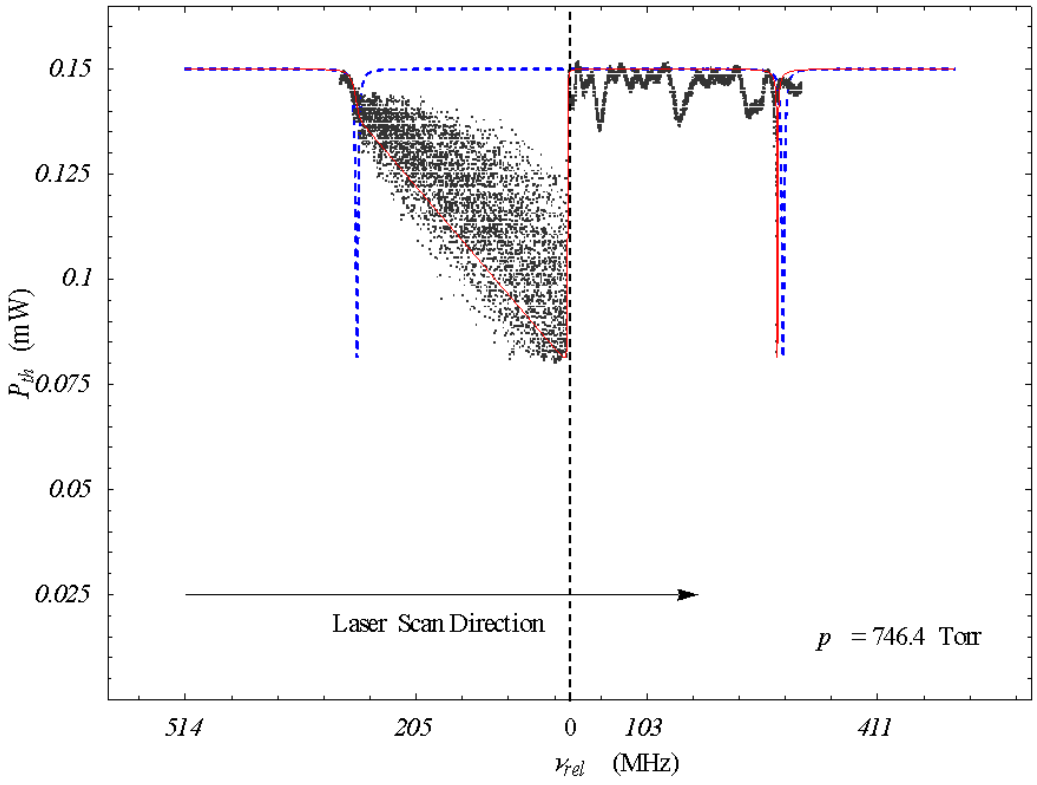


Figure 15. WGM resonance dip showing thermal bistability. The red line is the theoretical fit. The blue dotted line indicates the mode before bistability (at low power). This is an undercoupled mode with $Q = 3.14\times10^7$, as measured at low power and fitting to the model gives $\alpha_{abs} = 0.00440$ m$^{-1}$. On the left side of the figure, the laser is scanning down in frequency through the resonance, and on right the laser scans back up in frequency through the same resonance.

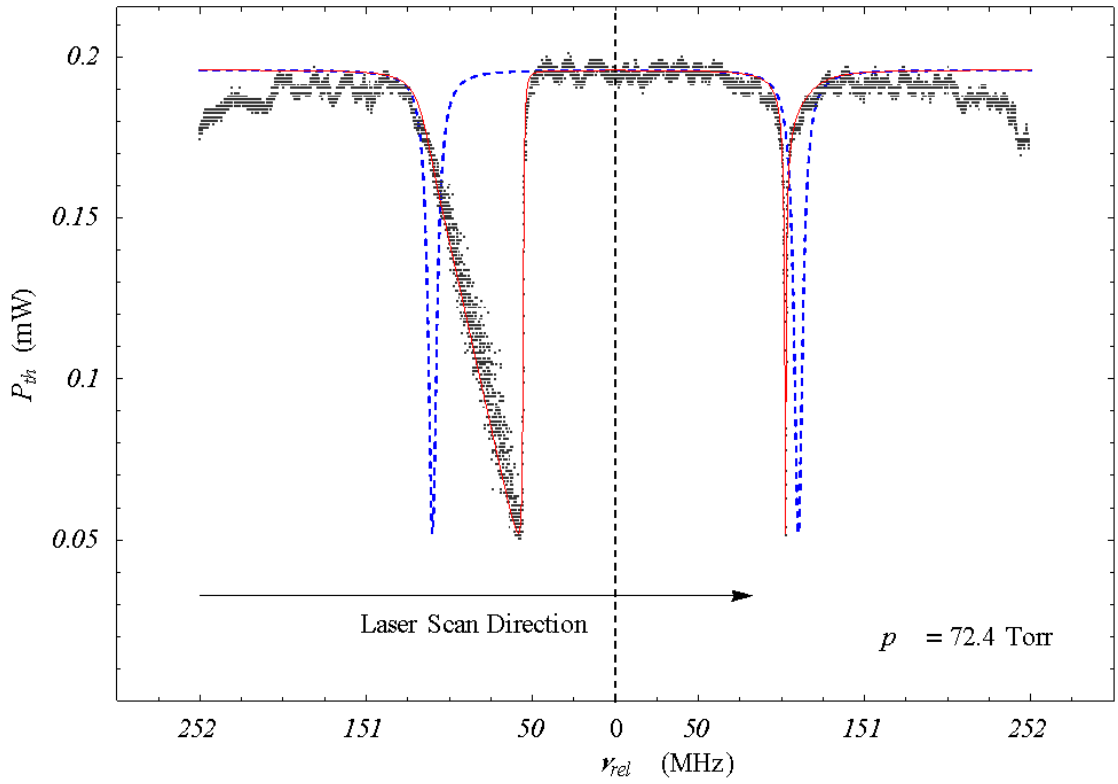


Figure 16. WGM resonance dip showing thermal bistability. The red line is the theoretical fit. The blue dotted line indicates the mode before bistability. This is an undercoupled mode with $Q = 3.14\times10^7$ and $\alpha_{abs} = 0.00357$ m$^{-1}$.

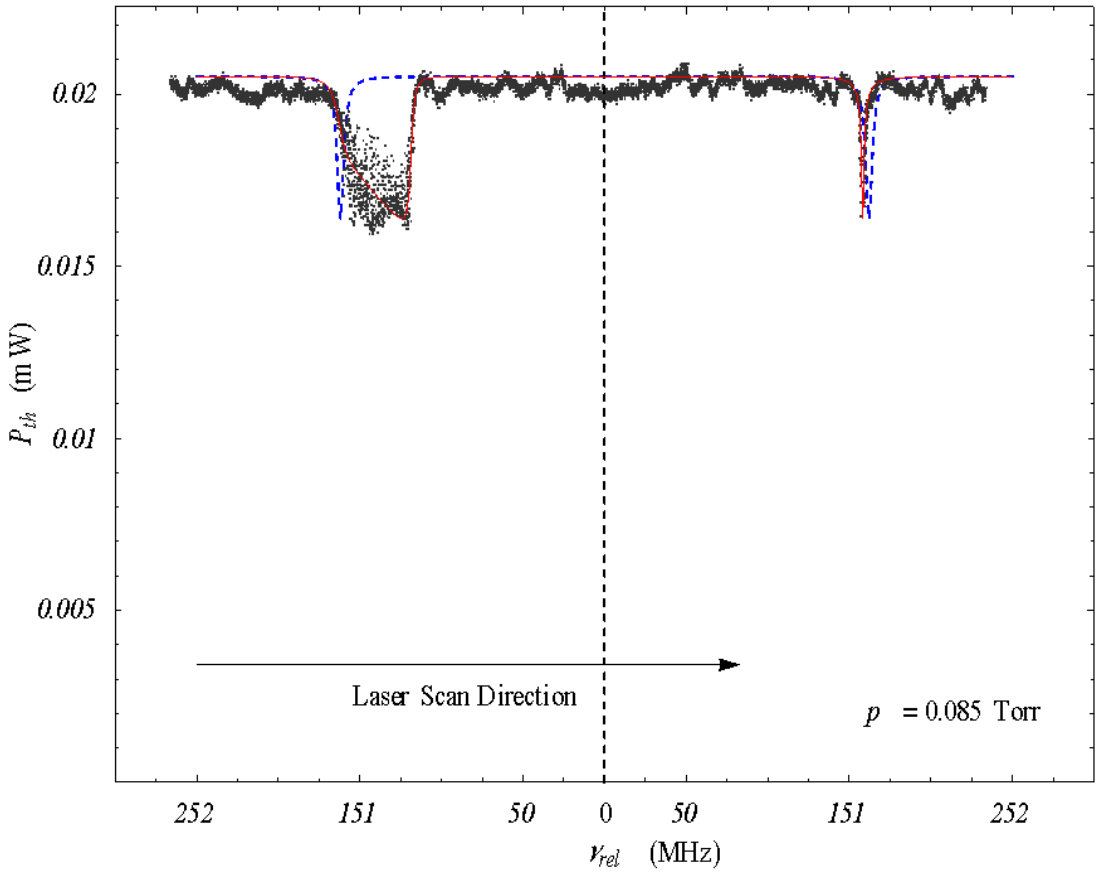


Figure 17. WGM resonance dip showing thermal bistability. The red line is the theoretical fit. The blue dotted line indicates the mode before bistability. This is an overcoupled mode with $Q$ = $3.88 \times 10^7$ and $\alpha_{abs} = 0.00194$ m$^{-1}$.

The pressures at which the experiments are performed are shown in the bistability plots. Knowing the effective absorption coefficient, and that the bulk absorption coefficient ($\alpha_b$) of water at these wavelengths is 800 m$^{-1}$[44], we can find the number of water layers given by Eq. (14). Assuming one monolayer is $1 \times 10^{-10}$ m (it might be as large as twice this value [43, 45]), we can find the water layer thickness $\delta$ in units of monolayers, and that is how it will be presented here. For Fig. 18 $\delta$ is 0.0662, and for Figs. 19 and 20 respectively $\delta$ is 0.0537 and 0.0292. As we vary the pressure from higher to lower the water layer thickness reduces slightly which agrees with our expectations. The oscillation due to thermal nonlinearity as seen in Figs. 15-20 has

previously been observed [29, 42]. They are most likely occurring due to temperature relaxation from the mode volume to the rest of the sphere. We have not modeled the oscillations and fit them to the experimental data as the detailed cause of these oscillations is being further investigated. This effect has been observed to be strongly dependent on the modal quality factor. All bistability experiments were conducted after the sample had been in sustained vacuum for several hours at low pressure, then data were taken as pressure increased. This is why $\delta$ is so low. If a sphere has been at atmospheric pressure for a long time, $\delta$ will be on the order of one monolayer as seen in Fig. 18, where $\delta$ is 1.07. The surface coating close to a monolayer has also been predicted in [45]. The $\alpha_b$ value is strongly dependent on wavelength. For Fig. 18 taking $\alpha_b$ as 880 $m^{-1}$ given in [46], $\delta$ is 0.97 and by taking $\alpha_b$ as 912 $m^{-1}$ as given in [47], $\delta$ is 0.93. That corresponds to slight variation in the prediction of the $\delta$ values by our method.

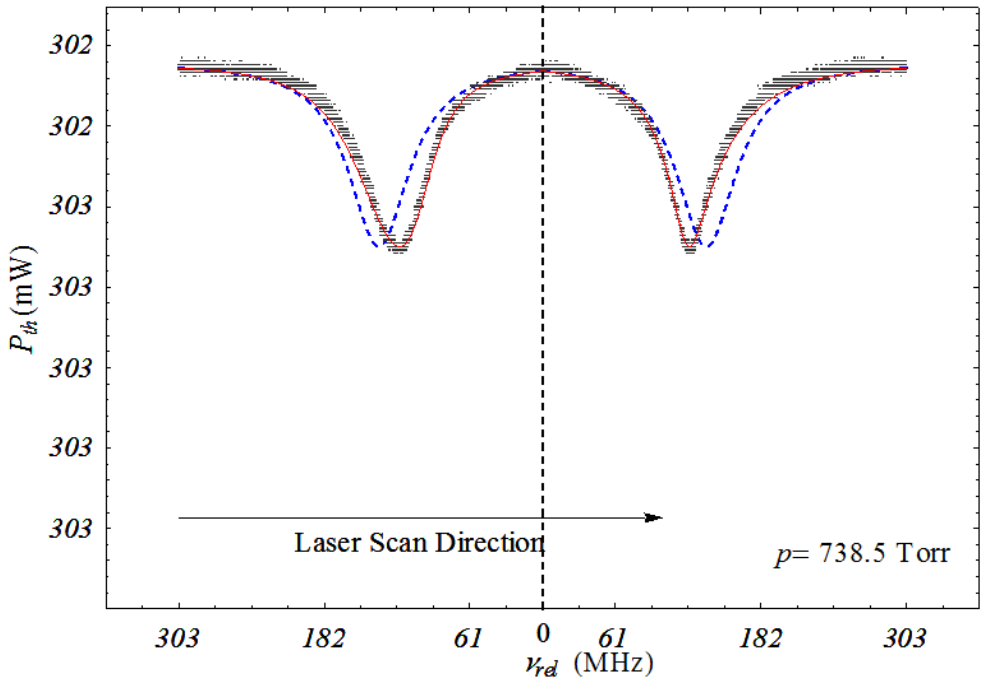


Figure 18. WGM resonance dip showing thermal bistability. For this undercoupled mode at λ = 1542 nm in the bare sphere with $a$ = 426 μm and $Q = 3.16\times10^6$, we find $\alpha_{abs} = 0.0592$ m$^{-1}$.

The spheres are then coated with PDDA and the experiments are repeated for various samples at different pressures. In the first set of experiments we coated the microsphere with PDDA without dipping in DI water to remove the unbonded PDDA and performed the bistability experiments. We observed thicker clusters of PDDA on the surface of microsphere from the SEM images taken on them. For Fig. 19 $\delta$ is 8.08. In this case the change in $\delta$ with pressure is not significant. Absorption is taking place in the PDDA layer, not in a surface water layer, and since the thickness of a PDDA layer is about 1 nm, this result implies that the unrinsed PDDA coating has approximately the same effective $\alpha_b$ as water at this wavelength. A value of $\delta$ = 1 indicates an absorption equivalent to that of one monolayer of water.

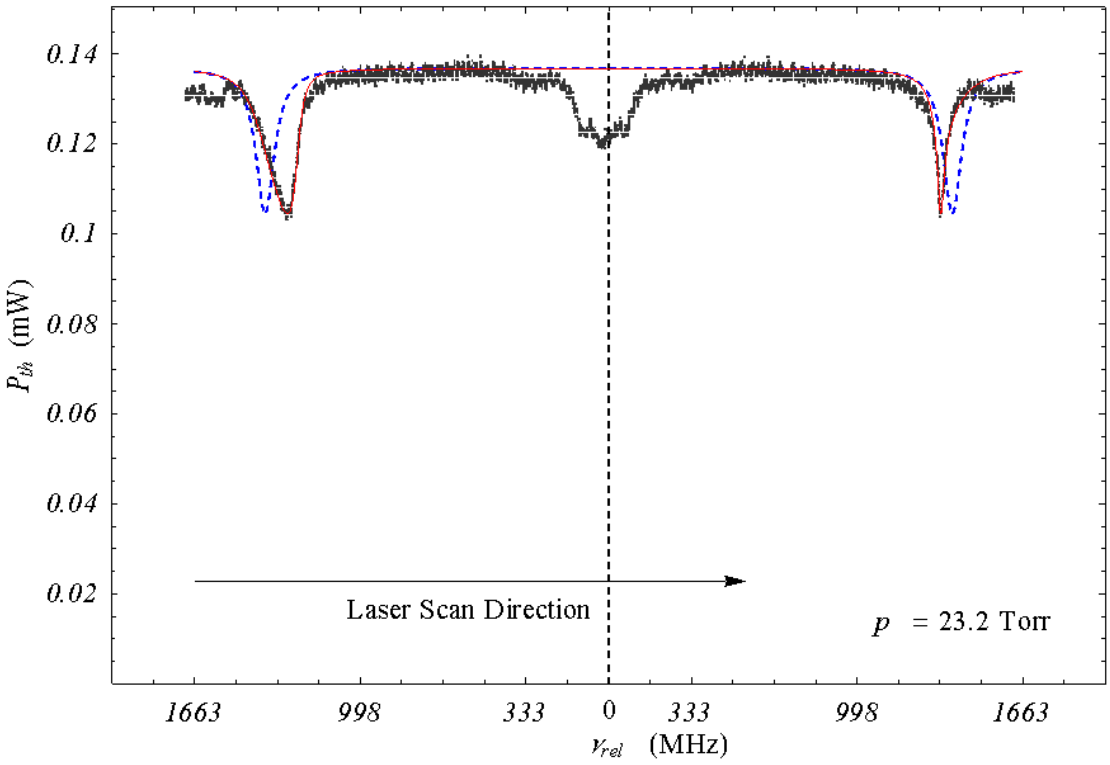


Figure 19. WGM resonance dip showing thermal bistability. For this undercoupled mode at λ = 1563 nm in the PDDA-coated sphere with $a$ = 426 μm and $Q = 2.25\times10^6$, we find $\alpha_{abs} = 0.543$ m$^{-1}$.

Next the same experiment is repeated using a sphere with $\lambda$ = 1559.7 nm and $a$ = 391 μm, but in this case unbonded PDDA is removed by dipping in DI water; $\delta$ in this case was found to be 1.276 at 0.168 Torr and $\alpha_{abs}$= 0.073 $m^{-1}$. This clearly shows that we have removed the unbonded layers and the change in thickness of the PDDA layer is clearly seen from the results of the experiments, by the decrease in $\delta$ values. It might also be that the PDDA clusters that were removed had been binding extra water.

In the next experiment we silanized the microsphere using aminosilane. For Figs. 20 and 21 $\delta$ is 1.01 and 0.921 respectively. We observed this small drop in $\delta$ immediately upon going below vapor pressure of water, indicating reduced bond strength because the surface is hydrophobic after silanization. The pressure change does not seem to have a significant effect on the overall $\delta$, which is large compared to the $\delta$ value on the bare sphere. Thus we conclude that nearly all of the absorption is taking place in the silanized layer, not in a surface water layer.

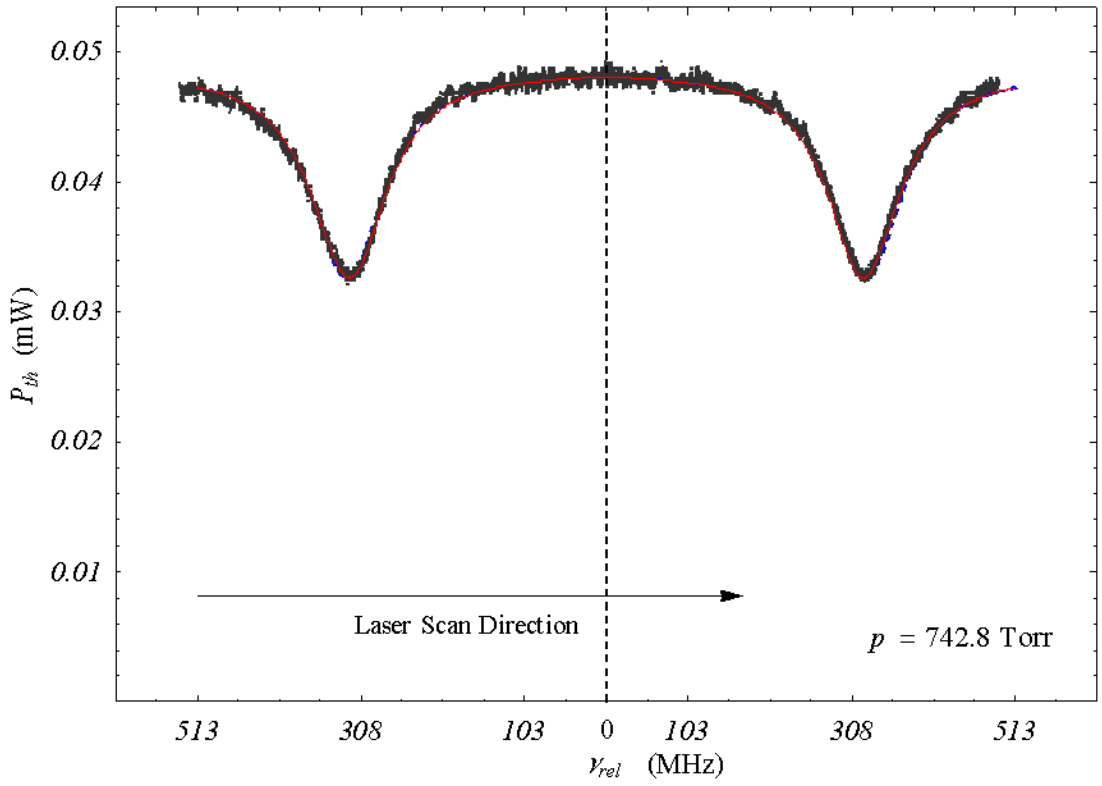


Figure 20. WGM resonance dip showing thermal bistability. For this undercoupled mode at λ = 1560 nm in the silanized sphere with $a$ = 345 μm and $Q = 1.35\times10^6$, we find $\alpha_{abs} = 0.0619$ m$^{-1}$.

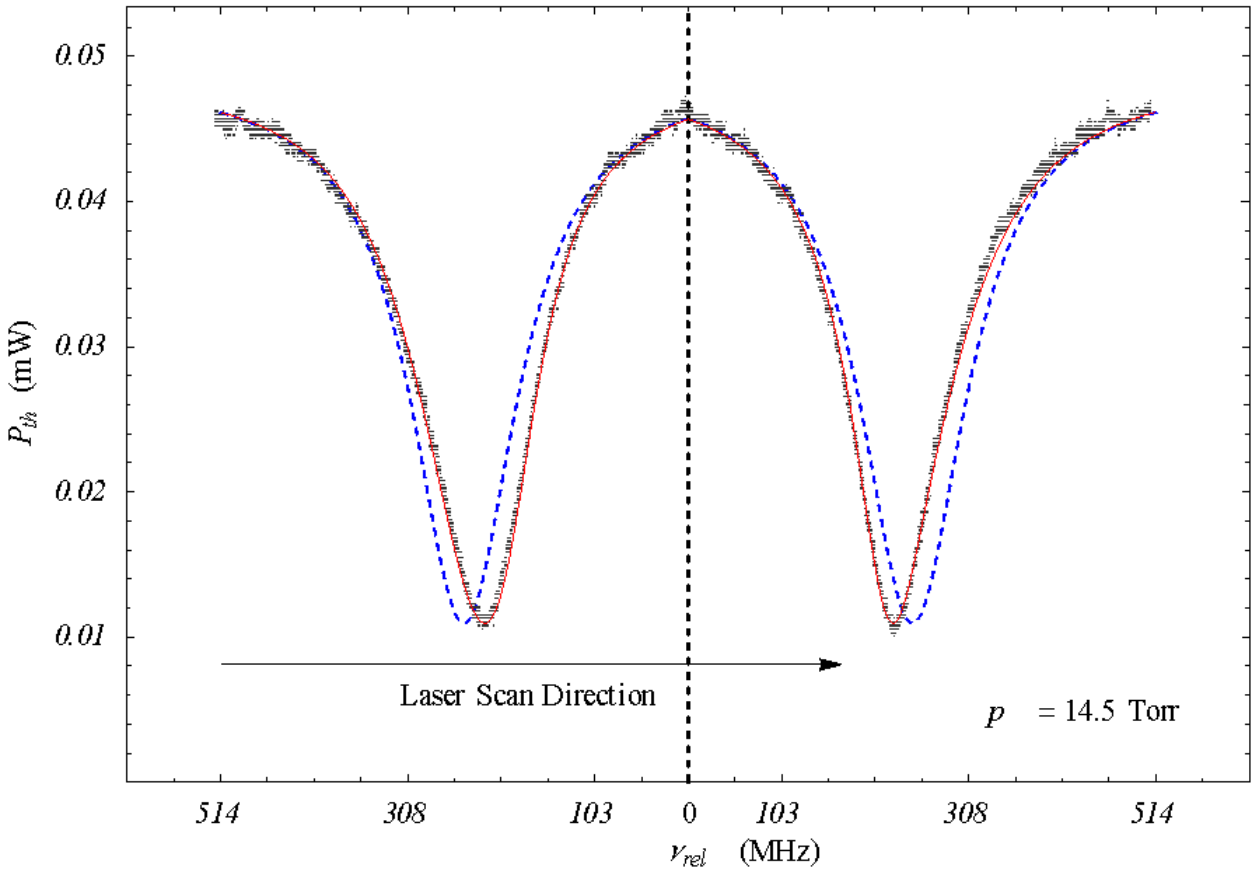


Figure 21. WGM resonance dip showing thermal bistability. For this undercoupled mode at λ = 1560 nm in the silanized sphere with $a$ = 345 μm and $Q = 1.35\times10^6$, we find $\alpha_{abs} = 0.0563$ m$^{-1}$.

Next the thermal bistability experiments are repeated for bare microsphere-helium interfaces and coated microsphere-helium interfaces. For the bare sphere of Fig. 22, $\delta$ is 1.06.

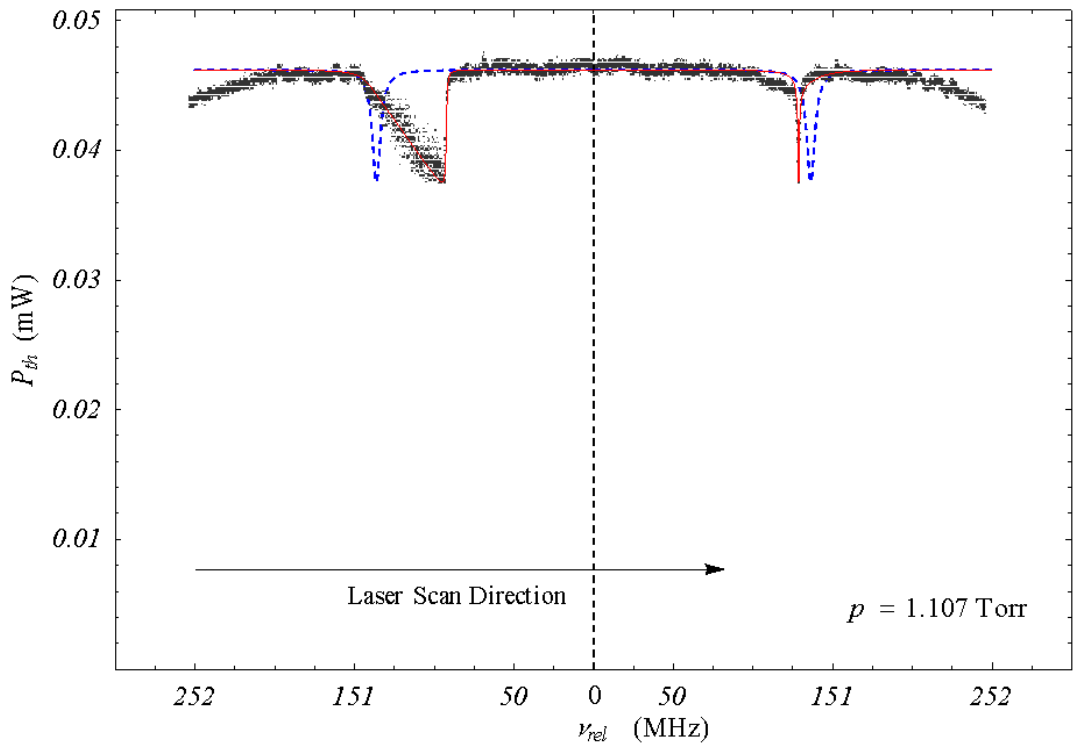


Figure 22. WGM resonance dip showing thermal bistability for this undercoupled mode at λ = 1560 nm, of a bare sphere in helium with $a$ = 285 μm, we find $\alpha_{abs}$ = 0.0716 m$^{-1}$.

There is no change in the number of water layers with change in pressure, probably because the microsphere was not held at low pressure for a long amount of time, as we changed the pressure. Initially the vacuum chamber was flushed and filled 2-3 times with helium to avoid air being present. Thermal bistability experiments are repeated for silanized microsphere and PDDA coated sphere in helium. One set of data for each sample at a given pressure is reported here.

For Figs. 23 and 24, $\delta$ is 1.01 and 1.87 respectively, about same as observed in air. As expected, changes in the ambient helium pressure do not seem to have any effect on the absorption in either coating. Table 3 summarizes the results discussed in this section.

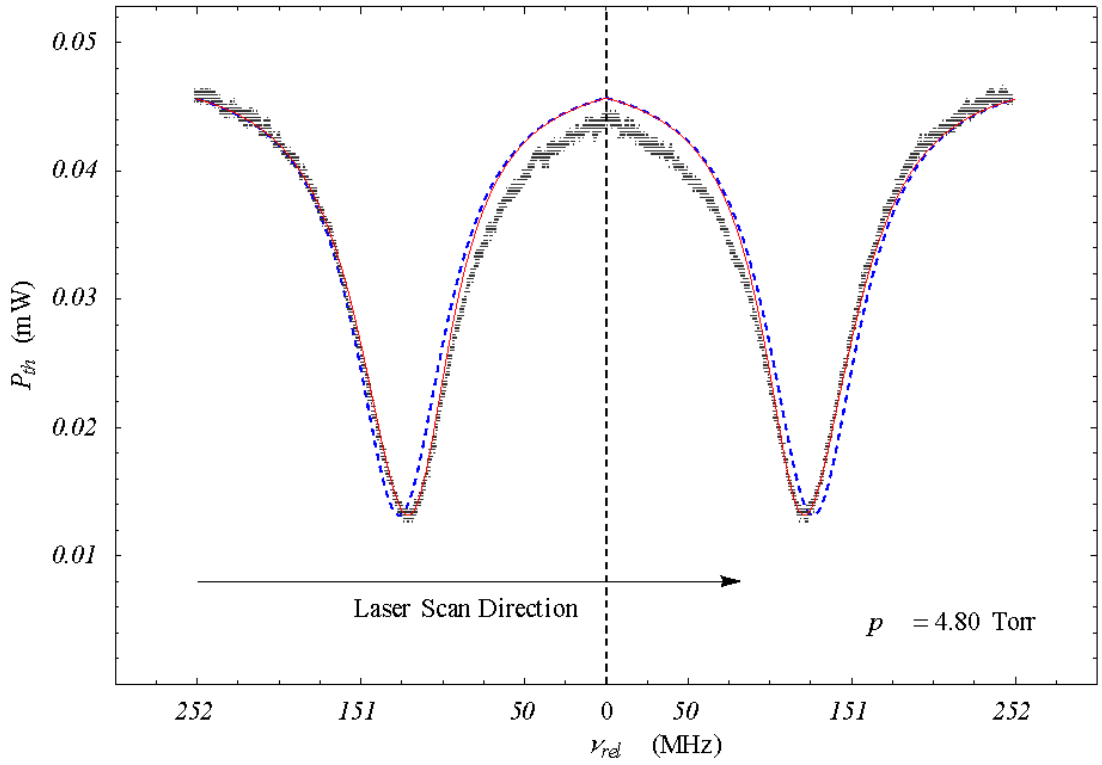


Figure 23. WGM resonance dip showing thermal bistability. For this undercoupled mode at λ = 1560 nm, of a silanized sphere in helium with $a$ = 340 μm,we find $Q$ = $2.82\times10^6$, $\alpha_{abs} = 0.063$ m$^{-1}$.

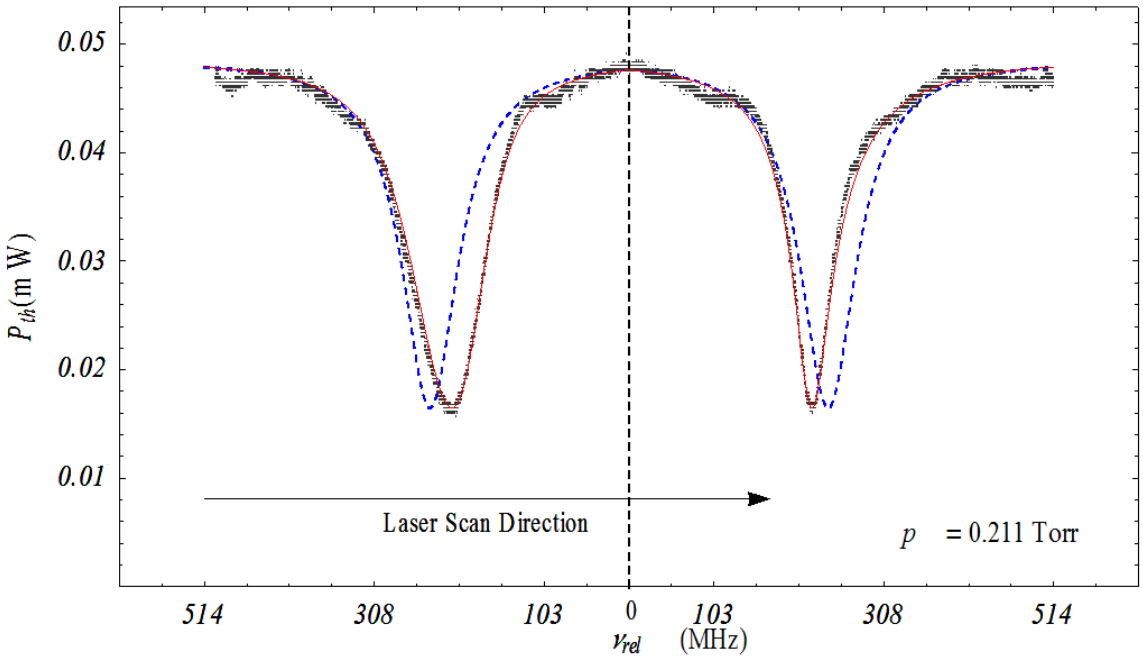


Figure 24. WGM resonance dip showing thermal bistability. For this undercoupled mode at $\lambda$ = 1560 nm, of a PDDA coated sphere in helium with $a$ = 391 μm $Q = 2.33\times10^6$, we find $\alpha_{abs}$ = 0.108 $m^{-1}$.

| Surface | Gas | λ (nm) | $a$ (μm) | Pressure (Torr) | $\alpha_{abs}$ ($m^{-1}$) | $\delta$ (monolayer) |
|---|---|---|---|---|---|---|
| Bare* | Air | 1560 | 293 | 746.4 | 0.004 | 0.06 |
| Bare* | Air | 1560 | 293 | 72.40 | 0.003 | 0.05 |
| Bare* | Air | 1560 | 293 | 0.085 | 0.001 | 0.02 |
| Bare | Air | 1542 | 426 | 738.5 | 0.059 | 1.07 |
| PDDA | Air | 1560 | 391 | 0.618 | 0.073 | 1.27 |
| PDDA (Unrinsed) | Air | 1563 | 426 | 724.2 | 0.529 | 7.88 |
| PDDA (Unrinsed) | Air | 1563 | 426 | 23.20 | 0.543 | 8.08 |
| Silanized | Air | 1560 | 345 | 742.8 | 0.062 | 1.01 |
| Silanized | Air | 1560 | 345 | 14.50 | 0.056 | 0.92 |
| Bare | Helium | 1560 | 285 | 1.107 | 0.071 | 1.06 |
| PDDA | Helium | 1560 | 391 | 0.211 | 0.108 | 1.87 |
| Silanized | Helium | 1560 | 391 | 4.80 | 0.063 | 1.01 |

Table 3. Comparison of absorption coefficients at various pressures for different surfaces in different gases. *The samples were not held at atmospheric pressure for a long amount of time.

## III.4 Water Layer Desorption Rate

An experiment was performed to find the water desorption rate from the surface of a bare silica microsphere in air. Performing thermal bistability experiments is a novel method to find the desorption and adsorption rates for a water layer thickness of the order of a monolayer, at room temperature.

Initially an experiment was performed to find the water desorption rate from the surface of a bare silica microsphere in air as proof of concept. As seen in Fig. 25, when a bare microsphere is kept in the vacuum chamber at constant pressure of 0.024 Torr, $\delta$ will decrease. We typically kept it for 120 hrs in this case before performing bistability experiments. A similar experiment was performed to find the water layer desorption rate

from the surface of a bare silica microsphere in nitrogen with more precision and more data points as shown in Fig. 26.

Within the respective uncertainties the values of the water desorption rates appear to be approximately equal for nitrogen and air. The desorption is roughly exponential, with a decay time of ~40 hrs, as found from the fit (line) in Fig. 26.

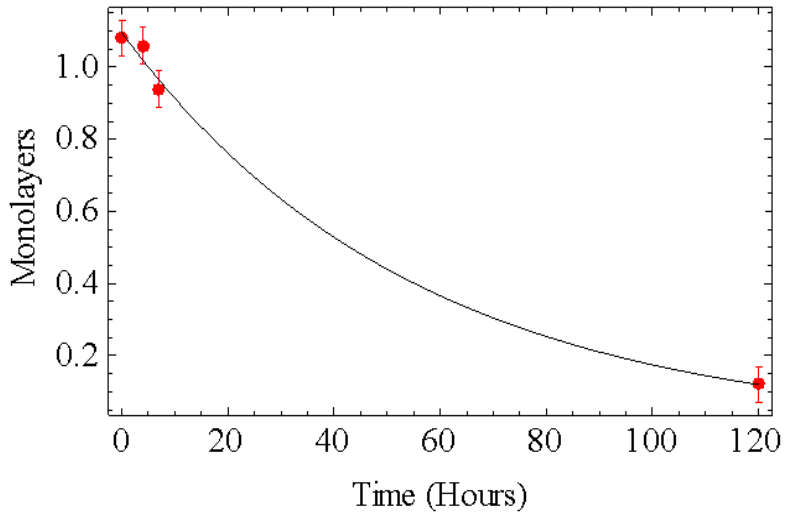


Figure 25. Surface water layers vs. time, measured using a bare microsphere of effective radius 293 μm in ambient air.

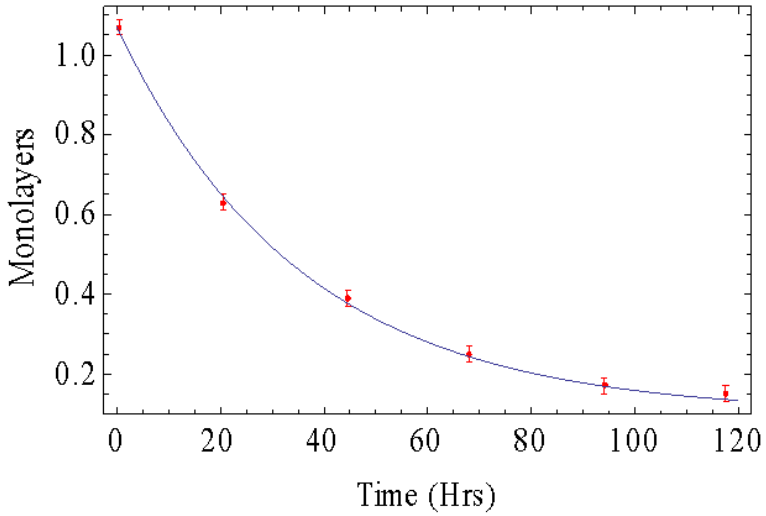


Figure 26. Surface water layers vs. time, measured using a bare microsphere of effective radius 426 μm in nitrogen.

After 120 hrs when $\delta$ is 0.150, for bare sphere in air to find the water layer adsorption time, the vacuum chamber is brought back to atmospheric pressure and the value of $\delta$ reaches 1.007 after 15-20 minutes. Figure 27 shows water layer desorption of a bare sphere in nitrogen and, after 120 hours when returned to atmospheric pressure, water layer adsorption.

Therefore bare sphere in air takes less time for water adsorption, compared with nitrogen, which is drier and takes around 24 hours for water adsorption as seen from Fig. 27.

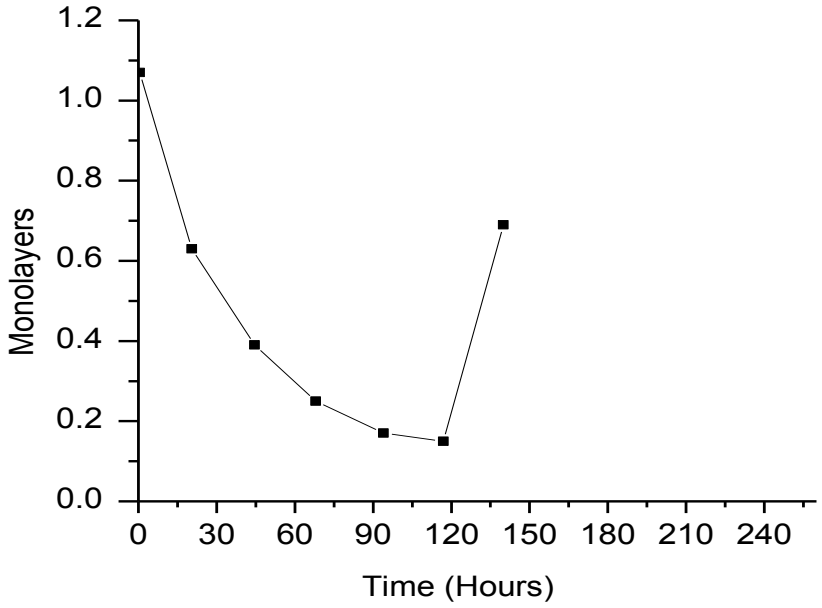


Figure 27. Surface water layers vs. time, measured using a bare microsphere of effective radius 426 μm in nitrogen. The pressure is returned to atmospheric at 120 hours.

Similarly the experiments are repeated for a silanized sphere to find the water layer desorption rate; in 10 minutes $\delta$ is 1.007 and we observed no change after 24 hrs. That implies water layer is weakly bonded onto the surface of the silanized sphere. Next the above experiments are repeated for PDDA coated sphere and there is only a small change in $\delta$ from 1.85 to 1.77 in 16 hrs, suggesting that the PDDA layer binds some water.

## III.5 Surface Layer Mode Fraction Estimation

The field from a whispering gallery mode extends outside the geometrical boundary of the microresonator. The mode volume fraction of the evanescent wave extending outside depends on the size of the microresonator and the refractive index contrast between the microsphere and the surrounding medium. With small index contrast, for example immersion of the microsphere in water, the evanescent fraction is

larger than for the same microsphere in air where the index contrast is high. The refractive index of air is 1.00 compared to refractive index of water 1.33, while the index of refraction for a fused-silica microsphere is 1.45 at 1550 nm wavelength.

There are two kinds of microsphere modes, TE (transverse electric) and TM (transverse magnetic) modes, based on how the magnetic and electric fields orient themselves with respect to the surface of the sphere and direction of propagation. From the solution of Maxwell's equations in three dimensions we can get the expression for the field and it is given, as in [20], by

$$\Psi_{qlm}(r,\theta,\phi) = N_s \Psi_r(r)\Psi_\theta(\theta)\Psi_\phi(\phi), \tag{15}$$

where $\Psi$ is the electric field in the case of TE modes and is the magnetic field in the case of TM modes, $N_s$ is a normalization constant and the order of the mode is given by $q$ (radial mode order) and $l$ - $|m|$ is the polar mode order. Forms of the fields from [20] used in the calculations are solved using a Mathematica routine:

$$\Psi_r(r) = j_l(kn_s r), r \le a, \tag{16}$$

$$\Psi_r(r) = h_l(kn_o r), r > a, \tag{17}$$

$$\Psi_\theta(\theta) = P_l^m(\sin\theta), \tag{18}$$

$$\Psi_\phi(\phi) = e^{\pm im\phi}, \tag{19}$$

where $n_s$ is the refractive index of the sphere, $n_o$ is the refractive index of the ambient, $j_l$ and $h_l$ are the spherical Bessel functions of first kind and spherical Hankel functions, $P_l^m$ are the associated Legendre polynomials, and $a$ is the radius of the microsphere. No accurate experimental method to determine the evanescent fraction that will work with all

cases has yet to be devised. The evanescent field is well approximated by an exponentially decaying radial function, with decay length $\frac{\lambda}{2\pi\sqrt{n_s^2 - n_o^2}}$.

From the field we can calculate the intensity of the mode and by integrating it over the radial coordinate, the evanescent fraction ($f$) can be calculated:

$$f = \frac{\int_a^\infty I(r) r^2 dr}{\int_0^\infty I(r) r^2 dr} \tag{20}$$

where $I(r)$ is the intensity of the mode. If we have a surface layer present (water or applied coating), the fraction of the mode contained within it can be calculated from the following expression:

$$f_l = \frac{\int_a^{a+\delta} I(r) r^2 dr}{\int_0^\infty I(r) r^2 dr} \tag{21}$$

Where $\delta$ is the thickness of the layer and $f_l$ is its mode fraction. In the following calculations, we will take $\delta$ = 0.1 nm, corresponding to one monolayer of water.

From Fig. 28 for a microsphere of radius 300 μm at $\lambda$ = 1550 nm, $f$ = 0.00155 and $f_l = 1.91 \times 10^{-6}$.

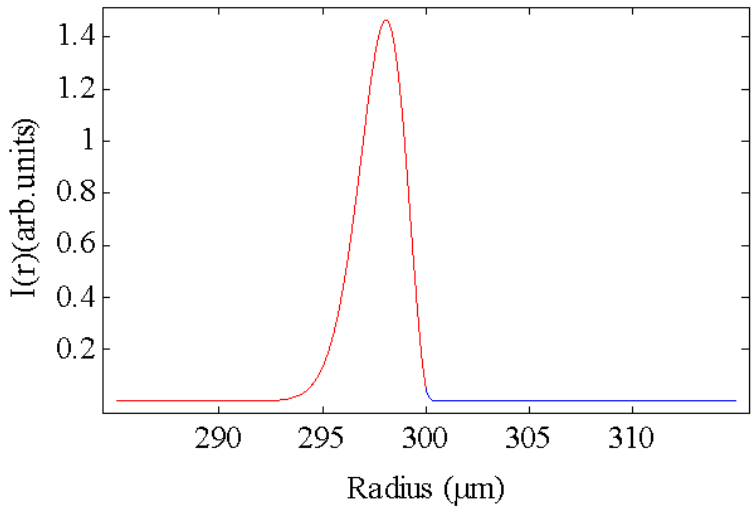


Figure 28. The mode profile for a 300 μm radius microsphere for fundamental TE mode with $q$ =1 and $l$ - $|m|$=0. The blue portion of the plot is outside the microsphere.

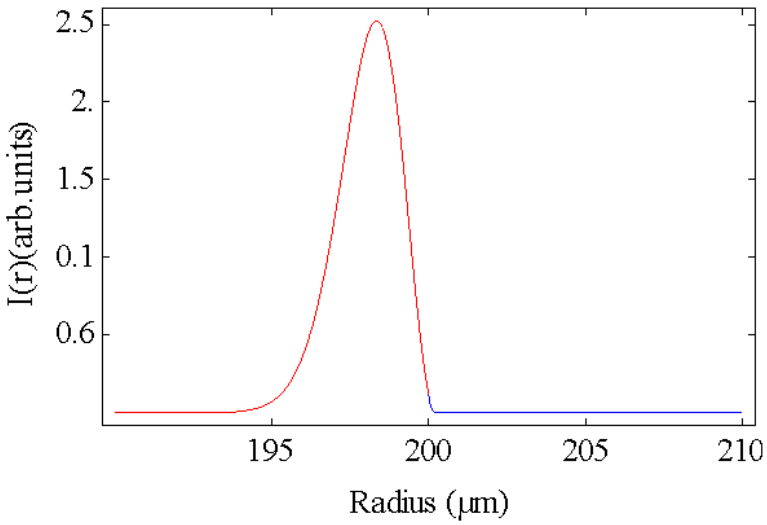


Figure 29. The mode profile for a 200 μm radius microsphere for fundamental TE mode with $q$ =1 and $l$ - $|m|$=0. The blue portion of the plot is outside the microsphere.

From Fig. 29 for a microsphere of 200 μm at $\lambda$ = 1550 nm, $f$ = 0.00234 and $f_l$ = 2.82 × $10^{-6}$. Similarly for a microsphere of radius 400 μm at the same wavelength $f$ = 0.00116 and $f_l = 1.43\times10^{-6}$.

This last case is almost the same as in Fig. 18, where $\alpha_{abs} = 0.0592\ m^{-1}$. Dividing by $\alpha_b = 800\ m^{-1}$, this gives a measured mode fraction of $7.4 \times 10^{-5}$. Using Eq. (14) this was found to represent 1.07 monolayers of water. However, using our method, where one monolayer gives $f_l = 1.43 \times 10^{-6}$, the measured mode fraction represents 52 monolayers, a factor of 48 larger. There is large disagreement between our experimental results based on Eq. (14) (though our deduced water coverages seem to be reasonable) and our estimation of the surface layer mode fraction. The discrepancy still needs to be resolved.

## III.6. Conclusions

In conclusion, the thermal bistability technique permits the measurement of the absorption coefficient of a surface film or water layer, and it can be applied to a wide variety of thin films with arbitrary refractive index. Since these measurements can easily be done with various gases, using different surface coatings of thin films, a large number of gas-surface interactions can be studied. The precision of these measurements is quite good (< 2%), so the prospect of using these techniques for thin-film characterization is promising. The strength of the observed thermal bistability gives us the heat supplied by the fraction of total optical power lost due to absorption. The results provide insight into the relative importance of surface scattering and absorption in these structures. This absorption results from a water layer on the surface of a bare sphere, and for a coated sphere it is due to the thin film. This method can be used for sensing applications, surface chemistry studies and to know the contaminants present on the surface.

# Chapter IV

# GOLD NANOROD SYNTHESIS

## IV.1 Introduction

The shapes of nanoparticles greatly influence their optical and electronic properties. Nanoscale materials have been used in biological systems, where many proteins are a few nm in size [48]. Growth methods for gold nanorods (NRs) have drawn a lot of attention as they are used for biological applications like sensing of sequence specific HIV-1 virus DNA by using hyper-Rayleigh scattering spectroscopy, identity profiling of cell surface markers by multiplex gold NR probes, and many other biological and sensing applications [49-51]. The shape of a gold NR is defined by its aspect ratio (AR, length/diameter). Localized surface plasmons (SP) are standing waves of coherent fluctuations of electron charges along the metal-dielectric boundary. When the frequency of incident light matches that of a localized SP, it leads to so-called surface plasmon resonance (SPR) phenomena. These gold NRs exhibit two peaks, a longitudinal surface plasmon peak, and a transverse surface plasmon peak. As the AR of the gold NRs increases, the energy separation between the two peaks increases. The AR of the gold NRs can be controlled in wet chemical synthesis by varying the ratio of seed to metal salt concentrations as well as the time delay between steps of the synthesis [52]. The gold NRs can be grown directly on the surface [53] or they can be prepared by seed-mediated

wet chemical reduction [54-57]. The above two methods were tried in our lab; the first method will be discussed briefly, as it was attempted without much success as a follow up to [53] done earlier in the lab; the second technique of growing rods using the wet chemical method will be discussed in detail and this procedure is based on Murphy's recipes [54-56], with slight modifications in the growth conditions. There are many other methods used to grow gold NRs, for example by electrochemical deposition in templates or photochemical synthesis [58, 59]. Murphy's method of growing rods in solution requires many rounds of filtration as the solution will contain spheres and platelets depending on the number of steps in the seed mediated method. The section on filtration methods will discuss these aspects in detail. Gold NRs were grown in our lab with ARs ranging from 2.5 to 19.0, using a combination of methods discussed in the literature. The growth of high-AR gold NRs involves many steps and careful control of the growth conditions. The following three sections describe the methods used for synthesis, characterization, and purification of NRs, and are followed by some conclusions.

## IV.2 Synthesis Methods

All the chemicals obtained from commercial suppliers are listed below and are used without further purification. Cetyltrimethylammonium bromide (CTAB, 99+ %), hydrogentetrachloroaurate (111) trihydrate ($HAuCl_4$, 99.9%), ascorbic acid (AA, 99+ %), sodium borohydrate (99+ %), heavy water, PDDA and silver nitrate (99+ %) were purchased from Sigma–Aldrich. Sodium citrate (99%) was purchased from Alpha-Aesar. Sodium hydroxide and all basic lab supplies like gloves and beakers were purchased from the chemistry store at Oklahoma State University. Ultra-pure deionized

(DI) water of resistivity 18.2 MΩ (actually, MΩ·cm) was used for preparing aqueous solutions and for rinsing the glassware before experiments.

**Direct growth of gold NRs on surface of fused silica microresonator**: The surface is dipped in an aqueous solution of PDDA for 15-20 minutes. After washing with DI water, it is dried for a while in the atmosphere and dipped in a solution of HgTe nanoparticles (NPs). The negatively charged HgTe capping agent adheres well to the positively charged PDDA. Then the substrate is dipped in a gold growth solution consisting of $1.3x10^{-4}$ M $HAuCl_4$, 8.3 x $10^{-3}$ M CTAB and 1.9 x $10^{-4}$ M AA. This method has many disadvantages over the growth of gold nanorods in solution. There is no control over the yield and the yield is less compared with the wet chemical synthesis method. The AR of the gold NRs cannot be varied, and is about 4 ± 2. The characterization of the gold NRs is not possible, without growing them on the substrate. The gold NRs cannot be isolated from other structures. The HgTe seeds are not easy to prepare nor easily available, and their aggregation with time will lead to poor growth results. The above stated several disadvantages, in addition to the cost, made us go for the wet chemical synthesis method. Having good knowledge of and control over the surface charge properties will make adhesion of gold NRs on any surface possible.

**Wet chemical method (gold seed growth):** This is the first step in any solution-based growth method involving gold seeds. A 0.5 mL solution containing 0.01M $HAuCl_4$ trihydrate in water is added to 0.5 mL of 0.01M sodium citrate in water, and then 18 mL of DI water is added to the above and stirred well in a conical flask. While the solution is stirred, 0.5 mL of ice cold 0.1M $NaBH_4$ was added and the solution color changes from colorless to orange with the growth of the seeds. The seed solution should be used

within 2-6 hrs after preparation. The seed size varies from 3.5 ± 0.7 nm. Here the citrate serves as a capping agent; CTAB can also be used as a capping agent [57] to have better control the size of low-AR gold NRs. This citrate based seed recipe is used for the high AR gold NR growth discussed below.

**Preparation of 3.5 ± 1 AR gold NRs**: In this method Au seeds are prepared as discussed in [56], slightly different from the above method with the final seed solution having a pale brown-yellow color, probably due to formation of seeds of a different size. Then 4.75 mL of 0.1 M CTAB, 0.20 mL of 0.01 M $HAuCl_4$, and 0.030 mL of 0.01 M $AgNO_3$ solution are added one by one in the above order and followed by gentle inversion. It is very important to use clean containers to prevent aggregation.

In the last step, we add to the solution, which is bright yellow in color, 0.032 mL of 0.10 M AA. The solution turns colorless on repeating the gentle inversion method. The solution is left undisturbed for 3-4 hrs. We have obtained very high yield, close to the 95% specified for the ones we purchased from Nanopartz before trying this method.

**Preparation of 13.0 ± 2 AR gold NRs**: In this process we combined two recipes of Murphy [54, 55] to improve the yield in the case of growth of high AR rods. The high AR gold NR synthesis is not a single-step but a three-step process. Take three beakers or test tubes and label them (A, B and C), each containing 9 mL of growth solution of $2.5 \times 10^{-4}$ M $HAuCl_4$ and 0.1 M CTAB mixed with 0.05 mL of 0.1 M AA.

In the first step add 1.0 mL of 3.5 nm seed solution to sample A while stirring. The color of the solution turns red within 2-3 minutes. In the second step, after 4-6 h, 1.0 mL of solution from A is added to B while stirring. The color of the solution turns red in 2-5 minutes. Again in the last step, after 4-6 hrs, 10.0 mL from B is mixed with C

and the solution turns red within 8-10 minutes. The yield was around 30%, comparatively less than what we expected.

**Preparation of 15 ± 4 AR gold NRs**: The yield is significantly improved in this method that combines recipes, but produces a wide distribution in AR. Label three flasks as A, B, and C. The growth solution in A and B contains 9 mL of 0.1 M CTAB in water, 0.25 mL of 0.010 M $HAuCl_4$ trihydrate in water, and 50 μL each of 0.1 M AA and 0.1M NaOH. Growth solution C consists of 90 mL of 0.1 M CTAB, 2.5 mL of 0.01 M $HAuCl_4$, and 0.5 mL each of 0.1 M AA and 0.1M NaOH. Finally, 1 mL of seed solution is added to growth solution A. This solution was shaken for 3-5 seconds and 1.0 ml of A is added to B after 4-5 hrs and shaken for 3-5 seconds and the entire solution of B is poured into C after 4-5 hrs. The solution C, which turns reddish-brown, is left undisturbed overnight. The yield for this solution is around 50%.

**Preparation of 16 ± 3 AR gold NRs, long process:** Another process discussed in [60] is used to grow gold NRs, in hopes of improving the yield and reducing the size distribution. The methodology is slightly different from the others discussed above. Here the synthesis is performed in larger volumes. This method relies on gravitational sedimentation for separation of rods from other structures by leaving the solutions for several hours. It takes almost a week to complete the synthesis procedure. The density of growth solution is higher than in the previous methods. The gold seeds are prepared in the same way as discussed in the previous high AR gold growth processes. After the gold seeds are prepared, in a 2 L flask, 64.06 g of CTAB is dissolved in 880 mL of DI water and heated gently to prevent any aggregation of CTAB. In a separate flask, 173.4 mg of $HAuCl_4$ is dissolved in 880 mL of water and then added to the CTAB solution. In

the next step, the prepared solution is placed in amounts of 45 mL, 140 mL, and 1575 mL in three flasks labeled as A, B and C respectively.

Next, by dissolving 176 mg of AA in 10 mL of water, 0.1 M AA solution in DI water is prepared. Then add 0.25 mL, 0.77 mL, and 8.75 mL of this AA solution into flasks A, B, and C, respectively. The solutions in all three flasks become colorless after gentle inversion. The same three step process discussed previously is followed for these larger quantities. In the first step, 4 mL of seed solution is added to flask A and gently mixed. Then 12.4 mL of the resulting mixture is transferred from flask A to flask B within 4-6 seconds and gently mixed by stirring the flask. Next transfer all of the content of flask B into flask C as quickly as possible. The solution in flask C is left undisturbed for about 30 min and its color changes to dark red. The gravitational sedimentation process is done by leaving flask C undisturbed for at least 14 hours at room temperature. High AR gold NRs along with platelets precipitate from the solution, forming a thin film barely noticeable at the bottom of the flask. The supernatant, containing mostly spheres, is removed from the flask. The film at the bottom of flask, containing high AR gold NRs, is redispersed into 10 mL of 0.1 M CTAB solution to prevent aggregation of the gold NRs. The yield of gold NRs obtained is $\leq 55\%$.

In the last part of this section, the theory behind the growth of NRs will be discussed. The growth of NRs is initiated by the surfactant-capped Au seeds. When CTAB is added to $HAuCl_4$ it forms CTA-$AuBr_4^-$, which reduces to CTA-$AuBr_2^-$ upon the addition of AA. The addition of seeds further reduces the solution from $Au^-$ to $Au^0$ leading to gold deposition on the gold seeds, causing them to grow [52]. Similar to AA, $NaBH_4$ serves as reducing agent in gold seed formation. The most important constituent

in the NR growth is CTAB (Fig. 30), which serves as a directing agent in the formation of NRs and once gold NRs are formed it caps them to prevent aggregation. The concentration of CTAB is important, because by varying its concentration we can grow NRs of different sizes [56].

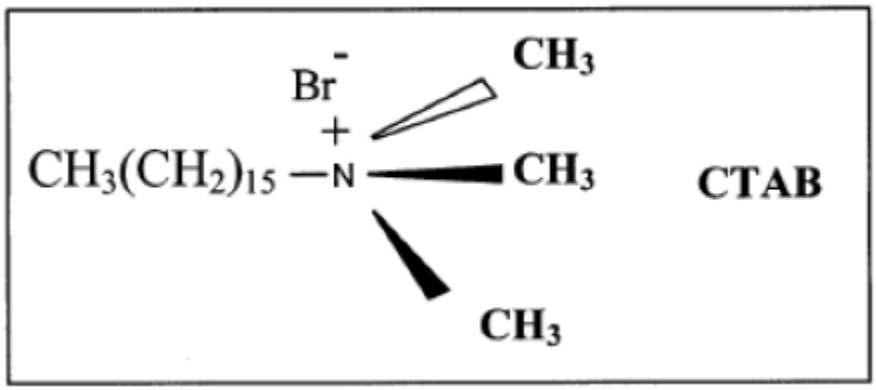


Figure 30. Structure of CTAB molecule reproduced from [57].

The silver nitrate used in growing low-AR gold NRs forms AgBr in the presence of CTAB and helps CTAB in restricting their growth to rod shape. NaOH is used in the high-AR gold NR growth process to improve the yields; with its addition the pH of the growth solution increases to 3.5, resulting in the increase in the proportion of high-AR gold NRs [54].

## IV.3 Characterization Methods

In this section methods for characterization of gold NRs will be discussed in detail. The gold NRs are characterized using absorption measurements and microscopy. The optical absorption spectrum was obtained from a Cary 5 UV/Vis/NIR

spectrophotometer using DI or $D_2O$ solutions of CTAB-stabilized gold nanostructures. Transmission electron microscopy (TEM) was performed at 200 kV using a JEOL JEM-2100, scanning electron microscopy (SEM) was performed using an FEI Quanta 600 field emission gun, energy-dispersive X-ray analysis was done with the Evex Nanoanalysis EDS system of the TEM, and Atomic force Microcopy (AFM) was performed using Veeco Multimode SPM with conductive AFM module and heating/cooling stages.

To collect the absorbance spectra of the gold NR solution, the spectrometer is scanned in wavelength from 300 to 1500 nm. First one scans a blank of pure solvent (DI water or $D_2O$) to obtain a baseline reading. Next the gold NR solution is scanned. The sample is prepared for TEM by holding a TEM grid at the edge using tweezers and depositing 3-6 μL of the gold NR sample onto the center of the grid using a micropipette, then letting it dry for 20-25 minutes.

Figure 31 shows TEM images of gold NRs grown in-house using the synthesis methods discussed in the previous section, with AR 2.5 ± 1 and AR 3.5 ± 1. The yields are high, > 90%. Figure 32 shows the TEM images of high-AR gold NRs grown in-house from the synthesis methods discussed in the previous section, with AR 13 ± 2 and AR 15 ± 4. The yields are lower; 25-35% for AR 13 ± 2 and 50-60% for AR 15 ± 4.

(a)

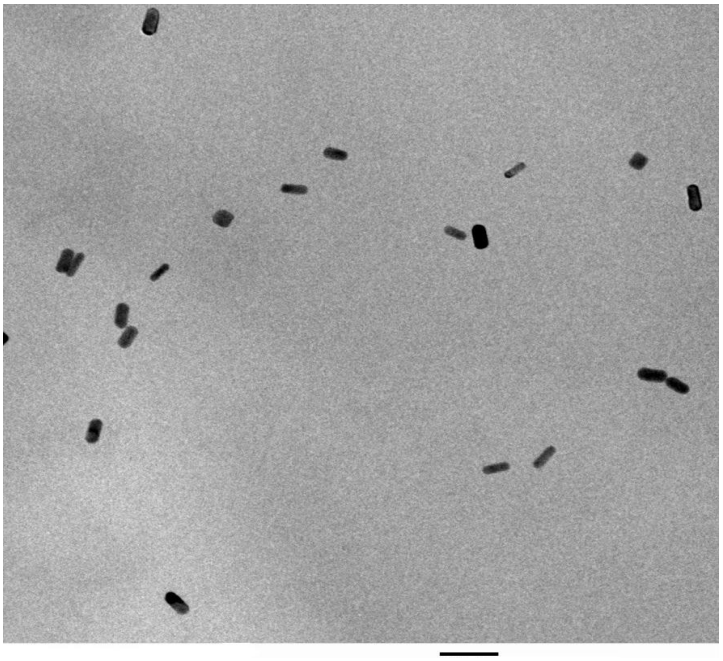

(b)

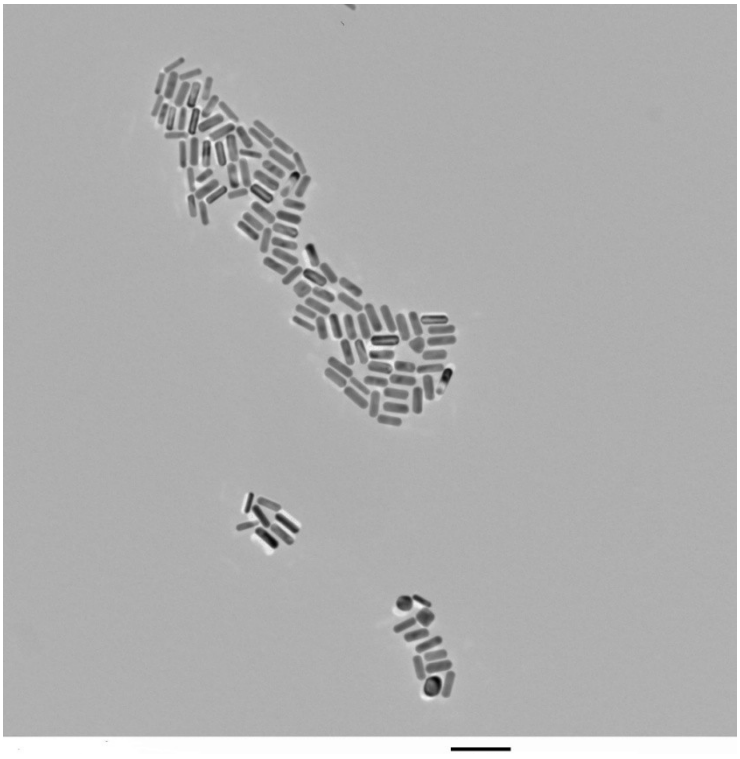

Figure 31. TEM images of gold NRs. (a) AR 2.5 ± 1. (b) AR 3.5 ± 1. All images are taken at 20000 magnification; all scale bars are 100 nm.

(a)

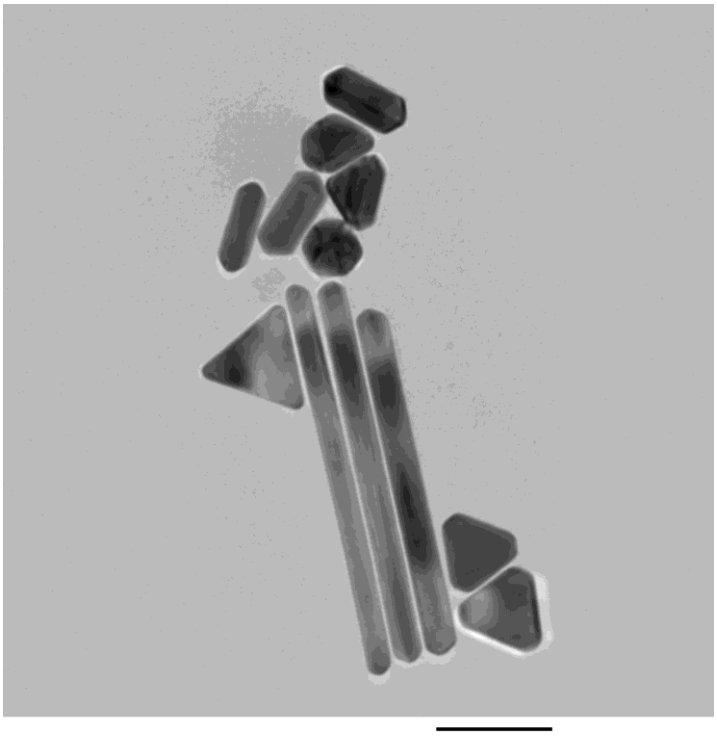

(b)

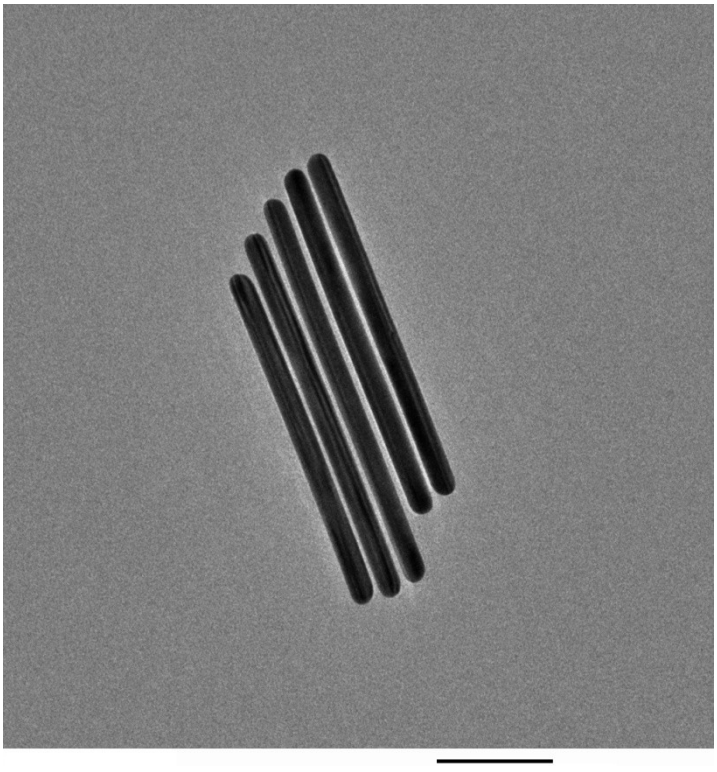

Figure 32. TEM images of gold NRs. (a) AR 13 ± 2. (b) AR 15 ± 4. All images are taken at 40,000 magnification; all scale bars are 100 nm

Figure 33 (a) shows a high resolution TEM image of gold seeds 3.5±0.7 nm, grown in the lab. Figure 33 (b) shows a high resolution TEM image of a low-AR gold NR, grown in the lab. The dark shades in the figures are structures of interest. We can see crystal lattice structure in the images, as gold NR formation results in different crystal planes ({110}, {111}, {100}) on their surfaces. The NRs are mainly enclosed by {100} and {110} facets and their axial growth direction is <100> [52].

The TEM has two different modes of operation: they are imaging mode and diffraction mode, which is also called selected area diffraction. The previous TEM images are taken in imaging mode. Figure 34 shows the image of a gold NR in diffraction mode.

Operation in diffraction mode is used to determine whether a specimen is single crystal, polycrystalline, or amorphous. This will be used to identify the crystal lattice structure and measure the lattice parameter. The white spots on the image indicate that it is single crystal. This electron diffraction using TEM is mainly used for characterizing the internal structure of materials, and is sensitive to tiny defects on the order of nm scale in the structures.

(a)

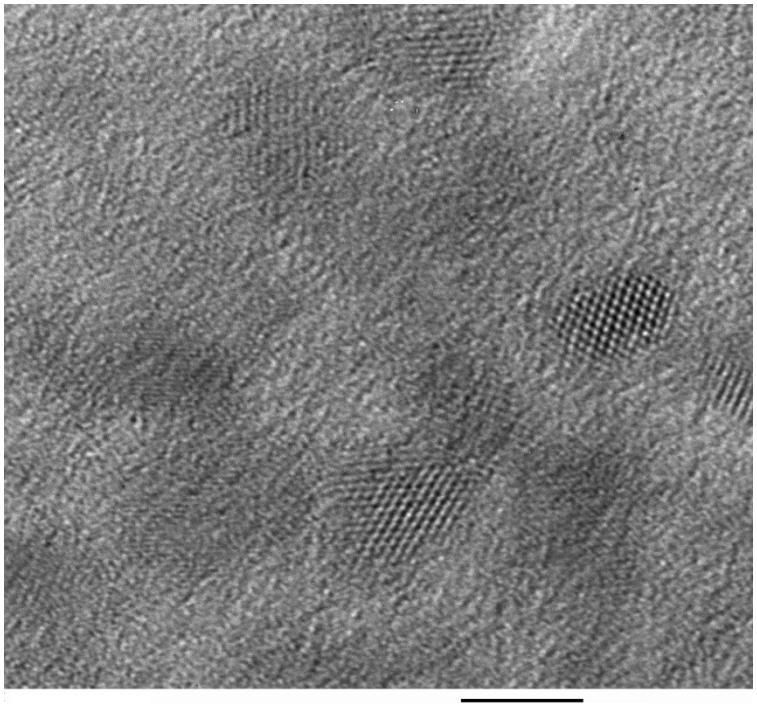

(b)

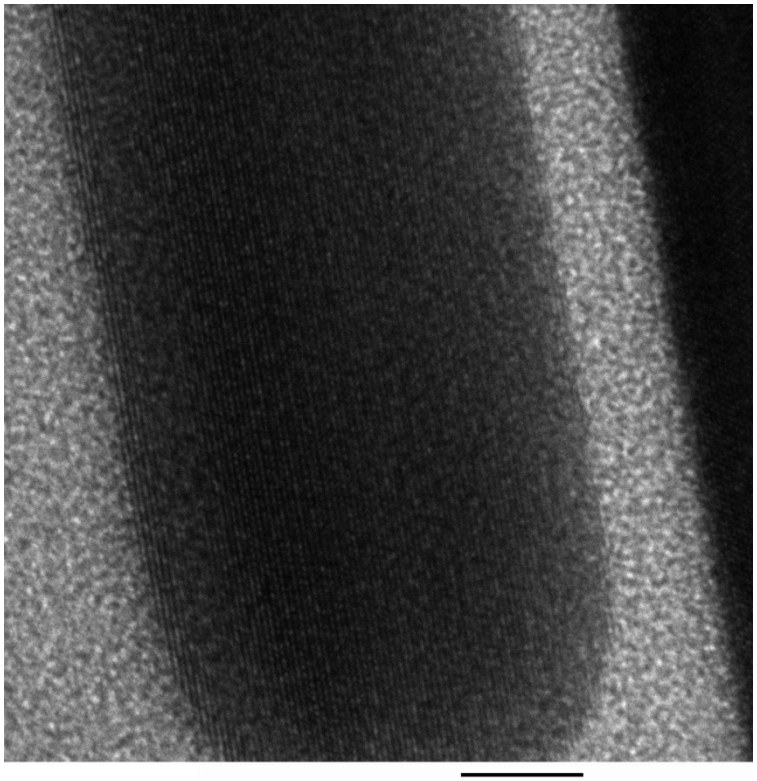

Figure 33. High resolution TEM images. (a) Gold seeds. (b) Gold NR. All images are taken at 80,000 magnification; all scale bars are 5 nm.

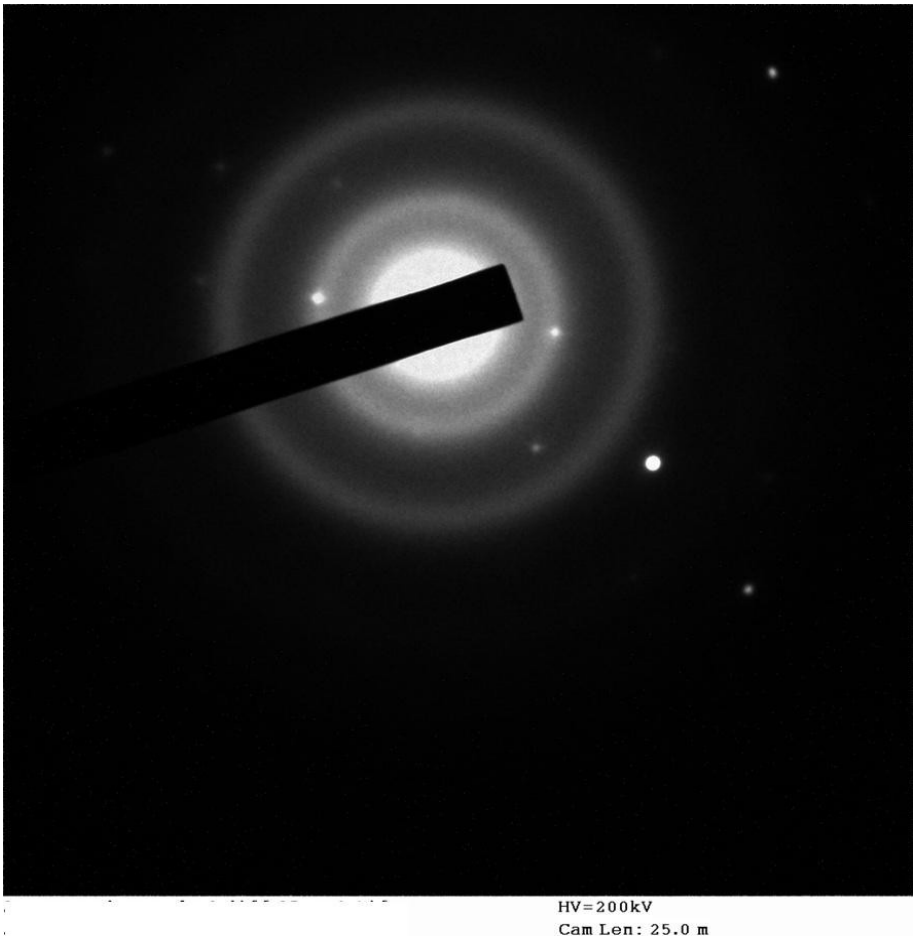


Figure 34. Diffraction mode TEM image of a gold NR.

The presence of gold on the surface was confirmed by energy dispersive X-ray analysis (EDX) (Fig. 35). The surface shows Au peaks (2.13 keV, 9.7 keV and 11.91 keV) along with peaks of all elements present on the TEM grid.

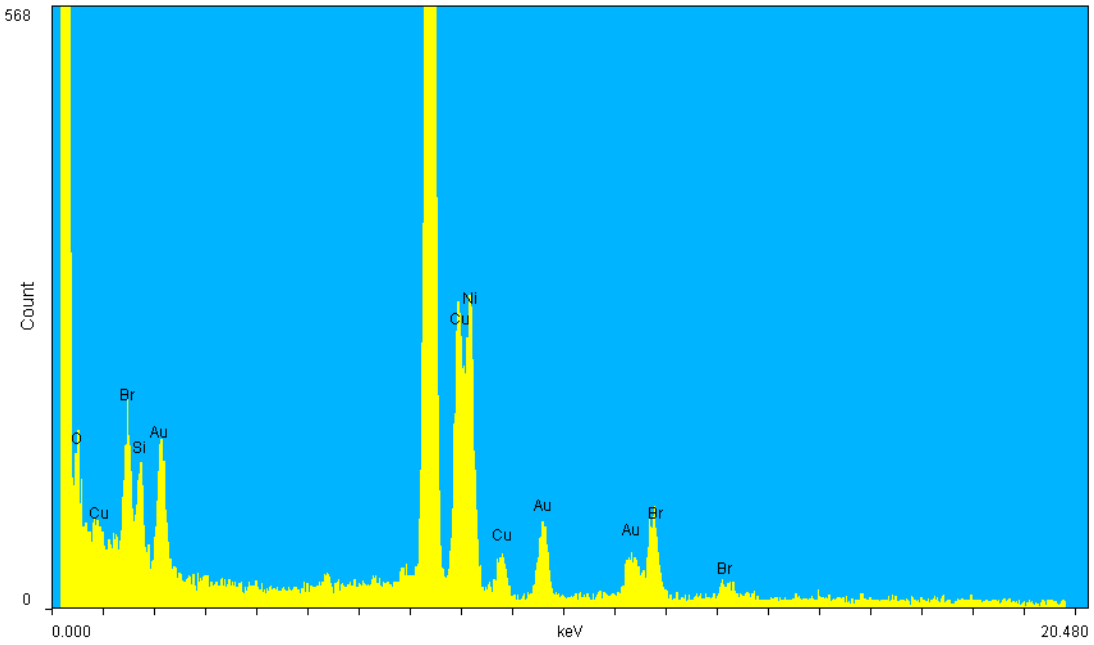


Figure 35. EDX taken on the surface of TEM grid made of nickel, copper, and coated with gold NRs.

Figure 36 shows an SEM image of gold NRs grown directly on a fused silica microresonator using HgTe seeds obtained from Dr. N. Kotov's group. This process is not repeatable and the HgTe seeds aggregate with time. The yield of rods is relatively low, <20%, even when we had unaggregated seeds [53]. Figure 37 shows the section analysis done on an AFM height image to obtain an indication of the size dispersion of the gold NRs grown on the surface of a fused silica microresonator. The vertical distance of 1-3 nm in the AFM image is equivalent to the diameter in the TEM image.

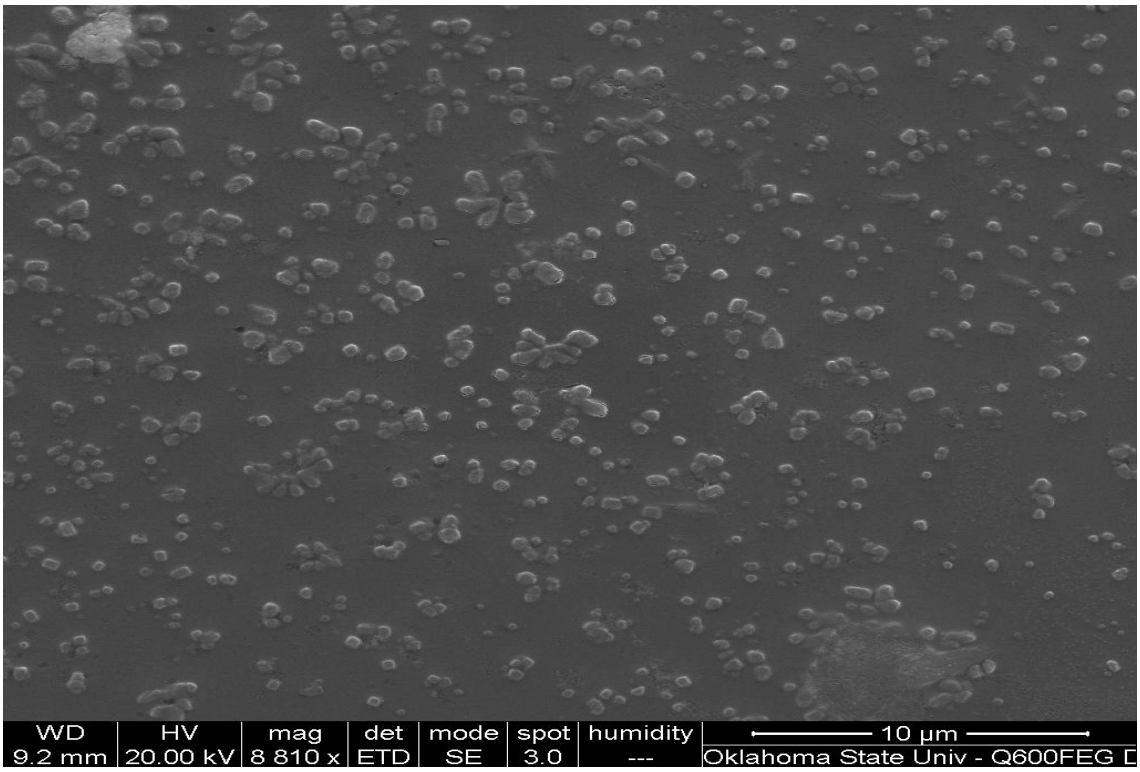


Figure 36. SEM image of gold NRs grown directly on the surface of a silica microresonator.

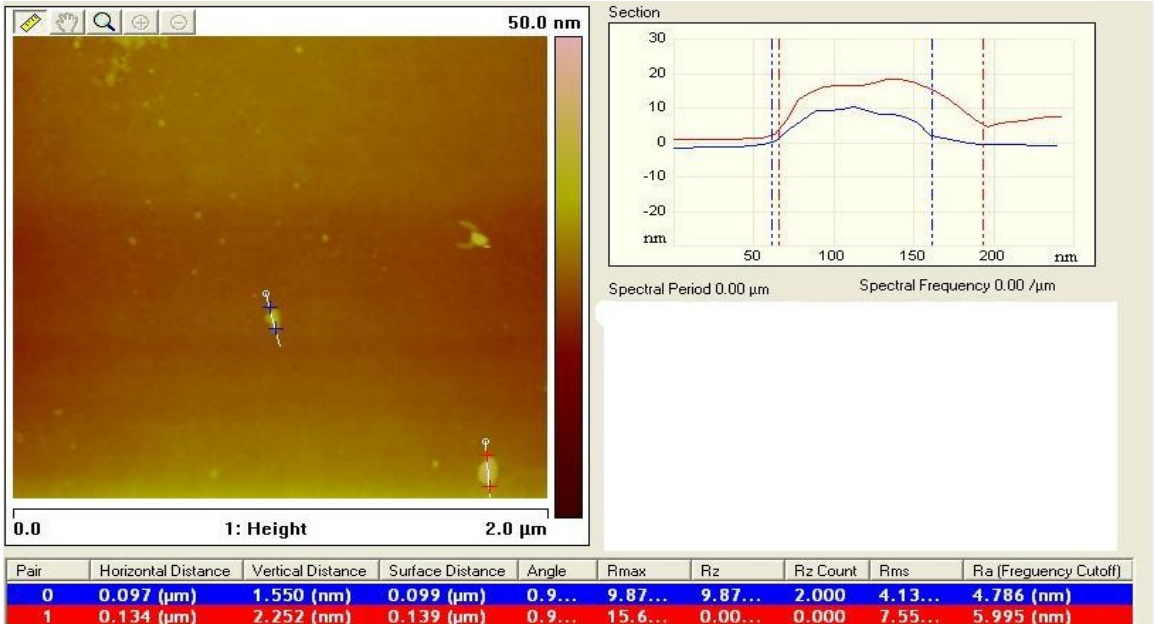


Figure 37. AFM height image with section analysis for gold NRs grown directly on the surface of the microresonator.

The next important and commonly used technique for characterization of gold NRs is obtaining absorption spectra using the Cary spectrophotometer**.** The basic concept behind absorbance spectroscopy involves the Beer-Lambert law. The absorbance is measured using a spectrophotometer, which determines the change in transmitted light intensity as the wavelength of light is varied from 400 nm to 2000 nm. The equation relating the transmitted light $I$, to the absorbance is as follows:

$$A = \log_{10}\left(\frac{I_0}{I}\right), \tag{22}$$

where absorbance $A$, is a measure of the amount of light absorbed by a material, $I_0$ is the intensity of light entering the sample, and $I$ is the intensity of light exiting the sample

In the case of a dilute solution, absorbance is given by the Beer-Lambert Law:

$$A = \varepsilon(\lambda)\, C\, L. \tag{23}$$

Where $L$ is the path length in cm, $C$ is the molar concentration of the material absorbing (NRs in our case) in M and $\varepsilon(\lambda)$ is the extinction coefficient or molar absorptivity in $cm^{-1}M^{-1}$, strongly dependent on the wavelength of the light or laser used. Figure 38 illustrates the concept described by Eqs. (22) and (23).

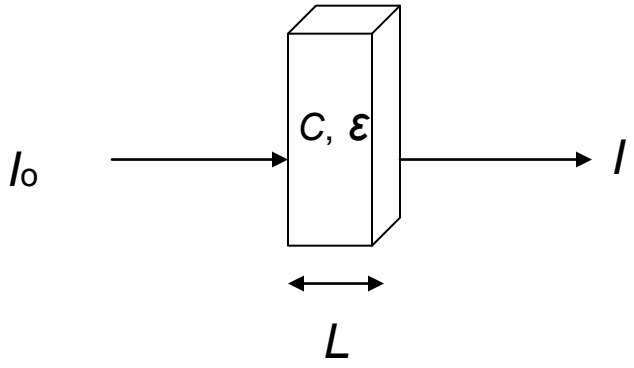


Figure 38. Schematic of a cuvette to determine absorbance of a dilute solution.

Gold NRs can have surface plasmon resonances (SPR) in either the longitudinal or transverse directions. The transverse plasmon gives an absorption peak at around 520 nm, while the longitudinal surface plasmon resonance peak can be between 600 nm and 1000 nm for low-AR gold NRs, as seen in Fig. 39. Figure 39 shows that an increase in AR has only a small effect on the transverse peak, but red-shifts the longitudinal peak. A small artifact is seen in the longitudinal peak due to filter change in the Cary.

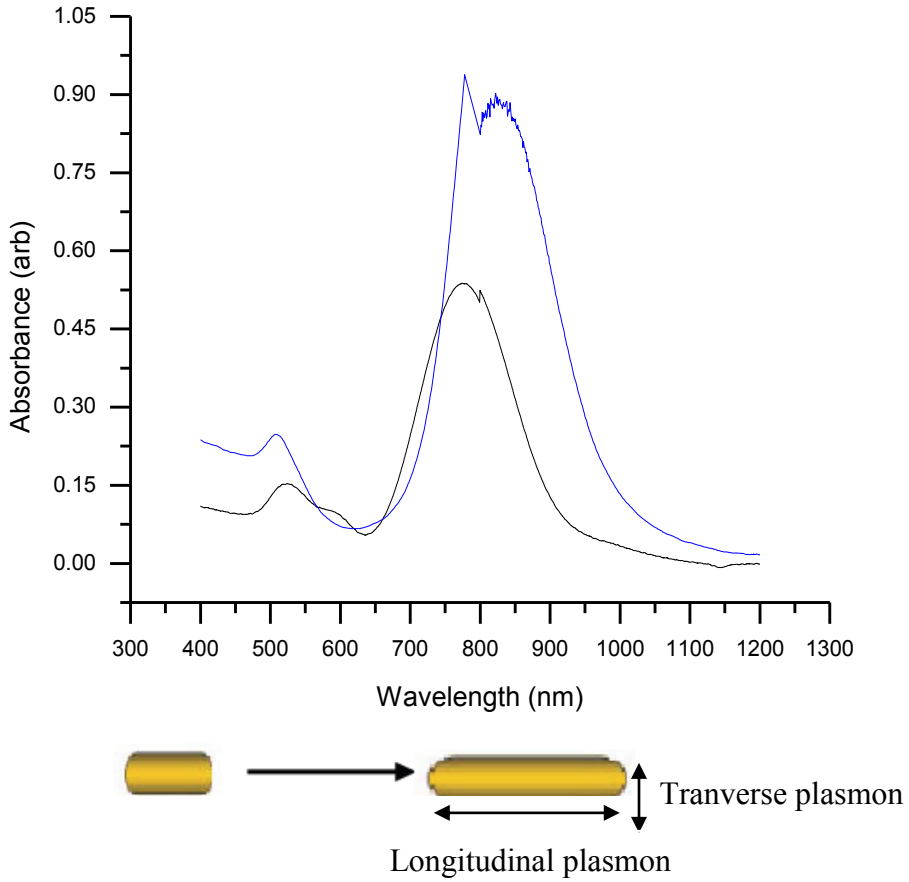


Figure 39. Absorption spectra of two sets of gold NRs with different AR; 3.8 ±1 in black and 4.5 ± 1 in blue.

High-AR gold NRs have plasmon peaks which will be partially masked by water absorption peaks, as water has strong absorption in the NIR. We tried reducing the size of cuvette as in the literature [61] and we were able to reduce the water absorption peaks, but the absorption features of high-AR gold NRs are still not clean, due to interference. Next we tried a method discussed in the literature [60]. The NRs are redispersed into 10 mL of 0.1M CTAB solution in $D_2O$. After 2-3 rounds of centrifugation and redispersion in CTAB, an absorption spectrum was taken using the Cary, without any success. This was due to conversion of $D_2O$ to HDO on an hour time scale, which was verified experimentally. Absorption measurements taken for two batches of high-AR rods grown by the long process [60] and the short process described in the previous section give broad spectra indicating the presence of high-AR rods of varying sizes. However, sharp longitudinal peaks as seen with low-AR NRs were not seen in the expected wavelength range of 1450-1800 nm.

The modeling of absorption spectra has been studied using an extension of Mie's theory by Gans [62]. Here we assume the NRs are ellipsoids; TEM images show them to be cylinders, but no analytical expression exists for that. We calculate the absorbance of light using Gans' formulae [62].

$$\frac{\gamma}{N_p V} = \frac{2\pi\varepsilon_a^{3/2}}{3\lambda} \sum_{j=A}^{C} \frac{(\frac{1}{P_j^2})\varepsilon^2}{[\varepsilon_1+(\frac{1-P_j}{P_j})\varepsilon_a]^2+\varepsilon_2^2} \quad , \tag{24}$$

where $V$ is the single particle volume, $N_p$ represents the number concentration of particles, $\lambda$ is the wavelength of light in vacuum, $\varepsilon_1$ and $\varepsilon_2$ are the real and imaginary parts of the complex refractive index of the particles, $\varepsilon_a$ is the dielectric constant of the

surrounding medium, in our case water, and $P_j$ is the depolarization factor. The expression for $P_j$ along the A, B, and C axes for elongated ellipsoids (i.e., prolate spheroids) is given by [62]

$$P_A = \frac{1-e^2}{e^2}[\frac{1}{2e}\ln(\frac{1+e}{1-e}) - 1], \tag{25}$$

$$P_B = P_C = \frac{1-P_A}{2}, \tag{26}$$

where ellipticity

$$e = [\frac{L^2 - d^2}{L^2}]^{1/2}, \tag{27}$$

and $L$ and $d$ are the major and minor diameters of the ellipsoids. The complex refractive index for bulk gold is obtained from the literature [63]. The absorption spectra are calculated and plotted from above expressions for 2.9, 3.8, 4.5, 7.0, 11.0 and 13.0 AR gold NRs, as shown in Fig. 40. The external medium is taken to be water as the NRs are suspended in DI water. As the AR of the gold NRs increases from 2.9 to 13.0, the longitudinal SPR peak shifts towards longer wavelengths. Theoretical and experimental values of the longitudinal resonance wavelengths are compared and tabulated in Table 4.

For higher AR gold NRs Gans' method or the discrete dipole approximation (DDA) methods [64] are about 20-40 nm off in predicting the longitudinal SPR peaks compared with the experimental values [52].

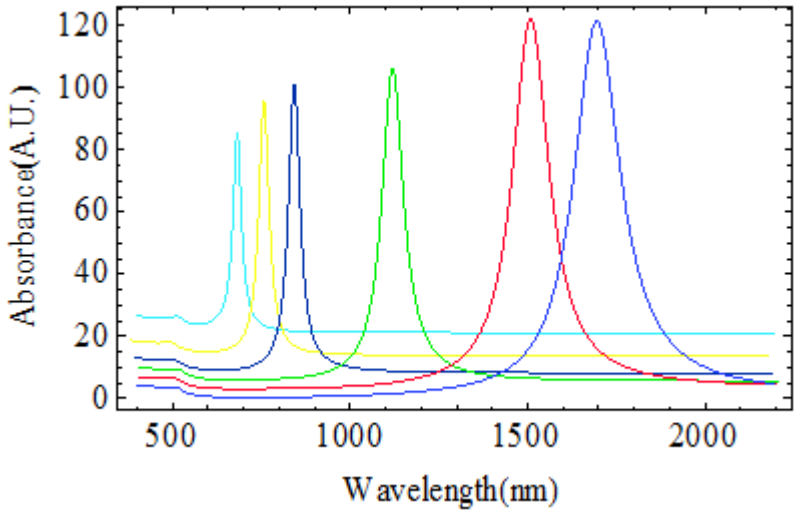


Figure 40. Absorbance vs. wavelength using Gans' method, for the ARs 2.9-13.0 gold NRs.

| AR of Gold NRs | Theory Wavelength Gans' method (nm) | Experimental Wavelength (nm) | |
|---|---|---|---|
| 2.9 | 700 | 700 | [52] |
| 3.8 | 780 | 780 | |
| 4.5 | 850 | 850 | |
| 7.0 | 1100 | 1100 | [52] |
| 11.0 | 1550 | 1500 | [52] |
| 13.0 | 1750 | 1780 | [52] |

Table 4. Comparison of longitudinal SPR wavelengths for various AR gold NRs in water.

## IV.4 Purification Methods

The gold NR solution also contains different structures like spheres and platelets. The low-AR growth solution contains < 5% other structures mostly spheres. The high AR rods synthesis produces these other components (spheres and platelets) in higher quantities. Centrifugation is used to reduce the proportion of these undesirable structures. The centrifuge used for the experiments is Biofuge 13, which can operate up to 13,000 rpm. Many other methods for purification are discussed in the literature including HPLC, diafiltration, capillary electrophoresis, and gel electrophoresis [52], but the methods discussed in this section are simpler and have a higher success rate.

The precipitation or sedimentation process involves separating the supernatant from the residue, either using a centrifuge or letting the solution separate itself by leaving it undisturbed for >24 hrs. Centrifugation can remove the majority of the spherical particles, but the remaining mixture of rods and platelets can be separated by a two step process involving reduction and centrifugation. This section discusses both methods in detail.

Centrifugation is done at different speeds, for example, for removing CTAB at 10,000 rpm 2-3 times. We can visibly inspect the vial by shaking it and no bubble formation indicates that the CTAB is separated. For removing spherical particles from high-AR gold NRs the centrifuge is operated at 2000 rpm, the top supernatant is removed and replaced with DI water, and the process is repeated 3-4 times. The low-AR gold NR solution does not require much filtration since the yield is very high. This solution is centrifuged at 10,000 rpm once or twice to separate the rods and then refilled with DI

water. The final solution is centrifuged at lower rpm (2000 to 6500 rpm) once to remove the spheres.

The theory behind shape separation in centrifugation will be discussed briefly. The ratio of the sedimentation coefficients between rods and spheres ($\beta_0$) describes the sedimentation behavior of cylindrical gold NRs and spheres and is given by [52]

$$\frac{s_o^{\text{rod}}}{s_o^{\text{sphere}}} = \frac{v_o^{\text{rod}}}{v_o^{\text{sphere}}} = \beta_0 = 6(\frac{d}{2a})^2[2\,ln\frac{L}{d} + 0.63] \tag{28}$$

where $S_0$ is the sedimentation rate, $v_0$ is the sedimentation velocity, $a$ the diameter of the sphere, $L$ and $d$ are length and diameter of the rod respectively. The square of the ratio of the diameters of rod and sphere plays an important role in separation. The log of AR or L/d, determines whether the rods or spheres sediment faster. This was verified experimentally by some groups [52].

Figure 41 is a TEM image taken of the supernatant removed by filtration and collected for imaging; the dark shade in the image is the CTAB covering the spheres. This shows that imaging is difficult with CTAB present. Figure 42 is the filtered high resolution image of low-AR gold NRs. Figure 43 shows the TEM images of the high-AR gold NRs before filtration and after going through the filtration steps described above. The yield after filtration is still <70%.

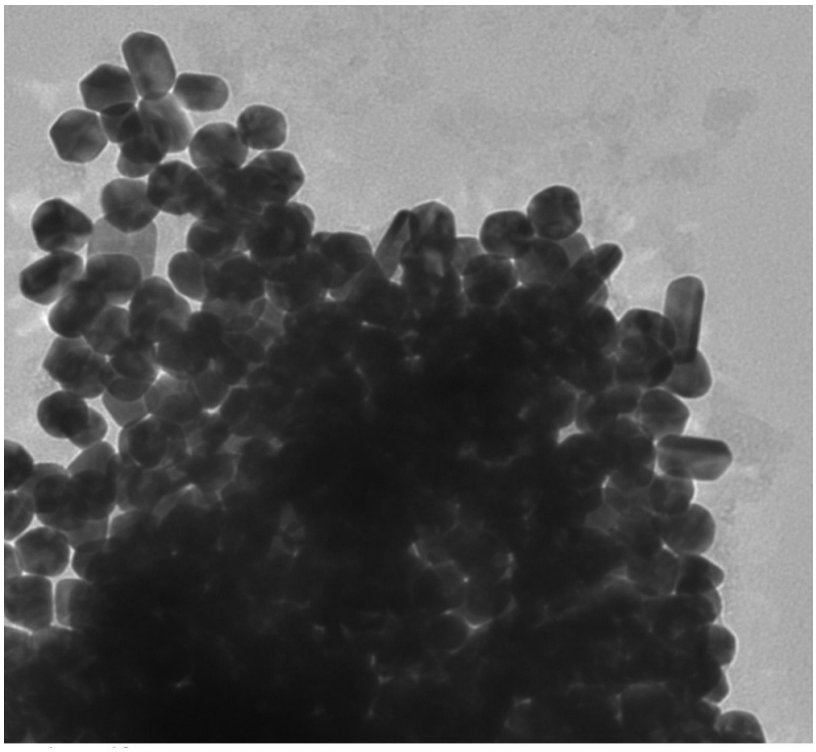

Figure 41. TEM image of supernatant removed by filtration containing spheres and CTAB. Image is taken at 40,000 magnification; scale bar is 100 nm.

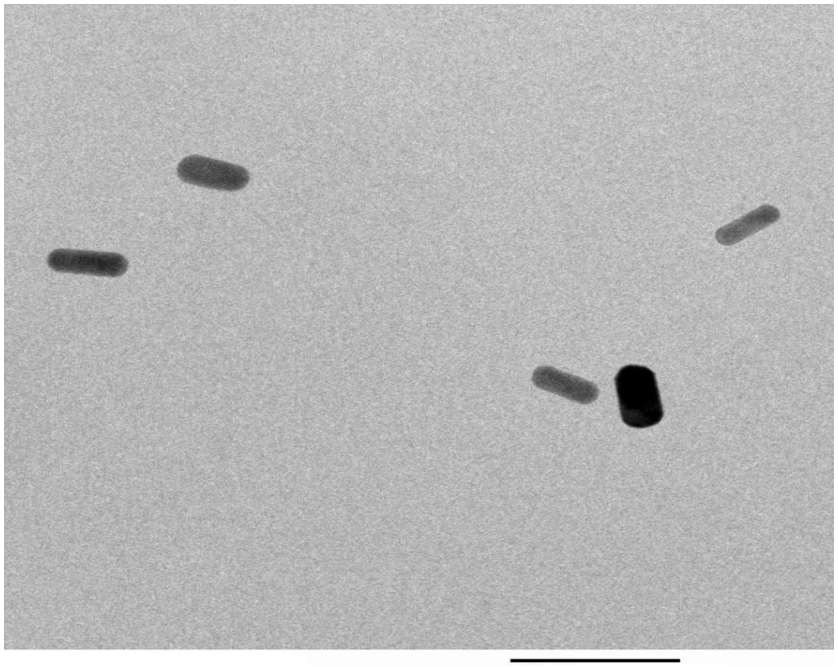

Figure 42. TEM image of low-AR filtered gold NRs. Image is taken at 50,000 magnification; scale bar is 100 nm.

(a)

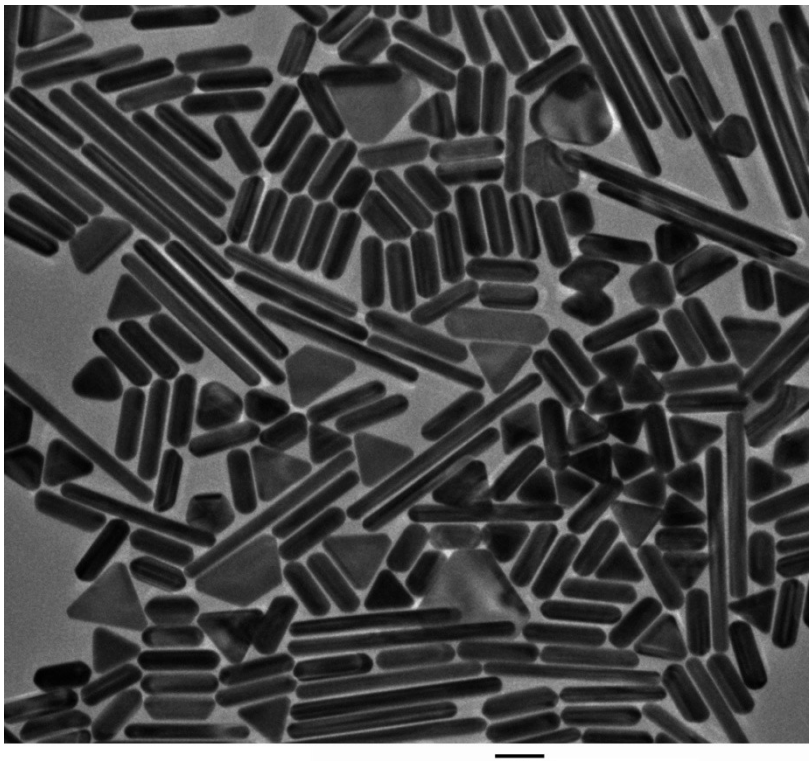

(b)

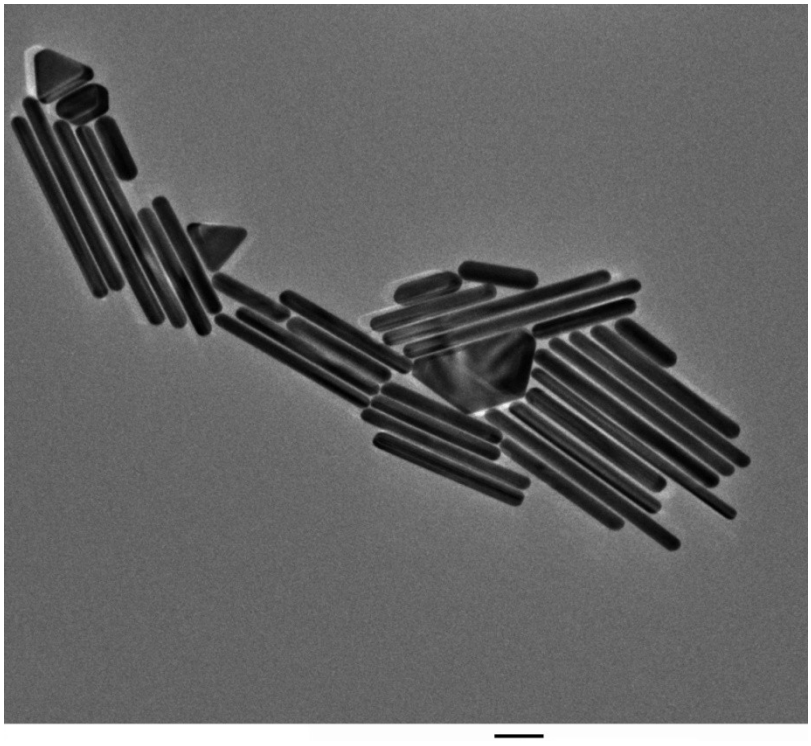

Figure 43. TEM images of gold high-AR NRs. (a) Unfiltered. (b) Filtered. All images are taken at 15,000 magnification; all scale bars are 100 nm.

Further purification of the high-AR Nr solution can improve the yield. This involves the filtration described above plus reduction as discussed by the Rice university group [60]. This reduction reaction uses a reducing agent to reduce the sizes of platelets and other structures by partial dissolution. The reduction reaction is followed by centrifugation to remove the spheres.

Take 364 mg of CTAB and 1.97 mg of $HAuCl_4.3H_2O$ in 10 mL of DI water. In the next step, 1 mL of this solution was added to the NR solution with rods and other structures to prepare the Au (III)/CTAB solution. This Au (III)/CTAB solution acts as a reducing agent for dissolution of the other structures. The solution was stirred for 5 minutes and left undisturbed for 14 hours. The high-AR gold NRs form a thin film on the bottom of the flask. The film of the precipitate was again redispersed in 10 mL of 0.1 M CTAB solution followed by addition of another 1 mL of the Au (III)/CTAB solution. This process was repeated 2-3 times.

This was supposed to give yields of >90%, but we obtained yields close to 50% for AR (13 ± 2) rods and around 80% for AR (15 ± 4) rods. Figure 44 illustrates these results.

(a)

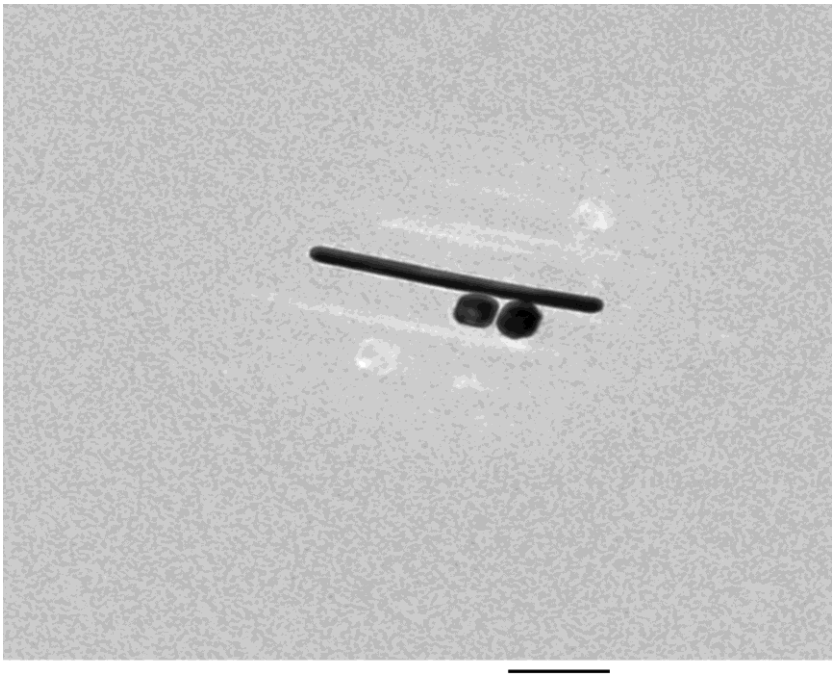

(b)

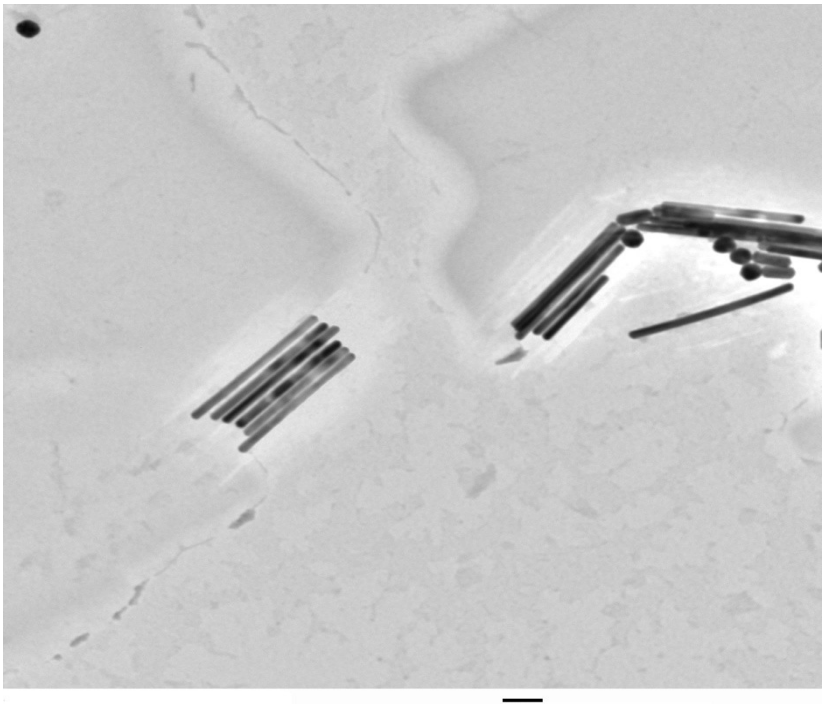

Figure 44. TEM images of gold NRs. (a) AR 13±2 taken at 30000 magnification. (b) AR 15±4 taken at 40000 magnification. All scale bars are 100 nm.

Figure 45 shows how filtration by centrifugation is successful in removing some of the structures from the high-AR gold NR solution, as seen in absorption spectra taken with the Cary spectrophotometer.

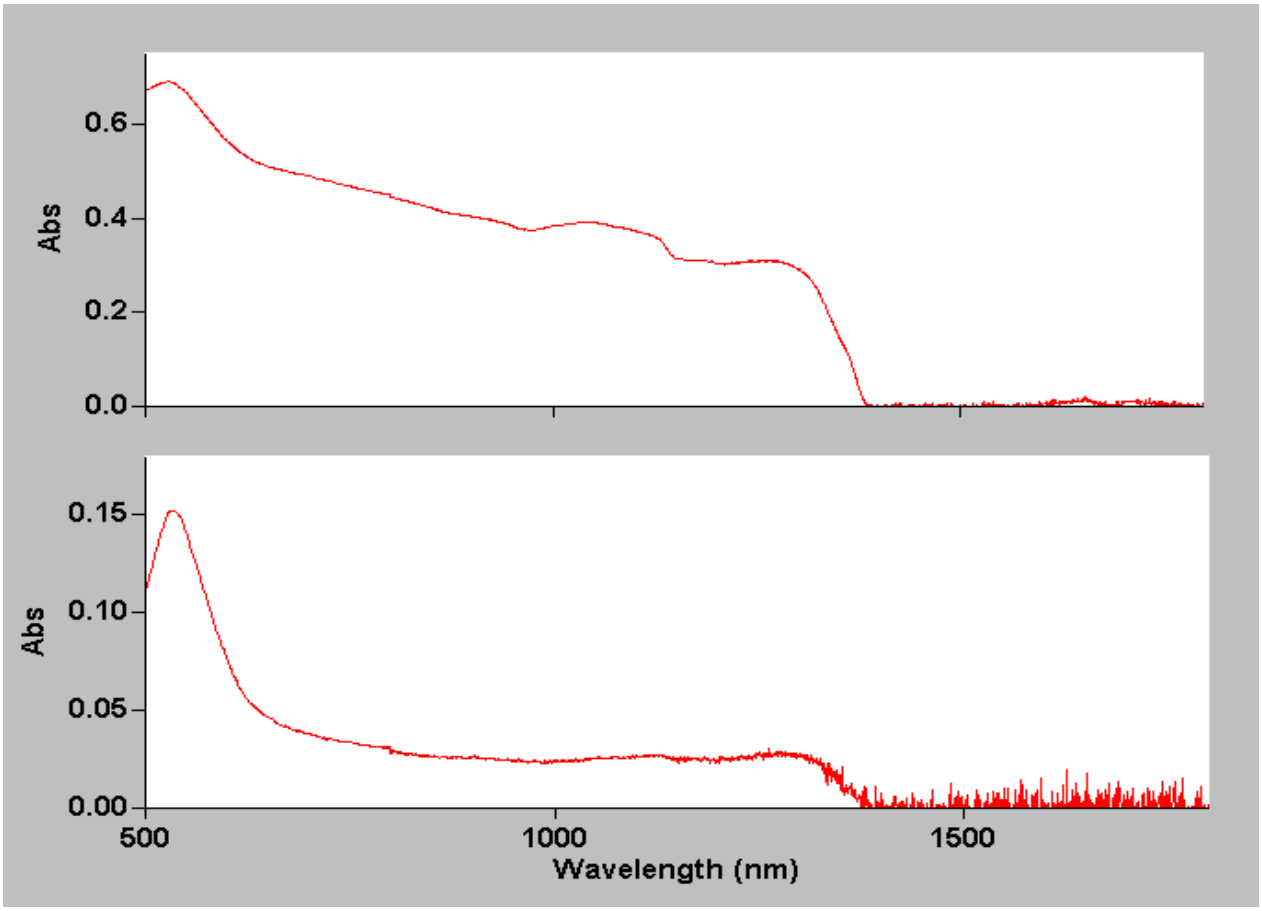


Figure 45. Absorbance high-AR NR solution: unfiltered (top) and filtered (bottom), spectra taken with Cary spectrophotometer.

## IV.5 Conclusions

In conclusion, we have found methods to grow gold NRs of different AR in solution by wet chemical synthesis methods and also by directly growing them on a surface of a fused-silica microresonator. For the seed-mediated or wet chemical method of synthesis of gold NRs the morphology of gold NRs is controlled by varying the reduction rate for low- and high-AR gold NRs. We have demonstrated that surfactants like CTAB and AA are important to get unidirectional growth of gold NRs.

Better filtration and purification methods are employed to improve the yield of gold NRs. For this we have used centrifugation of low-AR gold NRs to separate the spherical nanoparticles from the gold NR solution. We also used a combination of centrifugation and partial dissolution, using a reducing agent for shape separation in the case of high-AR gold NRs to improve the overall yield of the NRs in the growth solution.

We also explored different microscopy methods like TEM, AFM and SEM to characterize the gold NRs at different magnifications. The UV–visible spectroscopy in this study is done using a Cary spectrophotometer for absorption measurements of gold NRs. We also found that Gans' theory and other methods provide a good representation of the experimental results. These methods will let other research groups explore optical, catalytic and mechanical properties of gold NRs. These gold NRs can also be used for making gold nanowires for interconnects in the electronic circuits. These studies on controllable synthesis and better filtration methods of building NRs into a desired shape might find application in future nanoelectronics and nanodevices.

# Chapter V

# GOLD NANOWIRE ASSEMBLY

## V.1 Introduction

Nanowires (NWs) are considered essential components towards building nanoscale devices and circuitry with increased performance and greater speed [65, 66]. When we talk of shrinking processors or microchips we talk about feature size being reduced from submicron to nanometer size. The chemically inert nature and relatively low resistivity of Au makes it a suitable candidate for growing wires. Gold NWs can be grown by the wet chemical approach or the self-assembly method [67]. Other approaches require tremendous secondary processing methods with less control over shape and size distribution. In the latest development in the area, ultrathin NWs have been prepared with diameters of either 3 or 9 nm [68].

NWs can be assembled or grown between targeted points in a circuit using the dielectrophoretic approach demonstrated by our collaborative research group and other groups [67, 69, 70]. The dielectrophoresis (DEP) method of growing NWs is based on the mobility and interactions of nanoparticles (or NRs, in our case) caused by gradient alternating electric fields. This electric field allows assembly and manipulation of the NRs used to grow NWs. The same approach is being used in this chapter for growing NWs, with modifications in the experimental setup – using a much simpler setup and having the capability to grow higher AR NWs with ease, which is novel. The growth of

high-AR gold NWs with the modified dielectrophoretic approach was not observed before. Proper choice of the electrode geometry, in our case copper electrodes, is important as this arrangement produces a sharp electric gradient in front of their tips. We can also grow NWs with other metal electrodes which do not oxidize, like gold. The tips are made as sharp as possible to have stronger electric fields. Nanowires can also be grown from various other metals like indium, cobalt, zinc and lead and other semiconductors like CdTe using the methods discussed in this section. Growth of gold NWs is discussed in this chapter; we have not tried using other metals or semiconductors.

The NWs discussed in this chapter were grown primarily from NRs of AR 4.5 (Nanopartz); we were also able to grow NWs from in-house grown NRs of AR 3.5 ± 1. The NR solution is sonicated first and then centrifuged 2-3 times at 10,000 rpm to remove the majority of the CTAB. CTAB present in the gold NR solution hinders the unidirectional growth of NWs. The dielectric force is given by the following equation [69]:

$$F_{DEP} = (m\,(t) \cdot \nabla E\,(t)), \tag{29}$$

where $E$ is the electric field and $m$ the induced dipole moment of the NR given by

$$m\,(t) = \varepsilon_m\, V_p\, K\, E\,(t), \tag{30}$$

where $\varepsilon_m$ is the complex dielectric permittivity of the medium, $V_p$ is the volume of the particle and $K$ is the complex polarization factor, which depends on the complex permittivity of the particle.

The dielectrophoretic force shown above is caused due to the non-uniform electric field between the electrodes. This force causes the interaction between the dipoles in the

NRs to be directed along the electric field, leading to single–step assembly of NWs between the electrodes [70].

The expression for dielectrophoretic force is different if the electric field used is AC instead of DC and is given by [70]

$$F_{\mathrm{DEP}} = (3/2)\varepsilon_m V_p \,\mathrm{Re}\,[K(\omega)]\ \nabla(E)^2\,, \tag{31}$$

where $K(\omega)$ is the real part of what is called the Clausius-Mosotti factor and $\nabla E$ is the gradient of the electric field. The force due to DEP is oscillating in direction.

The expression for $K(\omega)$ is given by

$$K(\omega) = \mathrm{Re}\left[\frac{\varepsilon_p^* - \varepsilon_m^*}{\varepsilon_p^* + \varepsilon_m^*}\right]. \tag{32}$$

Here $\varepsilon_p$ is the particle dielectric constant, in our case that for gold, and $\varepsilon_m$ is the medium dielectric constant; and note that the dielectric constant is a complex quantity. Gold NW growth using the DEP method is predominantly in the <110> direction [67].

## V.2 Experiment

Electrode-pairs are usually fabricated using photolithography onto a chip for growing wires in circuits [66, 67]. Here we use electrodes fabricated from copper wire. Figure 46 shows the experimental setup used for growing NWs. An arbitrary waveform function generator (Wavetek 395) is used to supply an alternating voltage at a variable frequency. We used a sinusoidal waveform. The region between the electrodes is observed using an optical microscope shown in Fig. 46. To grow the NWs, 100 μL of gold NR solution was used. The weight concentration of the rods is 35.7 μg/mL, the pH was 3.1, and the morality was 874 pM. The charge on the rods is usually determined from zeta potential measurements. The zeta potential of the NRs we used is 30 mV, indicating the NRs are positively charged.

The electrodes are brought nearly into contact, without actually touching, before growing a NW. Using a translation stage shown in Fig. 46, with one electrode fixed and by moving the second electrode, a gold NW can be drawn and its size controlled well. We typically used peak voltages from 2.5 ± 1 V and frequencies from 1-10 Hz. The applied AC voltage was terminated manually when the desired wire size was obtained. As seen in Fig. 46 one electrode is grounded and the other is connected to the function generator. After the NWs are grown they are characterized using SEM and AFM. The TEM has better resolution but it is difficult to load NWs onto a TEM grid without breaking them.

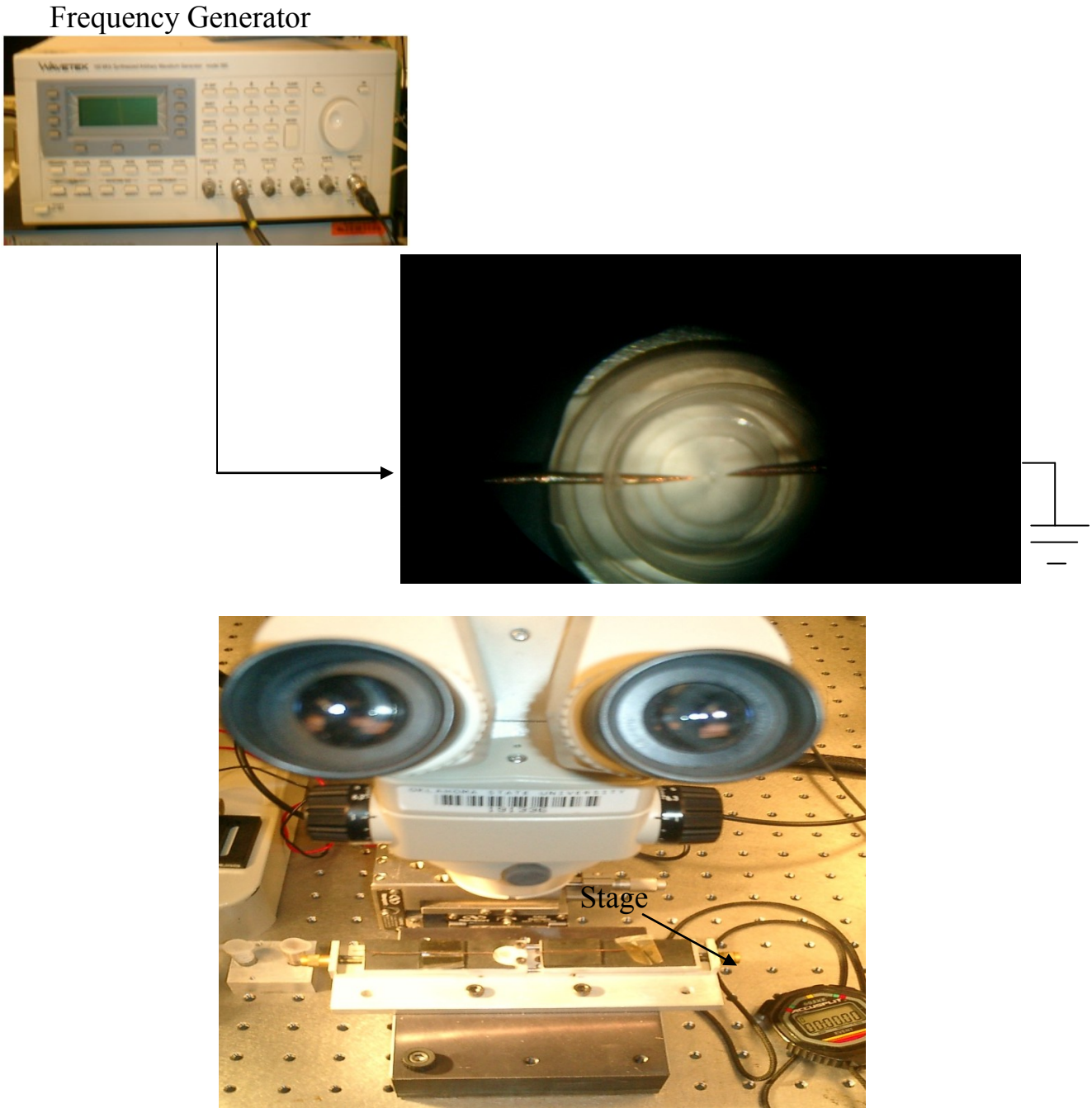


Figure 46. Block diagram of the apparatus used for nanowire assembly and a photograph of the experimental setup used in the experiment

## V.3 Results and Discussion

The chaining of nanoparticles or NRs in forming a NW depends strongly on the ability of the particle-field and particle–particle interactions to overcome Brownian motion [67]. The strength of the particle-field interaction is characterized by the unitless trapping parameter [67, 71]

$$\eta = \mu E/ (k_B T). \tag{33}$$

where $\mu$ is the magnitude of the induced dipole moment, $E$ is the applied field magnitude, $k_B$ is the Boltzmann constant ($1.381\times10^{-23}$ J/K) and $T$ is the temperature in degrees Kelvin.

Figure 47 shows an SEM image of a NW after being deposited on a fused silica microresonator. The NWs grown in our lab are long, from 200 μm to around 600 μm. This is a novel method for growing long NWs, the size of which can be controlled well. The AR of the wires grown in the lab is 600 or more. Commercially available NWs from Nanopartz have AR from 150 to 200. Growth conditions like electrode geometry and concentration of nanoparticle solution are kept identical, but voltage amplitude and frequency are varied when we grow NWs.

Figure 48(a) shows an SEM image of a fragment of the NW on the fused-silica-surface. Figure 48(b) shows a higher resolution SEM image detailing the internal structure of a different NW, showing how the gold NRs were chained well under the influence of the gradient electric field. All the SEM images are taken at 20 kV.

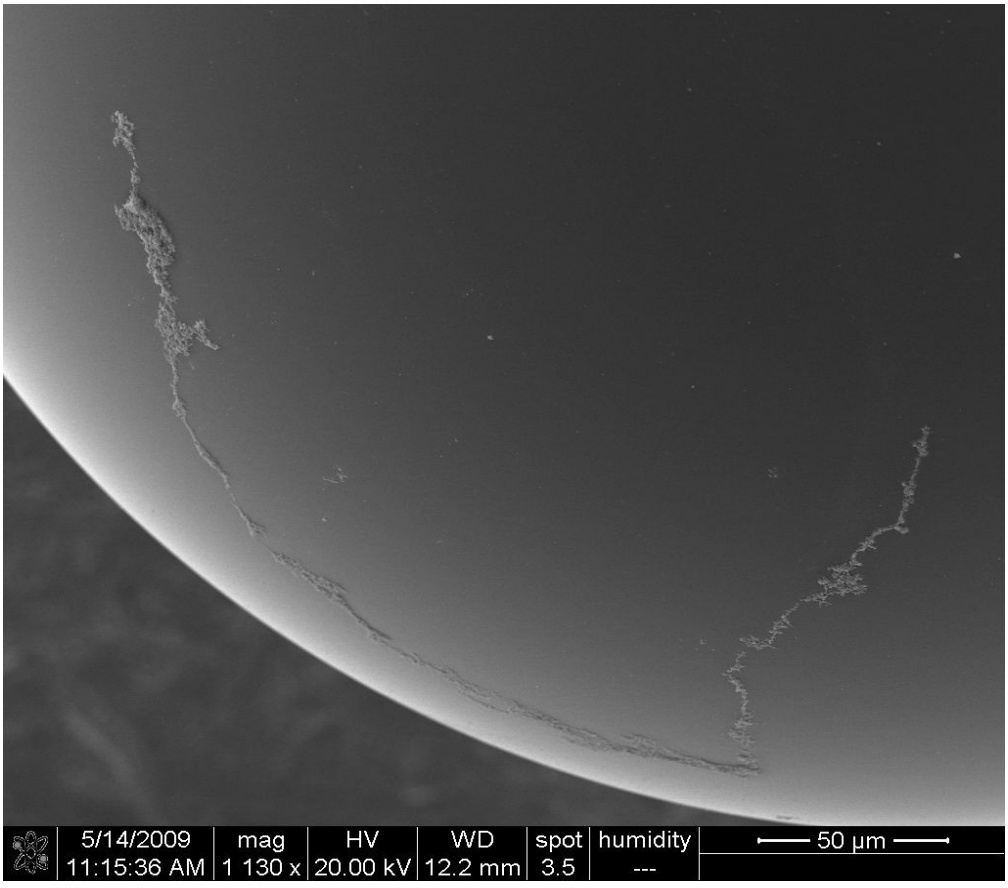


Figure 47. SEM image of a gold NW grown and then deposited on the surface of a silica microresonator.

(a)

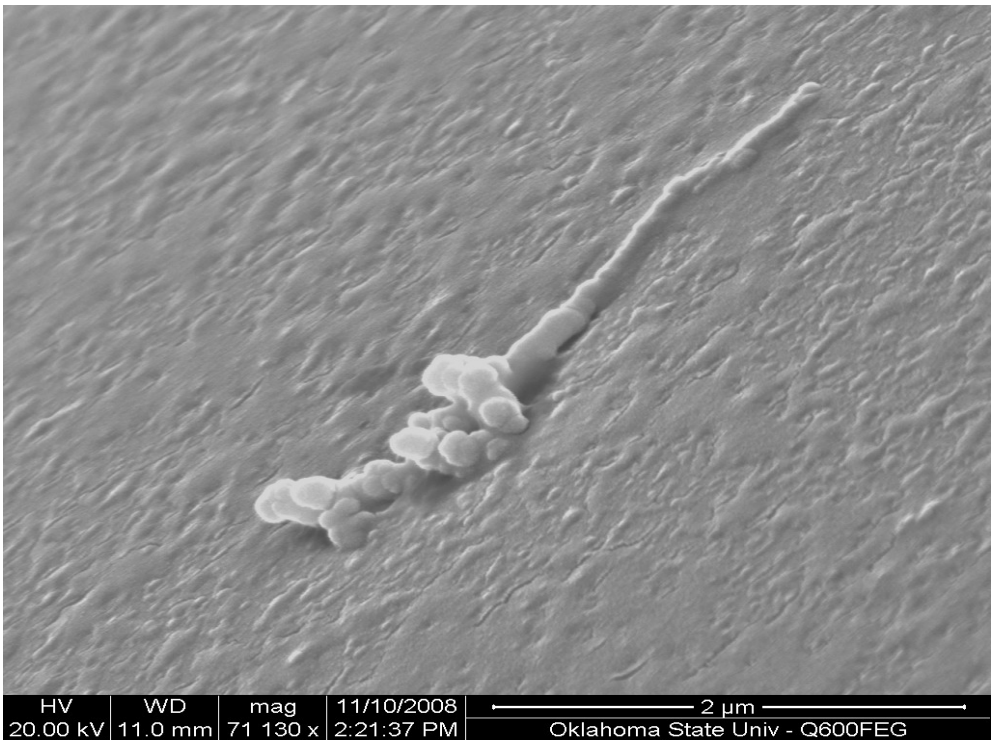


(b)

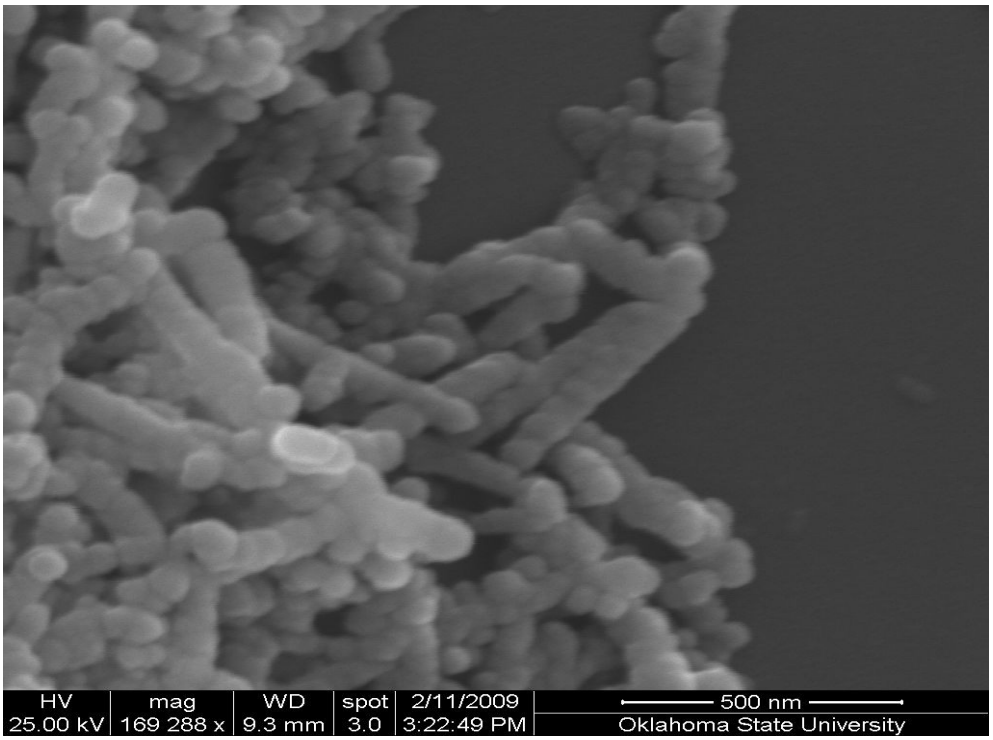


Figure 48. SEM images of two different gold NW fragments. (a) Taken at 71130 magnification, scale bar is 2 µm. (b) Taken at 169238 magnification, scale bar is 500 nm.

The general trends for modifying NW growth by changing the various parameters are noted here. The most important parameters affecting growth are the field strength and NR concentration; they should exceed certain limits or thresholds in order to start seeing NW growth. As we increase the particle concentration the growth rate and thickness of the wire increase [70]. As we increase the peak AC voltage from 0-3 ± 2 V, the growth rate and thickness of the wire increase and branching reduces. We used 4 V peak and 1 Hz to grow the wire shown in Fig. 49 (a). If we switch over from AC voltage to DC voltage we have observed branching under nearly identical conditions as seen from Fig. 49 (b). We can reduce the branching by increasing the particle size under identical growth conditions [70]. As the particle concentration increases beyond 0.13% the growth rate and thickness of the NW can be increased [70].

The novelty in our technique is that we can grow wires without having to amplify the voltage to 30 V or greater as has been reported [67, 70]. The frequency we used is also relatively low, 1-10 Hz, compared to 100-150 Hz or even a few MHz used by other groups [67]. As we draw the wire the thickness of the wire reduces, perhaps due to the decrease in the influence of the electric field on the particles. The influence of electrode separation on growth characteristics of the NW still needs to be further investigated; no results were found in the literature.

The conductive properties and other characteristics of the high-AR wire still need to be investigated before it can be used in circuits. Our objective was to grow a high-AR wire and deposit the fragments on the microresonator, to observe SPR effects and use it for many applications. The applications of NW fragments coated on the microresonator will be discussed briefly in the next section.

(a)

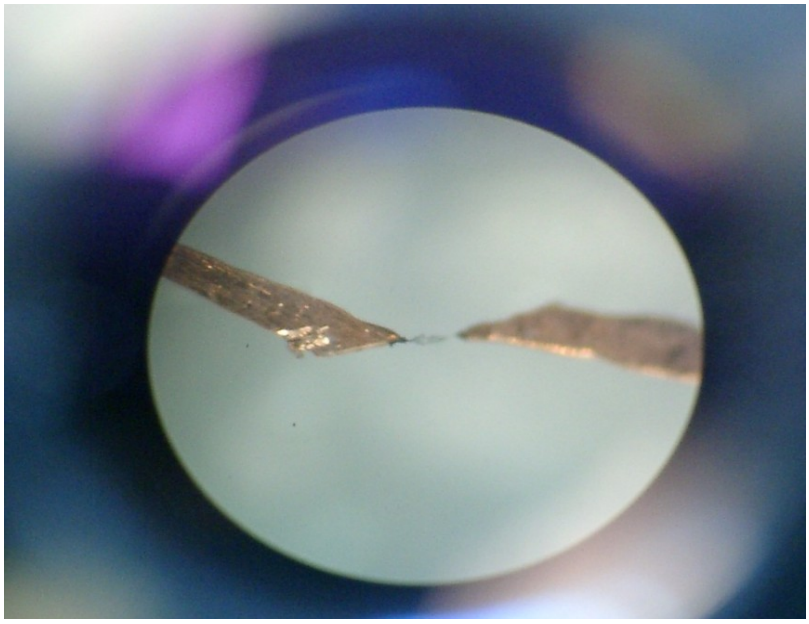

(b)

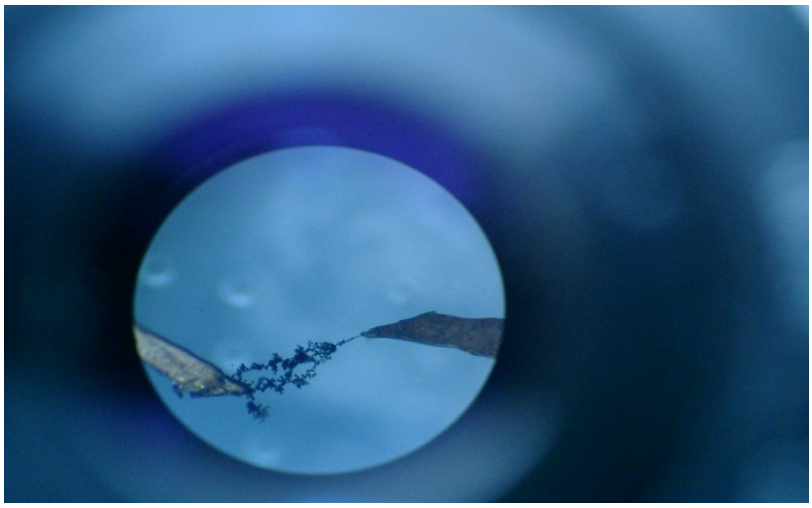

Figure 49. NW assembly at (a) 4 V (peak) AC and 1Hz setting; (b) 3 V DC setting.

## V.4 Conclusions

Nanowire growth between targeted points, copper electrodes in our case, is obtained by using the DEP method. An alternating voltage is applied to the electrodes immersed in a gold growth solution containing low-AR gold NRs. By controlling various growth parameters as discussed in the chapter we can grow needle-shaped or dendritic NWs.

Proper choice of the parameters enables the suppressing of side branching when a NW is grown. The tip of the electrode should also be sharp to suppress side branching and also to produce strong electric fields. This is a novel method of growing high-AR (20-600) gold NWs from low-AR NRs. We have better control over the size of the NW and growth of the NW can be stopped once we obtain the size we need. This wire growth method can be applied to various other metals, alloys and pure semiconducting compounds.

A possible future direction would be to study the electrical and optical properties of these wires in detail. Improving the existing method could improve the growth of gold NWs with a thinner diameter (a few nm), produced today only by wet chemical synthesis methods.

# Chapter VI

# ADHESION METHODS FOR NANOMATERIALS ON MICRORESONATOR

## VI.1 Introduction

Growth of nanostructures has been studied in detail in the two previous chapters. To be useful to us, these nanostructures must be adhered to the surface of a microresonator. Single-walled carbon nanotube segments have been deposited on nanolithographic templates [72]. Silver NWs have been grown on a surface of a $CaF_2$ crystal [73]. Gold NWs can also be grown directly on the Si surface by surfactant-assisted galvanic reduction [74].

Little research has been devoted to adhesion of the gold NRs grown by wet chemical synthesis on different substrates. The adhesion of gold nanostructures on different substrates has been a challenging task. This requires us to know the surface charges of and chemical reactions between various combinations of nanostructures, polymer coating layers, and substrates (whose surfaces may be functionalized). In order to put the interesting electrical and optical properties of these nanostructures studied by various groups [52, 67] into use, we need to know the chemistry in detail. In this chapter the surface chemistry of various polymers, chemicals and fused-silica substrates is studied.

Gold NRs can be grown directly on a silica surface by modifying the surface [75]. This method lacks control of the AR or of the surface distribution of the gold NRs

obtained, making them less useful for applications we want, like sensing and to study the SPR and SERS (surface enhanced Raman scattering) effects. The surface of the fused silica microresonator can also be modified to accommodate wet chemically grown gold NRs on the surface. Silanes like 3-mercaptopropylmethyldimethoxysilane (MPMDMS), have been used to modify the surface. Also other polymers (or combinations of them) such as poly (acrylic acid) (PAA), PDDA, and poly (4-styrenesulphonic acid) (PSS), and single-walled CNT (carbon nanotubes) have been used to modify the surface of a fused silica microresonator. These modified surfaces can improve the adhesion of gold NRs on them.

After summarizing surface charge properties in section VI.2, experiments and results involving surface-modified fused-silica microresonators will be discussed in section VI.3. AFM was used to study a surface of a Si surface modified with MPMDMS [76]. We use SEM for characterizing the modified surfaces. The AFM technique is good if the substrate is flat; we faced problems in resolution and obtained artifacts using AFM, since our surface is curved. TEM is not possible as it is difficult to load the sample onto the TEM grid for imaging. Some applications involving these coated microresonators, with preliminary results, will be discussed briefly in section VI.4.

## VI.2 Surface Charge Distribution

The surface charge is important in the adhesion process. Initially we had difficulty in adhesion of gold NRs on the fused silica microresonator. This was because the fused-silica microresonator has a weak positive charge and the gold NRs are positively charged since they are capped with CTAB. The literature shows that gold NRs have a positive zeta potential of +30 mV [77], therefore causing repulsion between the

fused-silica surface and the NRs. A water layer present on top of a microresonator makes it weakly negatively charged. It can then be coated with PDDA in water, which will make the PDDA-coated microresonator strongly positively charged; uncapped gold seeds, unlike NRs, are negatively charged, and so they can be attached to the microresonator.

The structures of a few of the polymers used for adhesion in this chapter are given in Fig. 50, and a summary of net charges is given in Table 5.

(a) (b) (c)

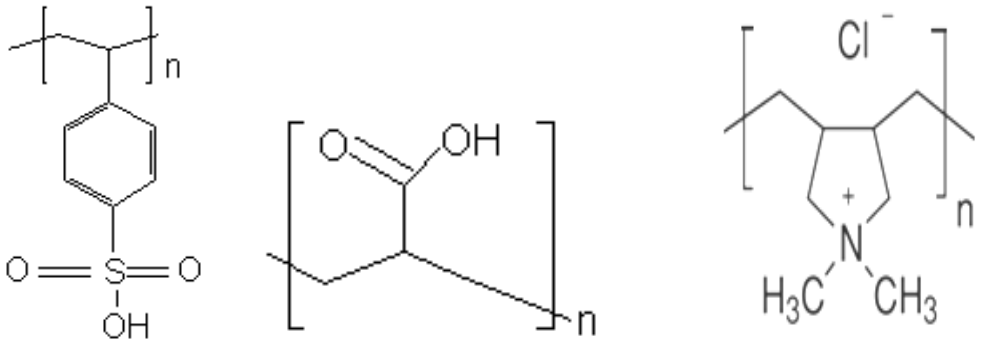


(d)

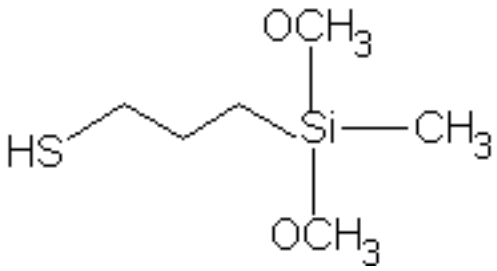


Figure 50. Chemical structures of (a) PSS, (b) PDDA, (c) PAA, (d) MPMDMS.

| Chemical | Net Charge |
|---|---|
| Gold NRs and seeds | -ve |
| Gold NRs CTAB Capped | +ve |
| CTAB | +ve |
| PSS | -ve |
| PAA | -ve [77] |
| PDDA | +ve |
| Silica surface silanized with MPMDMS | - ve |

Table 5. Net charge of various chemicals or polymers used for coating or deposition.

Some of the net charges mentioned in Table 5 have been verified experimentally. Knowing the charge of gold NRs, if the fused silica microresonator is coated with PDDA and dipped in a gold NR solution, subsequent SEM images show no adhesion, due to repulsion of identical charges. The same experiment was repeated for gold seed solution and we could see from electron microscopy images the adhesion of seeds on the microresonator. PSS and PAA, like PDDA, are called polyelectrolytes; these polymers partially dissociate in aqueous solution, making them negatively charged [77]. The experiments performed and steps involved in the process of modifying the surface of a fused-silica microresonator are discussed in the next section in detail.

## VI.3 Experiment and Results

Two methods for surface preparation of fused-silica microresonators for adhesion of gold NRs are primarily discussed in this section. Methods for coating microresonators with gold NWs and CNTs will be discussed briefly. The silanization of a Si wafer with MPMDMS is discussed in [76]. The additional chemicals and their suppliers required for experiments not discussed in previous sections are MPMDMS (>99%), PAA ($M_w$ = 450,000), and PSS ($M_w$ = 75,000, 18 wt. % in $H_2O$) are purchased from Sigma Aldrich; ethyl alcohol (200 proof) is purchased from Chemistry store at Oklahoma State University; the CNTs are obtained from the group of Dr. J. Wicksted.

The surface preparation for silanization with MPMDMS involves first cleaning the fused-silica microsphere with ethanol as soon as it is prepared. Figure 51 illustrates the steps involved in this procedure. After the sample is cleaned it is dipped in a 1:20 solution of MPMDMS in ethanol for >10 hrs. (Immersion in MPMDMS for 4-5 hrs did not make it strongly negatively charged enough to adhere the rods, and SEM imaging did

not show any rods present). Then the sample is taken, out rinsed in ethanol, and dried in nitrogen for 1-3 minutes. In the last step the microresonator is dipped in a high-AR gold NR solution for 5 seconds to 50 minutes, depending on the concentration of NRs required on the surface.

Figure 52 shows a SEM image of a bare fused silica microresonator after being dipped in ethanol, before surface modification. This image was taken at a higher magnification to show that the surface is clean. Figure 53 (a) and (b) show SEM images of high aspect ratio gold NRs prepared in-house coated onto the fused silica microresonator, taken at different magnifications.

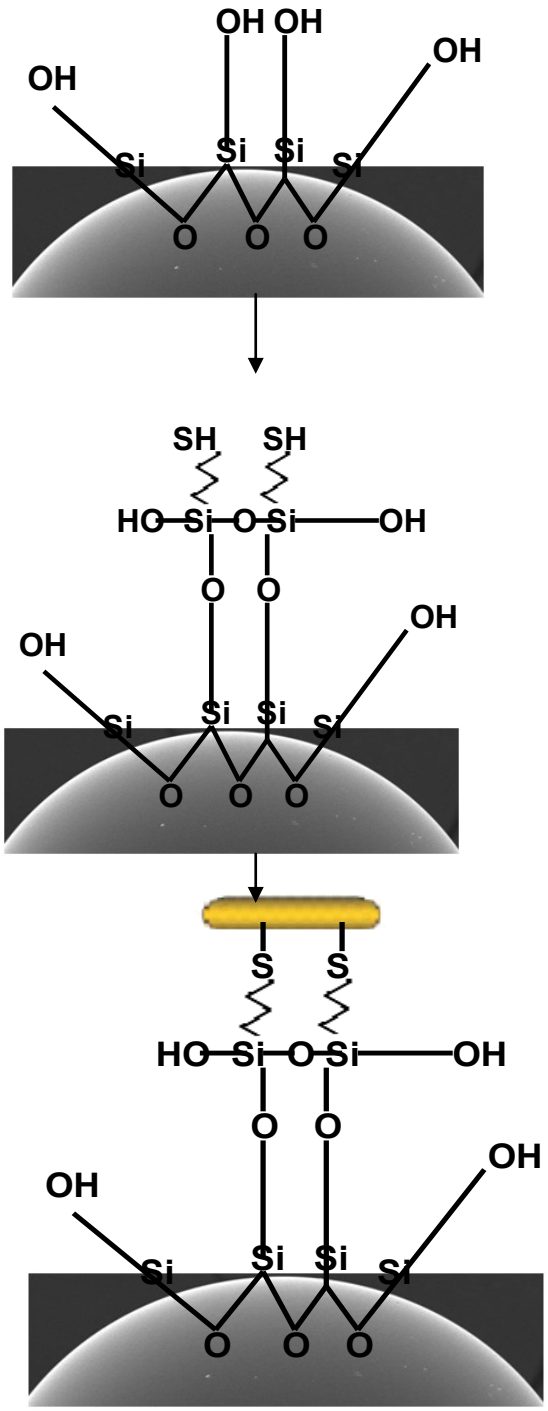


Figure 51. Schematic representation of the microresonator silanization process with MPMDMS and coating with gold NRs. Top to bottom: bare sphere, silanized sphere, and NR attachment.

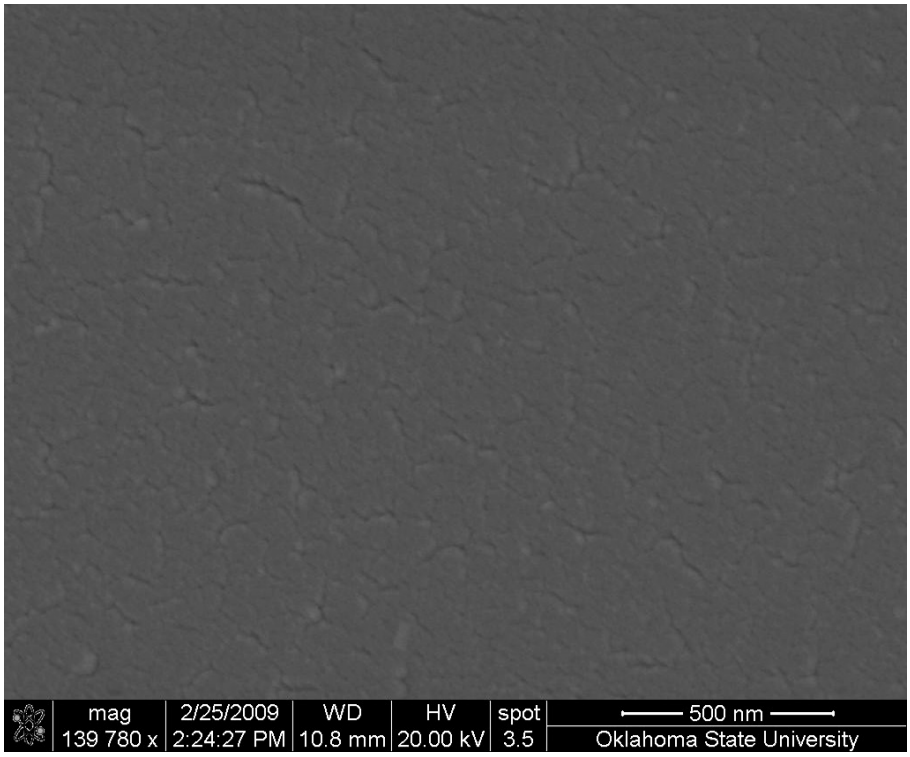


Figure 52. SEM image of bare fused silica microresonator before surface treatment. Taken at 139780 magnification, scale bar is 500 nm.

(a)

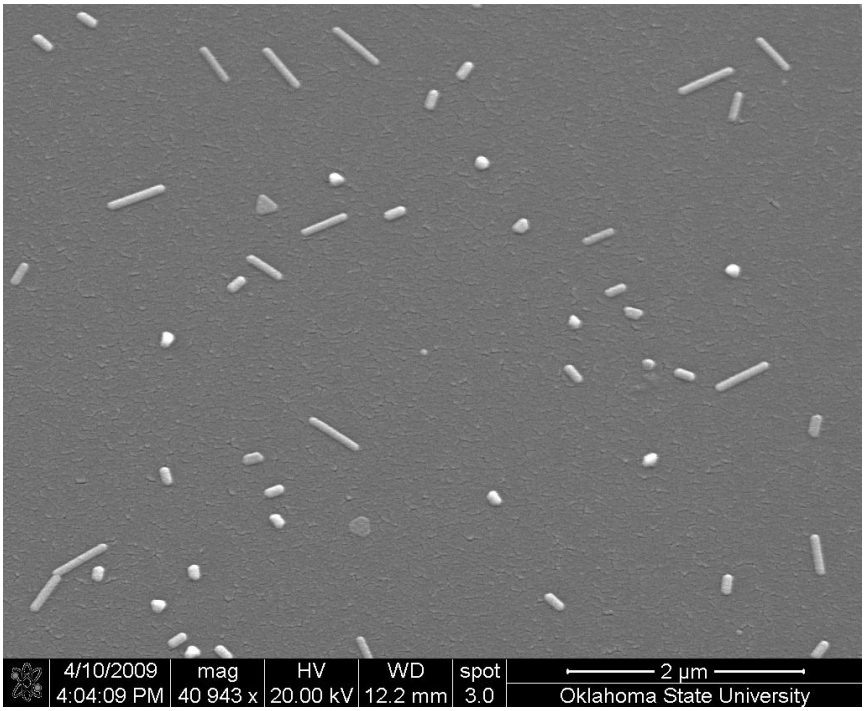


(b)

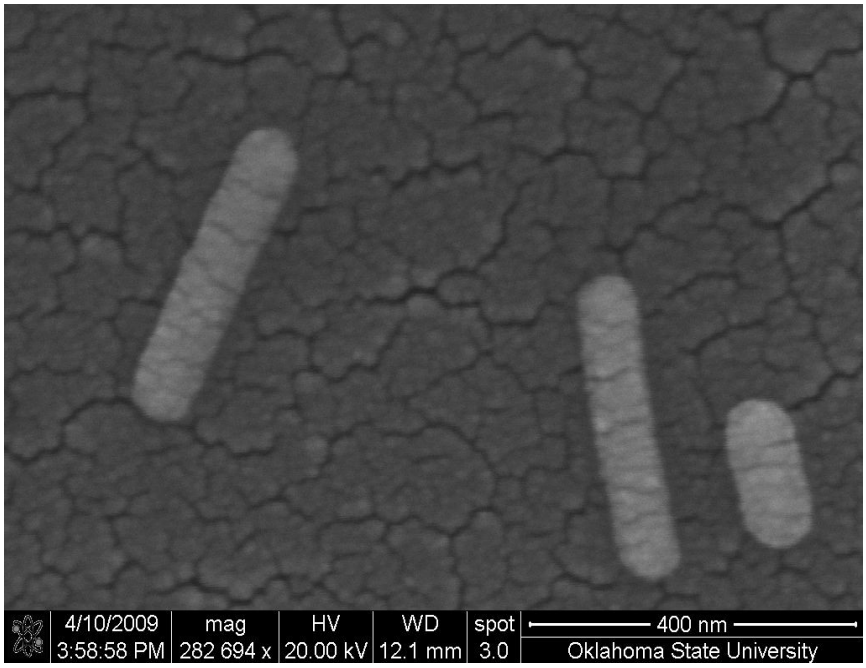


Figure 53. SEM images of high-AR gold NRs on silanized fused silica microresonator. (a) Taken at 40943 magnification, scale bar is 2 µm. (b) Taken at 282694 magnification, scale bar is 400 nm.

The second method of modifying the microresonator surface involves using PAA and PDDA. Here we used the LBL (layer-by-layer) approach discussed in the literature [37]. We used the method discussed in [77] to make gold NRs negatively charged using PAA. Take 1000 μL of PAA solution in water and add 1 mL of the purified high-AR gold NRs solution while stirring it vigorously. The NRs end up with a net negative charge provided by excess COOH groups formed from electrostatic attraction between PAA and the gold NRs, and this has been by zeta potential measurements [77]. The microresonator is first coated with PDDA in DI water (1:20), followed by rinsing in DI water to remove any unbonded PDDA, forming a thin film of PDDA. Next the microresonator is dipped in the negatively charged gold NR solution for 10-15 minutes and this is followed by rinsing in DI water.

Figure 54 shows an SEM image of the fused silica microresonator coated with gold NRs. This method did not provide uniform coating all over the surface of the microresonator, unlike the first method discussed above. Other drawbacks to this method are low reproducibility and aggregation (as seen from Fig. 54). We cannot use this method for any applications related to coated microresonator as it would lower the $Q$ of the microresonator and this was observed experimentally from the whispering gallery modes. Better purification methods and slight modification in the method might make this method better for various applications.

We also attempted to adhere gold NRs onto the microresonator using PSS/PDDA combination. First we dipped the microresonator in PDDA, then in PSS, followed by dipping in gold NR solution. The surface showed no NR attachment, only aggregation of

PSS on the surface. Another method was also tried, to mix PDDA and low-AR gold NRs and stir the mixture before applying the layer by dipping the microsphere in it. This attempt showed sporadic adhesion only at few places on the microsphere. Figure 55 shows an island of unbonded PDDA covering the NRs.

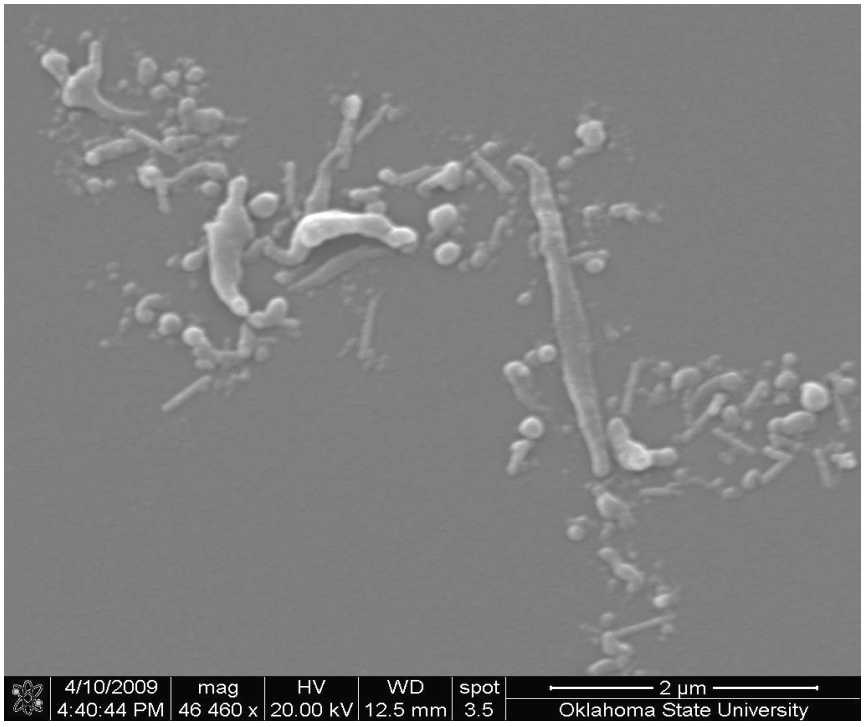


Figure 54. SEM image of (PAA-coated) high-AR gold NRs on PDDA-coated fused-silica microresonator. Taken at 46460 magnification, scale bar is 2 µm.

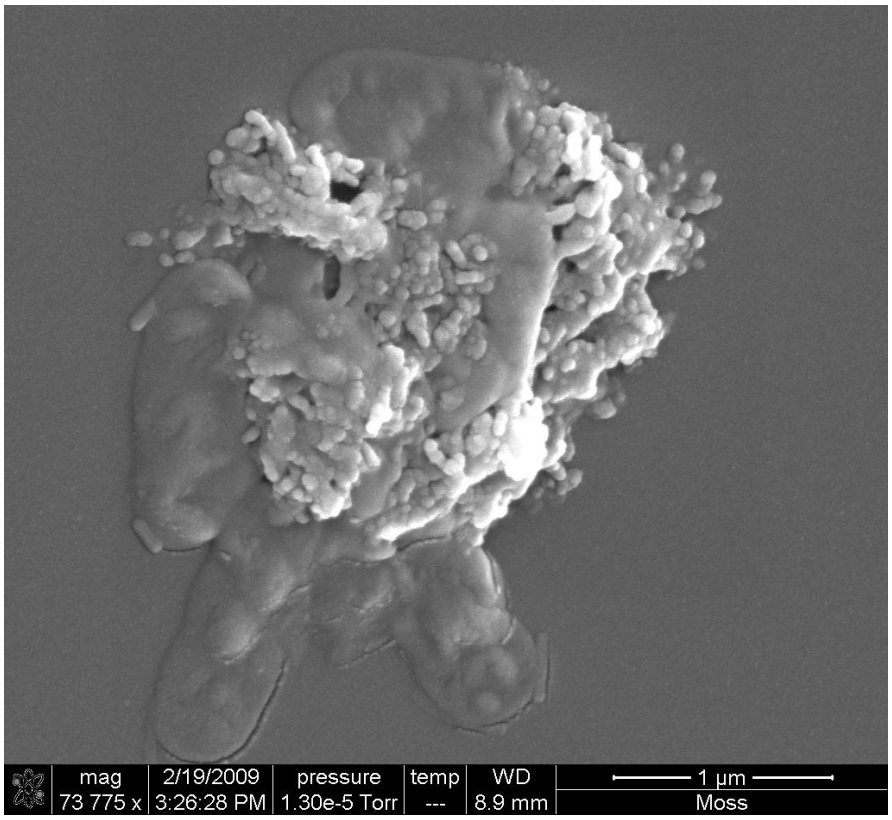


Figure 55. SEM image of low-AR gold NRs mixed into PDDA and coated onto a fused silica microresonator. Taken at 73775 magnification, scale bar is 1 µm.

Gold NWs grown by the DEP method were coated on the microsphere. After the NW was grown between the electrodes, a high precision 3D stage was used to position the microsphere under the NW as seen in Fig. 56. The microsphere was then gently moved up through the electrode gap, breaking free the NW from the electrodes and positioning it on the surface of the microsphere. The composition of the NW deposited on the surface of the microsphere coated as shown in Fig. 57 consists primarily of NW segments of varying density, along with unchained gold NRs and gold seeds. The AR of the individual NW segments is at least 10. Better filtration methods could be used to remove the seeds and other structures from the solution after the gold NW is grown.

An attempt was also made to deposit a gold NW grown by authors in [67] on a cylindrical fiber. Figure 58 represents a cylindrical fiber, onto which a gold NW has been deposited. The images are taken using an optical microscope (Leica). Similarly NWs can be deposited on any structure that is small enough. The NW-deposited microresonator can be used for many potential applications like sensing and SPR effects, well within the telecommunication frequency band.

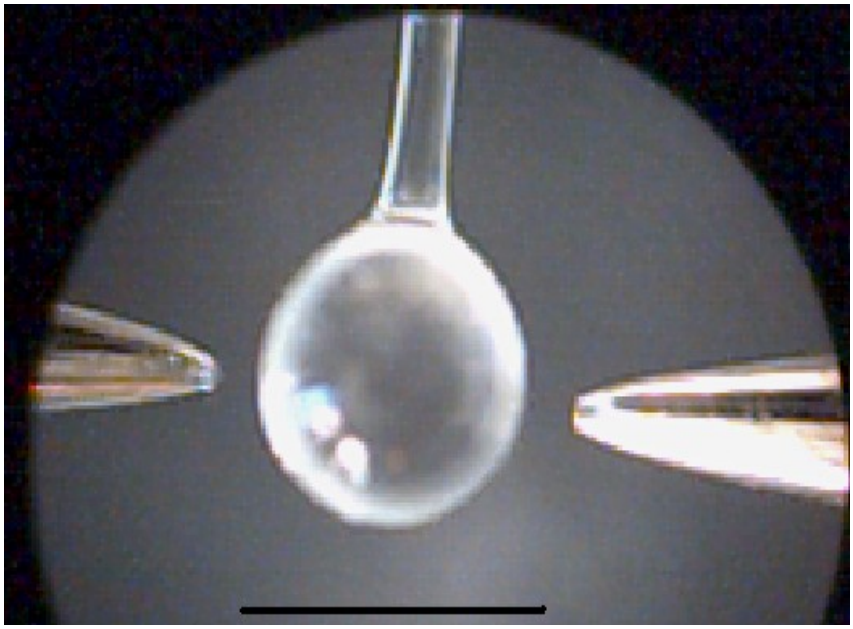

Figure 56. A bright field image of a microresonator positioned between the DEP electrodes, scale bar is 1mm.

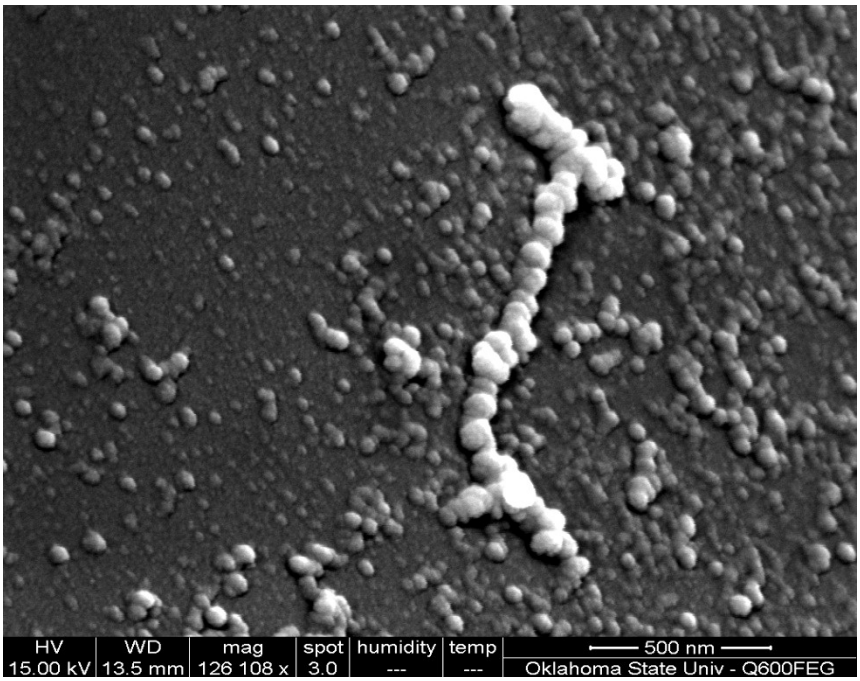


Figure 57. SEM image of a fragment of NW segment after breaking away from the electrodes and wrapping around the circumference of the microsphere.

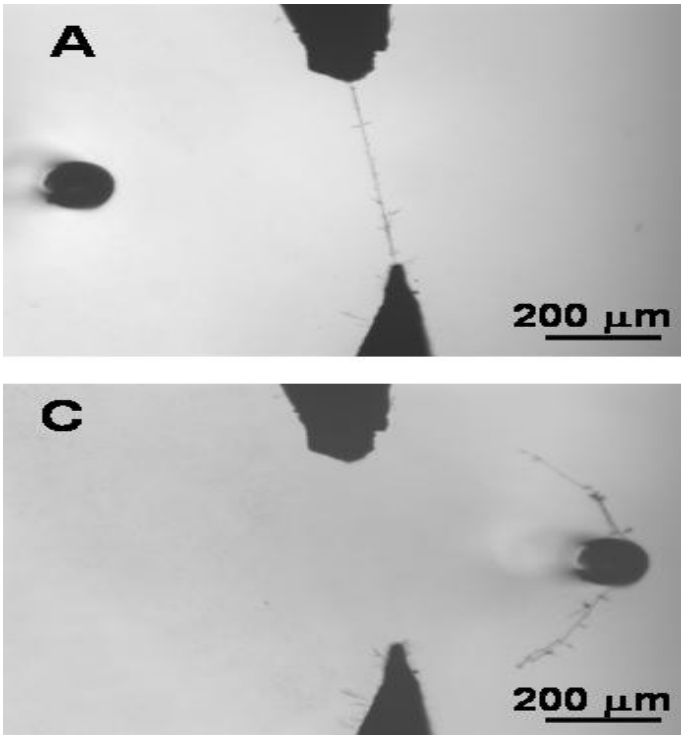


Figure 58. (A) A bright field image of a NW grown between the electrode gap, to the left of which is a cylindrical fiber approaching the electrode gap. (C) The NW breaking away from the electrodes and wrapping halfway around the circumference of the fiber.

Much research has been done to study the novel properties of CNTs, which makes them useful in many applications in nanotechnology, electronics, light-emitting diodes, solar cells, optics and many fields of materials science [78-80]. They exhibit either metallic or semiconductor properties. A CNT can be either a single–wall nanotube (single graphene sheet) or a multi-wall nanotube (several nested cylinders of graphene sheets). A CNT is a hundred times as strong as steel, light, chemically inert, and can be as long as 2 mm [81]. The CNTs are usually functionalized for adhesion of various nanoparticles, without degrading the mechanical and electronic performance of the CNT [81].

The adhesion methods of CNTs on the fused-silica microsphere are discussed in this section. Functionalized CNTs of negative charge are obtained from the group of Dr. J. Wicksted at Oklahoma State University. The microsphere is first coated with PDDA to make its net charge positive. Next the microsphere is dipped in a CNT solution for 5-10 minutes depending on the concentration required on the surface. Then the surface is dipped in DI water to remove any unbonded particles. In the last step, it is dipped in a solution of low-AR gold NRs grown in-house. The same procedure was also repeated on a glass slide coated with CNTs. Figure 59 (a) and (b) show SEM images of CNTs on the microresonator and glass slide. We could not resolve individual NRs since they are covered by thick strands of CNTs. This experiment was performed as proof of concept and requires much more refinement in procedure and filtration of CNTs before the coated microresonator can be used for potential applications.

(a)

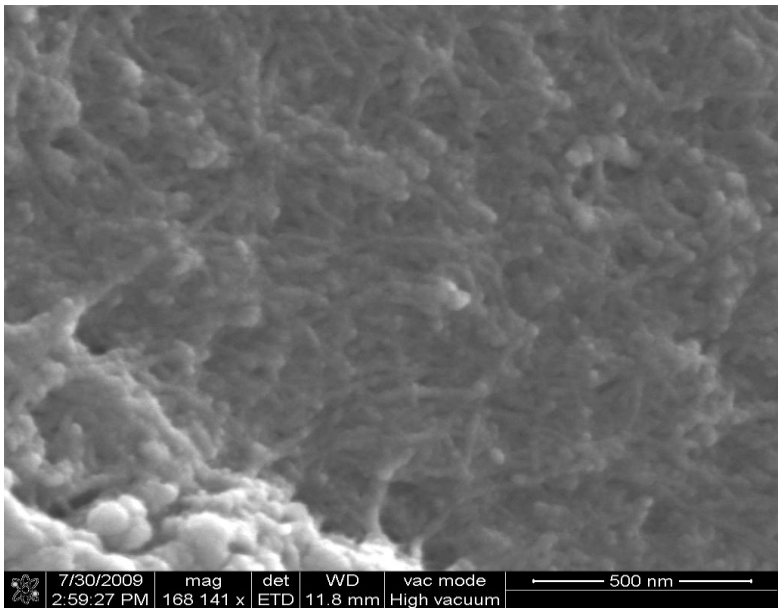


(b)

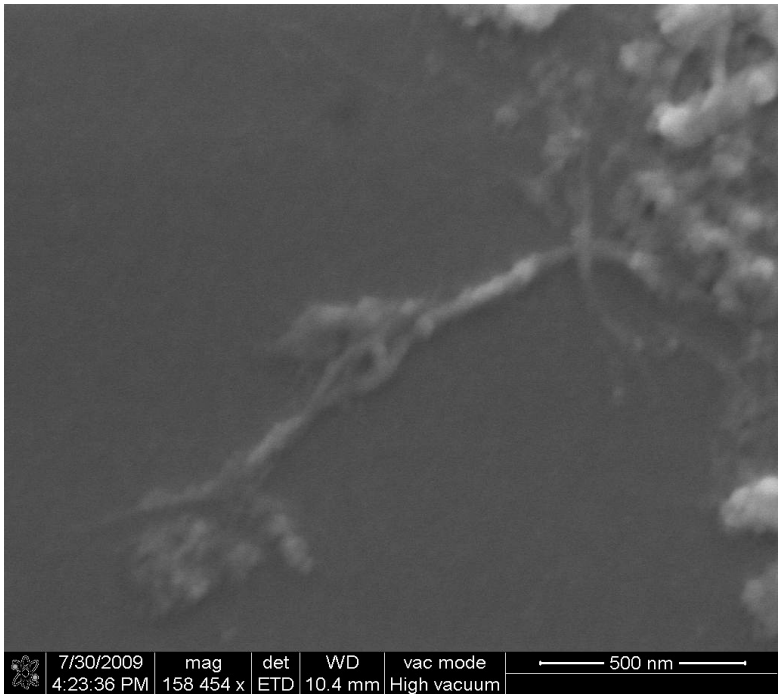


Figure 59. SEM images of CNT coated, (a) fused-silica microresonator, (b) glass slide. The scale bar is 500 nm.

## VI.4 Applications

In this section, a few applications and preliminary results for microresonators coated with gold NRs and gold NWs are discussed briefly. The results are discussed in more detail in [82]. The evanescent fields of whispering-gallery modes of a high-$Q$ dielectric microresonator are locally enhanced via excitation of the surface plasmon resonances of gold NRs on the microresonator's surface. This results in enhanced coupling between the microresonator and an adjacent tapered optical fiber for frequencies in the vicinity of the SPR.

Experimentally determining the WGM quality factor $Q$ and the loss ratio $x$ before (single prime) and after (double prime) Au NR growth is sufficient to determine the coupling enhancement factor, given by [83]

$$F_c = \frac{Q_c'}{Q_c''} = \frac{Q'\left(1+\frac{1}{x'}\right)}{Q''\left(1+\frac{1}{x''}\right)}, \tag{34}$$

and the intrinsic loss enhancement factor given by

$$F_i = \frac{Q_i'}{Q_i''} = \frac{Q'(1+x')}{Q''(1+x'')}. \tag{35}$$

The experimental results discussed and presented in [83] for surface-grown low – ARs at 800 nm demonstrate coupling enhancement by a factor of 100–1000, accompanied by an increase in absorption and scattering loss that is very small by comparison. We have performed similar experiments, at 1550 nm with our high-AR rods grown in solution and coated on a silanized surface. We have observed coupling

enhancement by a factor of 1–1500, accompanied by an increase in absorption and scattering loss by a factor of 1-1500. The same experiments repeated using an 800-nm laser and solution-grown low-AR gold NRs demonstrate coupling enhancement by a factor of 1-400.

Similar experiments with NW fragments deposited on the surface of the microsphere demonstrate coupling enhancements of a factor of 60–600, which are accompanied by an increase in absorption and scattering loss, depending on where the microresonator is probed spatially. These gold-NW coated microresonators could provide enhanced sensitivity in various types of gas, chemical, and biological surface-plasmon-based sensing applications well within the telecommunication frequency band.

We have also demonstrated that this enhancement can be controlled by an external beam leading to what is called plasmonic switching [82]. Sensing of SDA2072 (HW Sands Corp.) dye was also seen by us using a microresonator coated with gold NRs and the experimental results are explained in more detail in [82]. The solvent used in this case is methanol. The SDA dye is chosen since it has significant absorption at 1550 nm. We have tested for a Raman scattering signal using both bare and silanized NR-coated microspheres, by dipping in the Raman active liquids like ethanol, pyridine and carbon tertrachloride. The result of the SERS studies, done at 800 nm pump wavelength, is discussed in detail in [82].

## VI.5 Conclusions

The ability to deposit gold NRs and NWs on various substrates is important to develop applications based on these nanostructures. The surface chemistry of various polymers was studied before adhesion methods were tried for fused-silica microresonators. Various methods for coating the fused-silica microresonator with seed - mediated solution-grown gold NRs were discussed in this Chapter. The most successful method involves silanization of the surface of the microsphere with MPMDMS and coating with gold NRs. We have also used PDDA/PSS combination, and using LBL technique coated the surface of a fused-silica microsphere with gold NRs. Characterization of the samples with the SEM indicated deposition. We have also coated NWs on the surfaces of fused silica-microresonators and cylindrical fibers, by careful alignment and positioning of the surface before pulling it through the NW.

We have also attempted to coat the microspheres with CNTs and characterized these with the SEM. WGMs in these microresonators, which by themselves have interesting optical properties discussed in previous sections, would excite SPRs of gold NRs on the microresonator surface. This enhances coupling to the microsphere when an adjacent tapered optical fiber is brought in contact. These coating methods can make the microresonators useful for plasmonic sensing applications and for surface-enhanced Raman scattering (SERS) studies. These devices can also be used for plasmonic switching applications with the aid of an external laser beam.

# Chapter VII

# CONCLUSIONS AND FUTURE DIRECTIONS

The series of projects discussed in this dissertation represent areas of research relating to practical applications of microresonators, systematic study of assembly and characterization of nanostructures, and adhesion methods of the assembled nanostructures on the microresonators. In this Chapter the results of previous chapters are summarized briefly, the significance and possible applications of our results are evaluated, and further investigations related to those areas are discussed.

In Chapters II-III a tunable diode laser operating near 1570 nm is used to investigate various effects of the heat transfer from fused-silica microspheres, with and without thin-film coatings, to the surrounding gas in a vacuum chamber. A novel method is employed in Chapter II for measuring thermal accommodation coefficients of various gases like nitrogen, helium and ambient air on several coated and uncoated surfaces of fused-silica microresonator, operating at room temperature. This work can be extended to various other gases, using different surface coatings (thin compared to the wavelength); a large number of gas-surface interactions can be studied. The precision of these measurements is quite good (< 2%). In Chapter III, this method is further extended to measure the absorption coefficient of a surface film or water layer on a fused-silica microresonator. The strength of the observed thermal bistability gives us the heat supplied by the fraction of total optical power lost due to absorption. The results provide insight into the relative importance of surface scattering and absorption in these

structures. This absorption results from a water layer on the surface of a bare sphere, and for a coated sphere it is due to the thin film. This provides a novel method to find the water layer desorption and adsorption rates on the surface of a microresonator in the presence of gases like ambient air and nitrogen. In the future this method can be used to study a wide variety of thin films, with arbitrary refractive index and possibly thickness. This method can be extended to study the water desorption rate in the presence of other gases. This method can be used for sensing applications, surface chemistry studies and to know the contaminants present on the surface.

In Chapter IV, we have found methods to grow gold NRs of different AR in solution by wet chemical synthesis methods and also by directly growing them on the surface of the fused-silica microresonator. Better filtration and purification methods were employed to improve the yield of gold NRs. We also explored different microscopy methods like TEM, AFM and SEM to characterize the gold NRs at different magnifications. Better methods were found to control the AR of gold NRs and we could grow gold NRs with AR as low as 2.5 to AR as high as 18.0. Future work would be to improve the yield for higher-AR gold NRs of any size and to find better methods for absorption measurements in the case of high-AR gold NRs. These methods will let other research groups explore optical, catalytic and mechanical properties of gold NRs. These gold NRs of different sizes have potential applications in SERS studies, to identify biological specimens, and to provide enhanced sensitivity in various types of gas, chemical and biological surface-plasmon-based sensing applications well within the telecommunication frequency band. Gold NRs can also be used for making gold nanowires for interconnects in electronic circuits. NRs with unique optical properties are

generating much enthusiasm in molecular biology and medicine, with potential applications in the detection of cancer. By controlling the shape and size of NRs, their longitudinal SPRs can be tuned into the NIR region allowing better imaging techniques for the treatment of cancer. In addition, strongly absorbed light is converted into localized heat by gold nanoparticles for destroying cancer tumor cells.

In Chapter V, a NW is grown between targeted points, that is, copper electrodes using alternating voltages by using the DEP method, referred to as directed electrochemical NW assembly. Better purification methods are discovered to remove excess CTAB, which disrupt the unidirectional growth of gold NWs. By controlling various growth parameters discussed in the chapter we can grow needle shaped or dendritic NWs. Proper choice of the parameters enables the suppression of side branching when a NW is grown. This is a novel method of growing high-AR (20-400) gold NWs from low-AR gold NRs. We have better control of the size of the NW and growth of the NW can be stopped once we obtain the size we need. This wire growth method can also be applied to various other metals, alloys and pure semiconducting compounds.

A future direction would be to study the electrical and optical properties of these wires in detail. One could also study the effect different gold NR ARs would have on the growth of gold NWs. Improving the existing method could permit the growth of gold NWs with a thinner diameter (a few nm), produced today only by wet chemical synthesis methods. NWs of variable length can be grown, using this technique, across targeted points in the circuits of microelectronic devices. The miniscule size of the NW can

improve the speed of computers as we can accommodate a larger number of transistors. The most likely application in our lab would be for trace-gas sensing.

The ability to deposit the gold NRs and NWs on various substrates is important to develop applications based on these nanostructures. In Chapter VI, the surface chemistry of various polymers was studied before adhesion methods were tried for fused-silica microresonators. Various methods were discovered to coat these nanomaterials on the fused-silica surface. The most successful method involves surface modification with MPMDMS before coating with gold NRs. We have also used a PDDA/PSS combination and using the LBL technique coated the surface of a fused-silica microsphere with gold NRs. Characterization of the samples with SEM indicated deposition. We have also coated NWs on the surface of fused silica-microresonator and cylindrical fiber, by careful alignment and positioning of the surface around the NW.

We have also attempted to coat the microspheres with CNTs and characterized them with the SEM. WGMs in these microresonators, which by themselves have interesting optical properties discussed in previous sections, would excite SPRs of gold NRs on the microresonator surface. This enhances coupling to the microsphere when an adjacent tapered optical fiber is brought in contact. Initial work relating to coupling enhancement at different pump wavelengths was done as proof of concept using microresonators coated with gold NRs and NWs, and we observed coupling enhancements factors up to 1500.

Future directions for this work would be to improve the adhesion methods in order to obtain a uniform coating all over the surface of the microresonator. Newer methods needed to be explored which retain the high optical quality, in order to have

potential applications for chemical sensing. The CNT solution needs to be purified to separate CNTs from other structures, which will make adhesion of gold NRs on single walled CNTs easier and more identifiable by microscopy techniques. By studying the surface charge properties we can use these techniques to grow nanomaterials on different substrates. Single walled CNT are characterized using Raman spectroscopy and gold NRs can enhance Raman scattering signals. These coating methods can make the microresonators useful for plasmonic sensing applications, trace-gas detection, and surface-enhanced Raman scattering (SERS) studies. These devices can also be used for plasmonic switching applications with the aid of an external laser beam. The development of better coating techniques that restrict NWs to the equator of the microresonator will simplify the operation of microlasers in our lab: if only the equatorial region of a microspherical laser contains the active medium, pumping can be done more easily. Likewise, this selective coating technique on the microresonator might simplify the use of surface-enhanced Raman sensing.

BIBLIOGRAPHY

1. J. W. Strutt (Lord Rayleigh), *The Theory of Sound*, (Dover, New York, 1945). Chap. I, pp. 1-20.

2. Lord Rayleigh, "Further Applications of Bessel Functions of High Order to the Whispering Gallery and Allied Problems," Phil. Mag. **27**, 100-109 (1914).

3. R. D. Richtmyer, "Dielectric Resonators," J. Appl. Phys. **10**, 391–398 (1939).

4. M. A. Popovíc, T. Barwicz, M. R. Watts, P. T. Rakich, L.Socci, E. P. Ippen, F. X. Kärtner, and H. I. Smith, "Multistage high-order microring-resonator add-drop filters," Opt. Lett. **31**, 2571–2573 (2006).

5. P. E. Barclay, K. Srinivasan, O. Painter, B. Lev, and H.Mabuchi, "Integration of fiber coupled high-$Q$ $SiN_x$ microdisks with atom chips," Appl. Phys. Lett. **89**, 131108 (2006).

6. D. K. Armani, T. Kippenberg, S. M. Spillane, and K. J. Vahala, "Ultra-high-$Q$ toroid microcavity on a chip," Nature **421**, 925–929 (2003).

7. T. J. A. Kippenberg, *Nonlinear Optics in Ultra-high-Q Whispering –Gallery Optical Microcavities,* PhD Diss., Physics Dept., California Insitiute of Technology (2004).

8. H. T. Lee and A. W. Poon, "Fano resonances in prism-coupled square micropillars," Opt. Lett. **29**, 5–7 (2004).

9. P. Chylek, J. T. Kiehl, and M. K. W. Ko, "Optical Levitation and Partial-Wave

Resonances," Phys. Rev. A **18**, 2229-2233 (1978).

10. A. A. Savchenkov, A.B. Matsko, M. Mohageg, and L. Maleki, "Ringdown spectroscopy of stimulated Raman scattering in a whispering gallery mode resonator," Opt. Lett. **32**, 497-499 (2007).

11. Y. Dumeige, S. Trebaol, L. Ghisa, T. K. N. Nguyên, H. Tavernier, and P. Féron, "Determination of coupling regime of high-*Q* resonators and optical gain of highly selective amplifiers," J. Opt. Soc. Am. B **25**, 2073-2080 (2008).

12. A. T. Rosenberger and J. P. Rezac, "Whispering-gallery-mode evanescent-wave microsensor for trace-gas detection," Proc. SPIE **4265**, 102-112 (2001).

13. G. Farca, S. I. Shopova, and A. T. Rosenberger, "Cavity-enhanced laser absorption spectroscopy using microresonator whispering-gallery modes," Opt. Express **15**, 17443-17448 (2007).

14. D. Braunstein, A. M. Khazanov, G. A. Koganov, and R. Shuker, "Lowering of threshold conditions for nonlinear effects in a microsphere," Phys. Rev. A **53**, 3565–3572(1996).

15. Y. S. Park, A. K. Cook, and H. Wang, "Cavity QED with diamond nanocrystals and silica microspheres," Nano Lett. **6**, 2075–2079 (2006).

16. S. M. Spillane, T. J. Kippenberg, and K. J. Vahala, "Ultralow-threshold Raman laser using a spherical dielectric microcavity," Nature **415**, 621–623 (2002).

17. S. I. Shopova, G. Farca, A. T. Rosenberger, W. M. S. Wickramanayake, and N. A. Kotov, "Microsphere whispering-gallery-mode laser using HgTe quantum dots," Appl. Phys. Lett. **85**, 6101-6103 (2004).

18. V. Sandoghdar, F. Treussart, J. Hare, V. Lefe'vre-Seguin, J.-M. Raimond, and S. Haroche, "Very low threshold whispering-gallery-mode microsphere laser," Phys. Rev. A **54**, 1777–1780 (2006).

19. M. J. Humphrey, E. Dale, A. T. Rosenberger, and D. K. Bandy, "Calculation of optimal fiber radius and whispering-gallery mode spectra for a fiber-coupled microsphere," Opt. Commun. **271**, 124-131 (2007).

20. M. J. Humphrey, *Calculation of Coupling between Tapered Fiber Modes and Whispering-Gallery Modes of a Spherical Microlaser*, PhD Diss., Physics Dept., Oklahoma State University (2004).

21. S. Ilchenko, A. A. Savchenkov, A. B. Matsko, and L. Maleki," Nonlinear optics and crystalline whispering gallery mode cavities," Phys. Rev. Lett. **92,** 043903 (2004).

22. J. P. Rezac, *Properties and Applications of Whispering-Gallery Mode Resonances in Fused Silica Microspheres,* PhD Diss., Physics Dept., Oklahoma State University (2002).

23. I. S. Grudinin, A.B. Matsko, A. A. Savchenkov, D. Strekalov, V. Ilchenko and Lute Maleki, "Ultra high Q crystalline microcavities," Optics Communications, **265**, 33-38 (2006).

24. M. L. Gorodetsky and V. S. Ilchenko, "High-Q optical whispering-gallery microresonators: precession approach for spherical mode analysis and emission patterns with prism couplers," Opt. Commun. **113**, 133–143 (1994).

25. G. Farca, *Cavity-Enhanced Evanescent-Wave Chemical Sensing Using Microresonators*, PhD Diss., Physics Dept., Oklahoma State University (2006).

26. A. T. Rosenberger, "Analysis of whispering-gallery microcavity-enhanced chemical absorption sensors," Opt. Express **15**, 12959-12964 (2007).

27. V. S. Il'chenko and M. L. Gorodetskii, "Thermal nonlinear effects in optical whispering gallery microresonators," Laser Physics **2**, 1004-1009 (1992).

28. L. Collot, V. Lefèvre-Seguin, M. Brune, J.-M. Raimond and S. Haroche, "Very high-*Q* whispering-gallery mode resonances observed on fused silica microspheres," Europhys. Lett. **23**, 327-334 (1993).

29. T. Carmon, L. Yang, and K. J. Vahala, "Dynamical thermal behavior and thermal self-stability of microcavities," Opt. Express **12**, 4742-4750 (2004).

30. H. Rokhsari, S. M. Spillane, and K. J. Vahala, "Loss characterization in microcavities using the thermal bistability effect," Appl. Phys. Lett. **85**, 3029-3031 (2004).

31. S. C. Saxena and R. K. Joshi, *Thermal Accommodation and Adsorption Coefficients of Gases*, Vol. II-1 of *McGraw-Hill/CINDAS Data Series on Material Properties*, Y. S. Touloukian and C. Y. Ho, eds., (McGraw-Hill, New York, 1981), pp. 171-180.

32. I. H. Malitson, "Interspecimen Comparison of the Refractive Index of Fused Silica," J. Opt. Soc. Am. **55**, 1205-1209 (1965).

33. H. S. Carslaw and J. C. Jaeger, *Conduction of Heat in Solids*, (Clarendon, Oxford, 1959), Chap. IX, pp. 230-254.

34. W. R. Foss and E. J. Davis, "Transient Laser Heating of Single Solid Microspheres," Chem. Eng. Commun. **152-153**, 113-138 (1996).

35. E. H. Kennard, *Kinetic Theory of Gases*, (McGraw-Hill, New York, 1938), Chap. VIII, pp. 291-337.

36. A. T. Rosenberger, E. B. Dale, D. Ganta, and J. P. Rezac, "Investigating properties of surfaces and thin films using microsphere whispering-gallery modes," Proc. SPIE **6872**, 68720U–1-68720U–9 (2008).

37. A. L. Rogach, D. S. Koktysh, M. Harrison, and N. A. Kotov, "Layer-by-Layer Assembled Films of HgTe Nanocrystals with Strong Infrared Emission," Chem. Mater. **12**, 1526-1528 (2000).

38. R. K. Iler, *The chemistry of silica: Solubility, polymerization, colloid and surface properties, and Biochemistry*, (Wiley, New York, 1979), Chap. VII, pp. 622-730.

39. D. E. Leyden, *Silanes, Surfaces and Interfaces*, (Gordon and Breach Science Publishers, New York, 1986), Chap. I, pp. 1-25.

40. S. L. Westcott, J. Zhang, R. K. Shelton, N. M. K. Bruce, S. Gupta, S. L. Keen, J. W. Tillman, L. B. Wald, B. N. Strecker, A. T. Rosenberger, R. R. Davidson, W. Chen, K. G. Donovan, and J. V. Hryniewicz, "Broadband optical absorbance spectroscopy using a whispering gallery mode microsphere resonator," Rev. Sci. Instrum. **79,** 033106 (2008).

41. A. Isihara, "Determination of Molecular Shape by Osmotic Measurement," J. Chem. Phys. **18**, 1446-1449 (1950).

42. A. E. Fomin, M. L.Gorodetsky, I. S. Grudinin, V. S. Illchenko "Nonstationary nonlinear effects in optical microspheres," J. Opt. Soc. Am. B **22**, 459-465 (2005).

43. D. W. Vernooy, V. S. Ilchenko, H. Mabuchi, E.W. Streed, and H.J. Kimble, "High-*Q* measurements of fused-silica microspheres in the near infrared," Opt. Lett. **23**, 247-249 (1998).

44. G. M. Hale and M. R. Querry, "Optical Constants of Water in the 200-nm to 200-μm Wavelength Region," Appl. Opt. **12**, 555-563 (1973).

45. M. L. Gorodetsky, A. A. Savchenkov, and V. S. Ilchenko, "Ultimate Q of Optical Microsphere Resonators," Opt. Lett. **21**, 453-455 (1996).

46. D. M. Wieliczka, S. Weng and M. R. Querry, "Wedge shaped cell for highly absorbent liquids: infrared optical constants of water," Appl. Opt. **28**, 1714-1719 (1989).

47. D. J. Segelstein, "The Complex Refractive Index of Water," M.S. Thesis, Physics Dept., U. Missouri-Kansas City (1981).

48. N. L. Rosi and C. A. Mirkin, "Nanostructures in Biodiagnostics," Chem. Rev. **105**, 1547-1549 (2005).

49. G. K. Darbha, U. S. Rai, A. K. Singh, and P. C. Ray, "Gold-nanorod-based sensing of sequence specific HIV-1 virus DNA by using hyper-Rayleigh scattering spectroscopy," Chemistry **14**, 3896-3903 (2008).

50. C. Yu, H. Nakshatri, and J. Irudayaraj, "Identity profiling of cell surface markers by multiplex gold nanorod probes," Nano Lett **7**, 2300-2306 (2007).

51. G. J. Nusz, S. M. Marinakos, A. C. Curry, A. Dahlin, F. Hook, A. Wax, and A. Chilkoti, "Label-free plasmonic detection of biomolecular binding by a single gold nanorod," Anal. Chem. **80**, 984-989 (2008).

52. K. Park, *Synthesis, Characterization, and Self –Assembly of Size Tunable Gold Nanorods*, PhD Diss., Physics Dept., Georgia Institute of Technology (2006).

53. S. I. Shopova, C. W. Blackledge, A. T. Rosenberger, and N. F. Materer, "Gold nanorods grown from HgTe nanoparticles directly on various surfaces," Appl. Phys. Lett. **89**, 023120 (2006).

54. B. D. Busbee, S. O. Obare, and C. J. Murphy, "An improved synthesis of high-aspect ratio gold nanorods," Advanced Materials **15**, 414-416 (2003).

55. N. R. Jana, L. Gearheart, and C. J. Murphy, "Wet Chemical Synthesis of High Aspect Ratio Cylindrical Gold Nanorods," J. Phys. Chem. B **105**, 4065 (2001).

56. T. K. Sau and C. J. Murphy, "Seeded High Yield Synthesis of Short Au Nanorods in Aqueous Solution," Langmuir **20**, 6414 (2004).

57. B. Nikoobakht and M. A. El-Sayed, "Preparation and growth mechanism of gold nanorods (NRs) using seed-mediated growth method," Chem Mater **15**, 1957-1962 (2003).

58. J. M. Moon and A. Wei, "Uniform gold nanorod arrays from polyethylenimine-coated alumina templates," J. Phys. Chem. B **109**, 23336-23341 (2005).

59. F. Kim, J. H. Song, and P. Yang, "Photochemical Synthesis of Gold Nanorods," J. Am. Chem. Soc. **124**, 14316-14317 (2005)

60. B. P. Khanal and E. R. Zubarev, "Purification of high aspect ratio gold nanorods: complete removal of platelets," J. Am. Chem. Soc. **130**, 12634-12635 (2008).

61. J. G. Bayly, V. B. Kartha, and W. H. Stevens, "The absorption spectra of liquid phase H2O, HDO, and D2O from 0.7 μm to 10 μm," Infrared Phys. **3**, 211-223 (1963).

62. R. Gans, "The shape of ultra microscopic gold particles," Ann. Physik **37**, 881-900 (1912).

63. P. B. Johnson and R. W. Christy, "Optical-Constants of Noble-Metals," Phys. Rev. B **6**, 4370-4379 (1972).

64. A. Brioude, X. C. Jiang, and M. P. Pileni, "Optical Properties of Gold Nanorods: DDA Simulations Supported by Experiments," J. Phys. Chem. B **109,** 13138-13142 (2005).

65. Y. Huang, X. Duan, Q. Wei, and C. M. Lieber, "Directed Assembly of One-Dimensional Nanostructures into Functional Networks," Science **291**, 630-633 (2001).

66. Y. Cui and C. M. Lieber, "Functional nanoscale electronic devices assembled using silicon nanowire building blocks," Science **291,** 851-853 (2001).

67. Birol Ozturk, *Structural and transport properties of directly assembled nanowires*, PhD Diss., Physics Dept.,Oklahoma State University (2007).

68. C. Wang, Y. Hu, C. M. Lieber, and S. Sun, "Ultrathin Au Nanowires and Their Transport Properties," J. Am. Chem. Soc. **130**, 8902-8903 (2008).

69. J. J. Boote and S. D. Evans, "Dielectrophoretic manipulation and electrical characterization of gold nanowires," Nanotechnology **16**, 1500–1505 (2005).

70. K. D. Hermanson, S. O. Lumsdon, J. P. Williams, E. W. Kaler, and O. D. Velev, "Dielectrophoretic Assembly of Electrically Functional Microwires from Nanoparticle Suspensions," Science **294**, 1082-1086 (2001).

71. P. C. Jordan, "Association phenomena in a ferromagnetic colloid," Molec. Phys. **25**, 961-973 (1973).

72. L. Jie, M. J. Casavant, M. Cox, D. A. Walters, P. Boul, L. Wei, A. J. Rimberg, K. A. Smith, D. T. Colbert, and R. E. Smalley, "Controlled deposition of individual single-walled carbon nanotubes on chemically functionalized templates," Chem.Phys. Lett. **303**, 125-129 (1999).

73. M. Batzill, K. J. Sarstedt, and K. J. Snowdon, "Fabrication of periodic nanoscale Ag-wire arrays on vicinal $CaF_2$ surfaces," Nanotechnology **9**, 20-29 (1998**)**.

74. T. K. Huang, Y. C. Chen, H. C. Chen, H. C. Ko, H.W. Huang, C. H. Wang, H. K. Lin, F. R. Chen, J. J. Kai, C. Y. Lee and H. T. Chiu, "Growth of High-Aspect-Ratio Gold Nanowires on Silicon by Surfactant-Assisted Galvanic Reductions," Langmuir **24**, 5647-5649 (2008).

75. H. J. Huang, C. P. Yu, H. C. Chang, K. P. Chiu, H. M. Chen, R. S. Liu, and D. P. Tsai, "Plasmonic optical properties of a single gold nano-rod," Opt. Express **15**, 7132–7139 (2007).

76. S. Hsieh, S. Meltzer, C. R. C. Wang, A. A. G. Requicha, M. E. Thompson, and B. E. Koel, "Imaging and manipulation of gold nanorods with an atomic force microscope," J. Phys. Chem. B **106**, 231-234 (2002).

77. H. S. Park, A. Agarwal, N. A. Kotov, and O. D. Lavrentovich, "Controllable side-by-side and end-to-end assembly of gold nanorods by lyotropic chromonic materials," Langmuir **24,** 13833-13837 (2008).

78. P. Fournet, J. N. Coleman, B. Lahr, A. Drury, W. J. Blau, D. F. O'Brien, and H. H. Horhold, ''Enhanced brightness in organic light-emitting diodes using a carbon nanotube composite as an electron-transport layer,'' J. Appl. Phys. **90**, 969–975 (2001).

79. C. N. R. Rao, B. C. Satishkumar, A. Govindaraj, and M. Nath, ''Nanotubes,'' Chem. Phys. Chem. **2**, 78–105 (2001).

80. Z. W. Pan, S. S. Xie, B. H. Chang, C. Y. Wang, L. Lu, W. Liu, W. Y. Zhou, W. Z. Li, and L. X. Qian, "Very Long Carbon Nanotubes," Nature **394**, 631-632 (1998).

81. X. Li, Y. Liu, L. Fu, L. Cao, D. Wei, and Y. Wang, “Efficient Synthesis of Carbon Nanotube-Nanoparticle Hybrids,” Adv. Funct. Mater **16**, 2431-2437 (2006)

82. Elijah Dale**,** *Coupling Effects in Dielectric Microcavities,* PhD Diss., Physics Dept., Oklahoma State University (2010).

VITA

Ganta Deepak

Candidate for the Degree of

Doctor of Philosophy

Thesis: SURFACE EFFECTS AND GOLD-NANOSTRUCTURE SURFACE COATING OF WHISPERING-GALLERY MICRORESONATORS

Major Field: Photonics

Biographical:

Personal Data: Born on April 4, 1978 in India.

Education: Received Bachelor of Science degree in Electrical Engineering at University of Madras, Chennai, India, 1999; received a Master of Science in Electrical Engineering at Oklahoma State University, Stillwater, Oklahoma in May 2002. Completed the requirements for the Doctor of Philosophy degree with a major in Photonics at Oklahoma State University in May, 2010.

Experience: Employed by Oklahoma State University, Department of Physics as a graduate research assistant and graduate teaching assistant January 2003 to present.

Professional Membership: American Physical Society

Name: Ganta Deepak Date of Degree: May, 2010

Institution: Oklahoma State University Location: Stillwater, Oklahoma

Title of Study: SURFACE EFFECTS AND GOLD-NANOSTRUCTURE SURFACE COATING OF WHISPERING-GALLERY MICRORESONATORS

Pages in Study: 129 Candidate for the Degree of Doctor of Philosophy

Major Field: Photonics

Scope and Method of Study:

The purpose of this study is to explore the surface effects of high-quality-factor optical microsphere resonators and thin-film-coated microresonators in various ambient gases. In this work, we present a systematic study of the assembly and characterization of gold nanostructures. We employ a wet-chemical synthesis method for growing gold nanorods and a directed electrochemical method for assembly of gold nanowires. The adhesion methods of gold nanostructures on high-quality-factor optical microsphere resonators are also investigated.

Findings and Conclusions:

A novel method is employed for measuring thermal accommodation coefficients of various gases like nitrogen, helium and ambient air on several coated and uncoated surfaces of fused-silica microresonators, operating at room temperature. This method is further extended to measure the absorption coefficient of a surface film or water layer on a fused-silica microresonator, and provides a novel method to find the water layer desorption and adsorption rates on the surface of a microresonator in the presence of gases like ambient air and nitrogen. We have adapted methods for growing gold nanorods of different aspect ratios (AR), and developed a novel method of growing high-AR (20-400) gold nanowires from low-AR gold nanorods. Various methods were discovered to coat these gold nanostructures and carbon nanotubes on the fused-silica surface. The most successful method involves surface modification with MPMDMS (i.e., silanization) before coating with gold nanorods. These coating methods have made microresonators useful for plasmonic sensing applications.

ADVISER'S APPROVAL: Albert T. Rosenberger